

# **Assimilating Tropospheric Airborne Meteorological Data Reporting (TAMDAR) Observations and the Relative Value of Other Observation Types**

**by Brian P Reen and Robert E Dumais Jr**

**ARL-TR-7022**

**August 2014**

## **NOTICES**

### **Disclaimers**

The findings in this report are not to be construed as an official Department of the Army position unless so designated by other authorized documents.

Citation of manufacturer's or trade names does not constitute an official endorsement or approval of the use thereof.

Destroy this report when it is no longer needed. Do not return it to the originator.

# **Army Research Laboratory**

Adelphi, MD 20783-1197

---

---

**ARL-TR-7022**

**August 2014**

---

## **Assimilating Tropospheric Airborne Meteorological Data Reporting (TAMDAR) Observations and the Relative Value of Other Observation Types**

**Brian P Reen and Robert E Dumais Jr**  
**Computational and Information Sciences Directorate, ARL**

REPORT DOCUMENTATION PAGE			Form Approved OMB No. 0704-0188		
<p>Public reporting burden for this collection of information is estimated to average 1 hour per response, including the time for reviewing instructions, searching existing data sources, gathering and maintaining the data needed, and completing and reviewing the collection information. Send comments regarding this burden estimate or any other aspect of this collection of information, including suggestions for reducing the burden, to Department of Defense, Washington Headquarters Services, Directorate for Information Operations and Reports (0704-0188), 1215 Jefferson Davis Highway, Suite 1204, Arlington, VA 22202-4302. Respondents should be aware that notwithstanding any other provision of law, no person shall be subject to any penalty for failing to comply with a collection of information if it does not display a currently valid OMB control number.</p> <p><b>PLEASE DO NOT RETURN YOUR FORM TO THE ABOVE ADDRESS.</b></p>					
1. REPORT DATE (DD-MM-YYYY) August 2014		2. REPORT TYPE Final		3. DATES COVERED (From - To) 15 August 2012–30 September 2013	
4. TITLE AND SUBTITLE Assimilating Tropospheric Airborne Meteorological Data Reporting (TAMDAR) Observations and the Relative Value of Other Observation Types			5a. CONTRACT NUMBER		
			5b. GRANT NUMBER		
			5c. PROGRAM ELEMENT NUMBER		
6. AUTHOR(S) Brian P Reen and Robert E Dumais Jr			5d. PROJECT NUMBER		
			5e. TASK NUMBER		
			5f. WORK UNIT NUMBER		
7. PERFORMING ORGANIZATION NAME(S) AND ADDRESS(ES) US Army Research Laboratory ATTN: RDRL-CIE-M 2800 Powder Mill Road Adelphi MD 20783-1197			8. PERFORMING ORGANIZATION REPORT NUMBER  ARL-TR-7022		
9. SPONSORING/MONITORING AGENCY NAME(S) AND ADDRESS(ES)			10. SPONSOR/MONITOR'S ACRONYM(S)		
			11. SPONSOR/MONITOR'S REPORT NUMBER(S)		
12. DISTRIBUTION/AVAILABILITY STATEMENT Approved for public release; distribution unlimited.					
13. SUPPLEMENTARY NOTES					
14. ABSTRACT <p>The Weather Research and Forecasting model is applied here to domains centered over southern California in early 2012 to investigate how to best assimilate single-level, above-surface observations (e.g., aircraft-based observations) as well as the relative value of various observation types.</p> <p>Various configurations of observation nudging are applied to a single case day to assimilate aircraft-based observations on a 3-km horizontal grid-spacing domain nested in a 9-km domain in order to determine the best nudging configuration. These results are then used to configure model experiments on 5 case days that investigate the value of the aircraft data, a local rawinsonde, and more dense surface observations. These experiments indicate substantial day-to-day variability in the forecast improvements due to inclusion of observations. Overall, the inclusion of aircraft data improves temperature and water-vapor predictions, but degrades short-term (1–6 hours [h]) wind forecasts. The use of local rawinsonde data improves short-term temperature and wind forecasts, but degrades water-vapor forecasts. Ingesting denser surface observations improves surface forecasts of temperature, moisture, and wind, but above the surface the results may be degraded. Further experimentation is necessary to refine the results found in this study.</p>					
15. SUBJECT TERMS WRF, data assimilation, observation nudging, TAMDAR					
16. SECURITY CLASSIFICATION OF:			17. LIMITATION OF ABSTRACT  UU	18. NUMBER OF PAGES  87	19a. NAME OF RESPONSIBLE PERSON Brian P Reen
a. REPORT Unclassified	b. ABSTRACT Unclassified	c. THIS PAGE Unclassified			19b. TELEPHONE NUMBER (Include area code) (301) 394-3072

---

## Contents

---

<b>List of Figures</b>	<b>v</b>
<b>List of Tables</b>	<b>ix</b>
<b>Acknowledgments</b>	<b>x</b>
<b>1. Introduction</b>	<b>1</b>
<b>2. Model Description and Configuration</b>	<b>3</b>
<b>3. Case Description</b>	<b>5</b>
<b>4. Methodology</b>	<b>12</b>
4.1 Observation Preparation .....	12
4.2 Observation Nudging .....	13
<b>5. Exploring Observation-Nudging Parameters for TAMDAR Assimilation</b>	<b>14</b>
5.1 Experimental Design .....	14
5.2 Results .....	17
5.2.1 Noise .....	17
5.2.2 Verification .....	18
5.2.3 Data-Assimilation Benefit vs. Degradation .....	27
5.3 Summary and Conclusions .....	30
<b>6. Exploring the Value of Various Observational Data Sources</b>	<b>31</b>
6.1 Experimental Design .....	31
6.2 Results .....	33
6.2.1 Value of TAMDAR Observations .....	33
6.2.1.1 Three-kilometer Domain .....	34
6.2.1.2 One-kilometer Domain .....	40
6.2.2 Value of Local Rawinsonde .....	46
6.2.3 Value of Denser Surface Observations .....	60
6.3 Summary and Conclusions .....	66
6.3.1 TAMDAR .....	66

6.3.2	Local Rawinsonde .....	67
6.3.3	Denser Surface Observations .....	68
<b>7.</b>	<b>References</b>	<b>69</b>
	<b>List of Symbols, Abbreviations, and Acronyms</b>	<b>72</b>
	<b>List of Variables</b>	<b>74</b>
	<b>Distribution List</b>	<b>75</b>

---

## List of Figures

---

Fig. 1	Map of the 9-, 3-, and 1-km horizontal grid-spacing WRF domains .....	3
Fig. 2	Plots of the number of TAMDAR observations within the 3-km WRF domain for each of the 5 case days. Time series of the number of all observations between 0 and 12,000-m AGL are shown for a) temperature observations, c) dewpoint observations, and e) wind observations. Profiles of all observations from 12 UTC on the case day until the end of the WRF simulation at 12 UTC on the next day are shown for b) temperature observations, d) dewpoint observations, and f) wind observations. ....	7
Fig. 3	Location of TAMDAR observations between 1131 and 1800 UTC inclusive for a) 7 February, b) 9 February, c) 16 February, d) 1 March, and e) 5 March. The extent of the plot matches the extent of the 9-km domain, and the 3-km domain is the white square labeled “d02” while the 1-km domain is the red square labeled “d03”. ....	9
Fig. 4	Locations where a rawinsonde is available for at least one of the case days during the data-assimilation period (specifically 1131–1800 UTC). Note that KEDW has a rawinsonde during these cases only for 9 February and 16 February, and that KNSI only has a rawinsonde for these case days for 1 March. ....	10
Fig. 5	Map of all surface mesonet and non-mesonet observations available within the MADIS database for the 3 WRF domains. The area covered by the figure is coincident with the area of the 9-km domain. The 3-km domain is the white square labeled “d02” and the 1-km domain is the red square labeled “d03”. ....	11
Fig. 6	Map of all surface mesonet and non-mesonet observations available within the MADIS database for the 1-km WRF domain .....	12
Fig. 7	Time series showing the percentage of the error at time 0 that is still extant at a given time. This assumes that the only factor affecting the field is the nudging term. ....	15
Fig. 8	Time series of 3-km domain’s average tendency of perturbation dry air mass ( $dmu/dt$ ) relative to the experiment with no data assimilation for all experiments with an <i>obs_rinxy</i> of 60 km for 1 March 2012. A 100-point centered average was applied to smooth out the high-frequency variability .....	18
Fig. 9	Temperature MAE (K) for the experiments in Table 1: for 19–00 UTC (1–6-h forecast; a, c, e) and for 01–12 UTC (7–18-h forecast; b, d, f); at 2-m AGL (e, f), at 0–1,000-m AGL (c, d), and at 0–12,000-m AGL (a, b). The x-axis indicates the nudging strength ( $G_q$ ) of the experiment and the symbols indicate the <i>obs_rinxy</i> setting used to determine horizontal radius of influence. ....	20
Fig. 10	Dewpoint temperature MAE (K) for the experiments in Table 1: for 19–00 UTC (1–6 h-forecast; a, c, e) and 01–12 UTC (7–18-h forecast; b, d, f); at 2-m AGL (e, f), at 0–1,000-m AGL (c, d), and at 0–12,000- m AGL (a, b). The x-axis indicates the nudging strength ( $G_q$ ) of the experiment and the symbols indicate the <i>obs_rinxy</i> setting used to determine horizontal radius of influence. ....	22

Fig. 11	Wind-speed MAE (m/s) for the experiments in Table 1: for 19–00 UTC (1–6-h forecast; a, c, e) and for 01–12 UTC (7–18-h forecast; b, d, f); at 10-m AGL (e, f), at 0–1,000-m AGL (c, d), and at 0–12,000-m AGL (a, b). The x-axis indicates the nudging strength ( $G_q$ ) of the experiment and the symbols indicate the <i>obs_rinxy</i> setting used to determine horizontal radius of influence. ....	24
Fig. 12	Wind-direction MAE (degrees) for the experiments in Table 1: for 19–00 UTC (1–6-h forecast; a, c, e) and for 01–12 UTC (7–18-h forecast; b, d, f); at 10-m AGL (e, f), at 0–1,000-m AGL (c, d), and at 0–12,000-m AGL (a, b). The x-axis indicates the nudging strength ( $G_q$ ) of the experiment and the symbols indicate the <i>obs_rinxy</i> setting used to determine horizontal radius of influence. ....	25
Fig. 13	The percentage of observations against which the model verifies non-negligibly better as compared to the no-nudging experiments (a, c), and of the subset of observation against which the model verifies non-negligibly differently the percentage for which the change is an improvement (PCI; b, d). These are plotted for all experiments for the 0–1,000-m AGL level for 19–00 UTC for both temperature (a, b) and dewpoint (c, d). ....	28
Fig. 14	The percentage of observations against which the model verifies non-negligibly better as compared to the no-nudging experiments (a, c), and of the subset of observations against which the model verifies non-negligibly differently than the no-nudging experiments, the percentage for which the change is an improvement (PCI; b, d). These are plotted for all experiments for the 0–1,000-m AGL level for 19–00 UTC for both wind speed (a, b) and wind direction (c, d). ....	30
Fig. 15	WRF 3-km domain MAEs for Exp. C, T, S, and TS from Table 3 verified against non-surface observations in the 0–1,000-m AGL layer for 19–00 UTC for a) temperature, b) dewpoint, c) wind speed, and d) wind direction. The x-axis indicates the experiment's name and the symbols indicate the case day of the experiment. ....	35
Fig. 16	Difference in MAE between Exp. C and Exp. T (columns labeled C-T) and between Exp. S and Exp. TS (columns labeled S-TS) for 19–00 UTC for 2 m, 0–1,000-m AGL, and 0–12,000-m AGL on the 3-km domain for a) temperature and b) dewpoint. Positive values indicate Exp. T performs better than Exp. C and that Exp. TS performs better than Exp. S, respectively. A point is plotted for each case day as well as the mean of all of the case days, as noted in the figure legend. ....	37
Fig. 17	Difference in MAE between Exp. C and Exp. T (columns labeled C-T) and between Exp. S and Exp. TS (columns labeled S-TS) for 19–00 UTC for 10 m, 0–1,000-m AGL, and 0–12,000-m AGL on the 3-km domain for a) wind speed and b) wind direction. Positive values indicate Exp. T performs better than Exp. C and that Exp. TS performs better than Exp. S, respectively. A point is plotted for each case day as well as the mean of all of the case days, as noted in the figure legend. ....	38
Fig. 18	Difference in MAE between Exp. C and Exp. T (columns labeled C-T) and between Exp. S and Exp. TS (columns labeled S-TS) for 01–12 UTC for, 0–1,000-m AGL on the 3-km domain for a) temperature, b) dewpoint, c) wind speed, and d) wind direction. Positive values indicate Exp. T performs better than Exp. C and that Exp. TS performs better than Exp. S, respectively. A point is plotted for each case day as well as the mean of all of the case days, as noted in the figure legend. ....	40



Fig. 19	WRF 1-km domain MAE for experiments C, T, S, and TS from Table 3 verified against non-surface observations in the 0–1,000-m AGL layer for 19–00 UTC for a) temperature, b) dewpoint, c) wind speed, and d) wind direction. The x-axis indicates the experiment’s name and the symbols indicate the case day of the experiment.....	42
Fig. 20	Difference in MAE between Exp. C and Exp. T (columns labeled C-T) and between Exp. S and Exp. TS (columns labeled S-TS) for 19–00 UTC for 2 m, 0–1,000-m AGL, and 0–12,000-m AGL on the 1-km domain for a) temperature and b) dewpoint. Positive values indicate Exp. T performs better than Exp. C and that Exp. TS performs better than Exp. S, respectively. A point is plotted for each case day as well as the mean of all of the case days, as noted in the figure legend. ....	43
Fig. 21	Difference in MAE between Exp. C and Exp. T (columns labeled C-T) and between Exp. S and Exp. TS (columns labeled S-TS) for 19–00 UTC for 10 m, 0–1,000-m AGL, and 0–12,000-m AGL on the 1-km domain for a) wind speed and b) wind direction. Positive values indicate Exp. T performs better than Exp. C and that Exp. TS performs better than Exp. S, respectively. A point is plotted for each case day as well as the mean of all of the case days, as noted in the figure legend. ....	44
Fig. 22	Difference in MAE between Exp. C and Exp. T (columns labeled C-T) and between Exp. S and Exp. TS (columns labeled S-TS) for 01–12 UTC for 0–1,000-m AGL on the 1-km domain for a) temperature, b) dewpoint, c) wind speed, and d) wind direction. Positive values indicate Exp. T performs better than Exp. C and that Exp. TS performs better than Exp. S, respectively. A point is plotted for each case day as well as the mean of all of the case days, as noted in the figure legend. ....	45
Fig. 23	Difference in MAE between Exp. SK and Exp. S (columns labeled SK-S) and between Exp. TSK and Exp. TS (columns labeled TSK-TS) for 19–00 UTC for 2 m, 0–1,000-m AGL, and 0–12,000-m AGL on the 1-km domain for a) temperature and b) dewpoint. Positive values indicate Exp. S performs better than Exp. SK and that Exp. TS performs better than Exp. TSK, respectively. A point is plotted for each case day as well as the mean of all of the case days, as noted in the figure legend. ....	47
Fig. 24	Difference in MAE between Exp. SK and Exp. S (columns labeled SK-S) and between Exp. TSK and Exp. TS (columns labeled TSK-TS) for 19–00 UTC for 10 m, 0–1,000-m AGL, and 0–12,000-m AGL on the 1-km domain for a) wind speed and b) wind direction. Positive values indicate Exp. S performs better than Exp. SK and that Exp. TS performs better than Exp. TSK, respectively. A point is plotted for each case day as well as the mean of all of the case days, as noted in the figure legend. ....	48
Fig. 25	Difference in MAE between Exp. SK and Exp. S (columns labeled SK-S) and between Exp. TSK and Exp. TS (columns labeled TSK-TS) for 01–12 UTC for 2 m, 0–1,000-m AGL, and 0–12,000-m AGL on the 1-km domain for a) temperature and b) dewpoint. Positive values indicate Exp. S performs better than Exp. SK and that Exp. TS performs better than Exp. TSK, respectively. A point is plotted for each case day as well as the mean of all of the case days, as noted in the figure legend. ....	50
Fig. 26	Difference in MAE between Exp. SK and Exp. S (columns labeled SK-S) and between Exp. TSK and Exp. TS (columns labeled TSK-TS) for 01–12 UTC for 10 m, 0–1,000-m AGL, and 0–12,000-m AGL on the 1-km domain for a) wind speed and b) wind direction. Positive values indicate Exp. S performs better than Exp. SK and that Exp. TS performs better than Exp. TSK, respectively. A point is plotted for each case day as well as the mean of all of the case days, as noted in the figure legend. ....	51

Fig. 27 Vertical profiles of temperature MAE (excluding surface observations) for 19–00 UTC for Exp. SK and Exp. S for a) 7 February, b) 9 February, c) 16 February, d) 1 March, and e) 5 March. Panel f is a vertical profile of the number of observations used to construct the MAE in panels a–e. ....	53
Fig. 28 Vertical profiles of dewpoint MAE (excluding surface observations) for 19–00 UTC for Exp. SK and Exp. S for a) 7 February, b) 9 February, c) 16 February, d) 1 March, and e) 5 March. Panel f is a vertical profile of the number of observations used to construct the MAE in panels a–e. ....	54
Fig. 29 Vertical profiles of wind-speed MAE (excluding surface observations) for 19–00 UTC for Exp. SK and Exp. S for a) 7 February, b) 9 February, c) 16 February, d) 1 March, and e) 5 March. Panel f is a vertical profile of the number of observations used to construct the MAE in panels a–e. ....	55
Fig. 30 Vertical profiles of wind-direction MAE (excluding surface observations) for 19–00 UTC for Exp. SK and Exp. S for a) 7 February, b) 9 February, c) 16 February, d) 1 March, and e) 5 March. Panel f is a vertical profile of the number of observations used to construct the MAE in panels a–e. ....	56
Fig. 31 Differences in MAE between Exp. S and Exp. TSK for 19–00 UTC for surface, 0–1,000-m AGL, and 0–12,000-m AGL on the 1-km domain for a) temperature, b) dewpoint, c) wind speed, and d) wind direction. Positive values indicate Exp. TSK performs better than Exp. S. A point is plotted for each case day as well as the mean of all of the case days, as noted in the figure legend. ....	58
Fig. 32 Differences in MAE between Exp. S and Exp. TSK for 01–12 UTC for surface, 0–1,000-m AGL, and 0–12,000-m AGL on the 1-km domain for a) temperature, b) dewpoint, c) wind speed, and d) wind direction. Positive values indicate Exp. TSK performs better than Exp. S. A point is plotted for each case day as well as the mean of all of the case days, as noted in the figure legend. ....	59
Fig. 33 Differences in MAE between Exp. S and Exp. SM for 19–00 UTC for surface, 0–1,000-m AGL, and 0–12,000-m AGL on the 1-km domain for a) temperature, b) dewpoint, c) wind speed, and d) wind direction. Positive values indicate Exp. SM performs better than Exp. S. A point is plotted for each case day as well as the mean of all of the case days, as noted in the figure legend. ....	61
Fig. 34 Differences in MAE between Exp. S and Exp. SM for 01–12 UTC for surface, 0–1,000-m AGL, and 0–12,000-m AGL on the 1-km domain for a) temperature, b) dewpoint, c) wind speed, and d) wind direction. Positive values indicate Exp. SM performs better than Exp. S. A point is plotted for each case day as well as the mean of all of the case days, as noted in the figure legend. ....	62
Fig. 35 Time series of the differences in MAE between Exp. S and Exp. SM on the 1-km domain for a) 2-m temperature, b) 2-m dewpoint, c) 10-m wind speed, and d) 10-m wind direction. Positive values indicate Exp. SM performs better than Exp. S. A time series is plotted for each case day, as noted in the legend. The vertical line at 18 UTC indicates the end of the preforecast period and the beginning of the forecast period during which no current observations are assimilated. ....	64

Fig. 36 Time series of the differences in MAE between Exp. S and Exp. SM averaged over the 5 case days on the 1-km domain for a) 2-m temperature, b) 2-m dewpoint, c) 10-m wind speed, and d) 10-m wind direction. Positive values indicate Exp. SM performs better than Exp. S. The vertical line at 18 UTC indicates the end of the preforecast period and the beginning of the forecast period during which no current observations are assimilated.....65

---

## List of Tables

---

Table 1 List of WRF-ARW experiments exploring the assimilation of TAMDAR observations on 1 March 2012 using varying nudging strengths and horizontal radii of influence.....	16
Table 2 Ranking of MAE values for the 4 experiments with the lowest MAE, with “1” being the best of the 4 experiments and “4” being the worst.....	26
Table 3 Experimental design for Section 6 indicating which observations are assimilated in each experiment (“Y” is yes) .....	32

---

## Acknowledgments

---

AirDat LLC provided Tropospheric Airborne Meteorological Data Reporting observational data that expanded the above-surface data available for data assimilation and verification. This study was made possible in part due to the data made available to the National Oceanic and Atmospheric Administration by various providers for inclusion in the Meteorological Assimilation Data Ingest System (MADIS). The parallel Real-Time Mesoscale Analysis “use” and “reject” lists were provided by Steve Levine at the National Weather Service’s National Centers for Environmental Prediction – Environmental Modeling Center and greatly facilitated making full use of the MADIS observational data set. The madis2littler tool was provided by Ruifang Li (then) at the National Center for Atmospheric Research. Martin Kufus is acknowledged for his efforts as technical editor that improved the clarity of this manuscript and ensured it adhered to the proper format.

---

## 1. Introduction

---

Aircraft-based observations are a potentially promising data source for improving numerical weather prediction. Standard in situ observations above the surface are mostly limited to twice-daily rawinsondes at a limited number of locations (with an average spacing between rawinsondes of about 315 km over the United States) (Office of the Federal Coordinator for Meteorological Services and Supporting Research 1997). Compared to rawinsonde observations, there are many more surface observations available, especially over locations such as the continental United States. However, an individual surface observation is potentially less valuable for data assimilation than an individual above-surface observation; this is because of the less heterogeneous atmospheric conditions found above the surface and thus the greater error-correlation length scales above the surface as compared to at the surface. Aircraft-based observations have the potential to provide an additional source of above-surface observations and are neither limited to a specified number of locations nor to a twice-daily observation.

There are many aircraft-based weather observations available, and they are referred to in general as aircraft meteorological data relay (AMDAR) reports. The data from the United States that are part of AMDAR are referred to as both Meteorological Data Collection and Reporting System (MDCRS) and by a system that is used to transmit some MDCRS observations, the Aircraft Communications Addressing and Reporting System (ACARS). A new network of aircraft-based observation called Tropospheric Airborne Meteorological Data Reporting (TAMDAR) (Daniels et al. 2004) has been introduced in recent years by AirDat, LLC. TAMDAR has several potential advantages compared to AMDAR. AMDAR observations are usually from larger aircraft; since larger aircraft tend to use larger airports, AMDAR observations are likely to be present below 20,000 feet above ground level (AGL) only around major airports (Moninger et al. 2010). TAMDAR observations are generally on smaller commercial aircraft, which have the ability to use smaller airports than larger aircraft, and thus TAMDAR observations should have the potential to provide broader coverage below 20,000 feet than other aircraft observations. Additionally, TAMDAR observations measure water vapor while many AMDAR observations do not. Gao et al. (2012) estimated that TAMDAR errors are comparable to rawinsondes' for temperature, slightly worse for winds <15 m/s, but slightly better for winds >15 m/s, and perhaps slightly better for moisture.

TAMDAR observations are of interest for Army applications because they may provide a source of weather observations in environments where the available observations are very limited. An effort involving the US Army Research Laboratory, New Mexico State University's Physical Science Laboratory's Technical Analysis and Applications Center, and AirDat LLC developed a modified TAMDAR sensor referred to as TAMDAR-Unmanned Aerial System (TAMDAR-U) for use on an unmanned aerial system (UAS) (Passner et al. 2012). This sensor was tested on a

UAS; the data produced were assimilated by the Advanced Research version of the Weather Research and Forecasting model (WRF-ARW) (Skamarock et al. 2008) using its observation-nudging capability and nested domains with 3-km and 1-km horizontal grid spacing. Three case studies were used to show the sensitivity of the model forecast to the assimilation of these TAMDAR-U data. Their results suggest that model moisture forecasts were most affected by assimilation of the TAMDAR-U observations. The downstream propagation of changes due to the assimilation of TAMDAR-U data was shown. However, due to the limited availability of observations in the study region, no statistical verification was undertaken in that study to demonstrate improvement in the forecast due to the assimilation of the TAMDAR-U data. Since Passner et al. (2012) used a UAS the flight tracks are likely more representative of what could potentially be available on the battlefield via UAS than a study using all of the standard TAMDAR data available.

Moninger et al. (2010) assimilate TAMDAR data in the 20-km horizontal grid spacing Rapid Update Cycle (RUC) model using three-dimensional variational (3DVAR) data-assimilation methods for approximately 4 years, and find that use of TAMDAR data results in improvements in temperature, moisture, and wind forecasts. Szoke et al. (2007) find that for specific precipitation events assimilating TAMDAR in RUC can be beneficial, apparently due to improvements in the model moisture fields. TAMDAR data have also been assimilated in WRF-ARW using both nudging (e.g., Zhang et al. 2011) and 3DVAR (e.g., Gao et al. 2012). Zhang et al. (2011) used nested 12- and 4-km horizontal grid-spacing WRF simulations with observation nudging to evaluate the impact of TAMDAR data for a 5-day case and found that moisture is generally improved, but the impact on temperature and wind is more mixed, especially on the 4-km domain.

Jonassen et al. (2012) assimilated observations from an unmanned aerial system over Iceland using observation nudging with 9-, 3-, and 1-km WRF-ARW nests for 2 case days. They investigated varying the size of the area over which a given observation was assimilated as well as the strength with which each observation affected the simulation. Their verification was purely against surface observations.

In this study, we investigate the value of assimilating TAMDAR observations using WRF-ARW configured with nested 9-, 3-, 1-km horizontal grid-spacing domains using observation nudging. This differs from previous TAMDAR studies in that we include investigation into the size of the area over which each observation should be assimilated and the strength with which they should be assimilated. There are similarities between the current effort and that of Jonassen et al. (2012), but here we use all available TAMDAR observations instead of a single UAS, and we include above-surface observations to enhance our verification.

---

## 2. Model Description and Configuration

---

The WRF-ARW Version 3.4.1 (Skamarock et al. 2008) was configured with 9-, 3-, and 1-km horizontal resolution domains centered over southern California, as shown in Fig. 1, and with 56 vertical layers (which implies there are 56 half levels and 57 full levels). For some experiments the 1-km domain was omitted. Depending on the experiment, the model was integrated from 12 Coordinated Universal Time (UTC) to 12 UTC for one or all of the 5 case days described in Section 3.

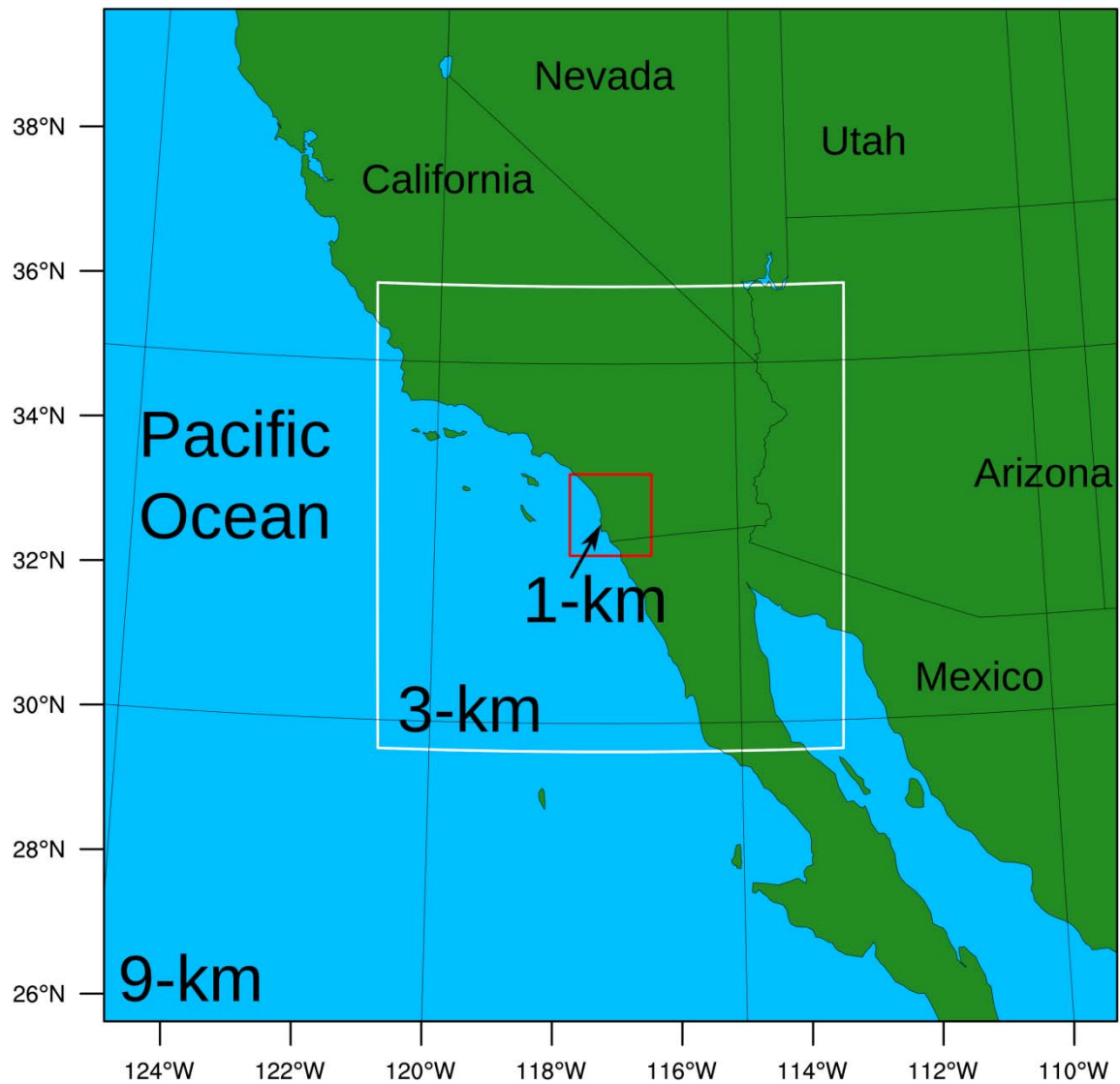


Fig. 1 Map of the 9-, 3-, and 1-km horizontal grid-spacing WRF domains

The Global Forecast System (GFS) model's  $0.5^\circ$  horizontal resolution output is used to create initial conditions and boundary conditions. Note that only GFS forecasts are utilized here (in contrast to analyses) so that we do not benefit from an observation type being included in the GFS analysis that a given model experiment is testing the exclusion of. For example, if we are testing the benefit of a specific rawinsonde and complete experiments both with and without that rawinsonde, but for both of these experiments use a GFS analysis for the initial conditions that includes this rawinsonde, we are not actually testing the effects of that local rawinsonde's absence. A sea-surface temperature product with higher resolution than the GFS output is produced by the National Centers for Environmental Prediction's Marine Modeling and Analysis Branch. Called the Real Time Global Sea Surface Temperature (Gemmill et al. 2007), it has  $1/12^{\text{th}}$  degree horizontal grid spacing and was used to specify sea-surface temperatures for these simulations. Where available, GFS snow fields were replaced with 1-km snow fields from the SNOw Data Assimilation System (SNODAS) developed by the National Weather Service's National Operational Hydrologic Remote Sensing Center (NOHRSC 2004).

Obsgrid is part of the WRF software suite and can be used to create objective analyses and to quality-control the observations. Initial conditions for some experiments in this study are enhanced with observations using Obsgrid. Modifications to the methodology used to create these objective analyses are described in Reen et al. (2014b). As described in Section 4.1, we also use Obsgrid to perform quality control of the observations used for inclusion in the initial conditions and for data assimilation.

The Mellor-Yamada-Janjić (MYJ) scheme (Janjić 2002) is used to parameterize the atmospheric boundary layer. This parameterization predicts turbulent kinetic energy (TKE) and is a Mellor-Yamada Level 2.5 turbulence closure model. As in Lee et al. (2012) and Reen et al. (2014a), the background TKE is decreased to better simulate conditions with low TKE and the atmospheric boundary layer (ABL) depth diagnosis is altered. In preliminary experiments for this study, the standard MYJ scheme resulted in noisy TKE fields and thus noisy ABL depth fields over the water, and contributed to the formation of dry spots at the surface over land due to nudging. These were resolved using the altered version of MYJ.

The WRF single-moment, 5-class microphysics parameterization (Hong et al. 2004; Hong and Lim 2006) and the Kain-Fritsch cumulus parameterization (Kain 2004) are utilized. For radiation, the Rapid Radiative Transfer Model (RRTM) (Mlawer et al. 1997) is used for longwave and the Dudhia scheme (Dudhia 1989) for shortwave. The Noah land surface model (Chen and Dudhia 2001) is used to represent land surface processes.

The observation-nudging capability of WRF (Deng et al. 2009) is used to incorporate observations into the model via a 6-hour preforecast (12 to 18 UTC). During this preforecast, the model is gradually nudged toward observations of temperature, moisture, and wind.



---

### 3. Case Description

---

Five 24-hour periods in early 2012 over the southwestern United States were modeled with each starting at 12 UTC: 7 February, 9 February, 16 February, 1 March, and 5 March. The case days were chosen to include days with active weather and those with more benign weather. On 7 February a trough moved onshore and led to widespread precipitation in the region. More quiescent weather was in place for the 9 February case with a 500-hPa ridge centered over central California at 12 UTC. On 16 February, an upper-level low was near the California/Arizona border with Mexico at 12 UTC bringing precipitation to that portion of the domain. The area of low pressure and the associated precipitation moved to the south and then east as the case day progressed. For 1 March, a weak shortwave trough at the beginning of the period resulted in precipitation in northern California that spread to Nevada and then moved southward and decreased in coverage. There was widespread high-level cloudiness for the 5 March case due to weak, upper-level low pressure but very limited precipitation.

Observations from the Meteorological Assimilation Data Ingest System (MADIS) database (at [madis.noaa.gov](http://madis.noaa.gov)) as well as TAMDAR (e.g., Gao et al. 2012) observations are available for these cases. The MADIS data include standard surface observations as well as mesonet data, maritime observations, profiler data, aircraft data, and rawinsondes. Note that although TAMDAR observations were in the past available via MADIS, as of the time of the case days studied here, TAMDAR observations were not available via MADIS. The TAMDAR observations were obtained directly from AirDat LLC. The MADIS database does include other aircraft-based observations, namely, ACARS observations.

The temporal and vertical distribution of TAMDAR observations available in the 3-km WRF domain for the 5 case days is plotted in Fig. 2. The 3-km WRF domain is plotted here because there are very few TAMDAR observations within the 1-km domain, and the 3-km domain is the focus of the TAMDAR data-assimilation experiments.

There is a clear temporal signal (Fig. 2a, 2c, 2e) with few TAMDAR observations between 09 and 15 UTC (0200–0800 Pacific Daylight Savings Time). In general, it is expected that there will be fewer TAMDAR observations overnight because there will generally be fewer commercial aircraft airborne. There is also substantial day-to-day variability in the diurnal variation of the number of TAMDAR observations among the case days. For example, the number of TAMDAR temperature observations available at 16 UTC is  $\approx 20$  for 9 February and 5 March but  $\approx 85$  for 16 February.

Over the entire WRF-ARW simulation period (1200 to 1200 UTC) more TAMDAR observations are in the lowest 1,000 m AGL than in any other layer (Fig. 2b, 2d, 2f), with notably fewer in the 1,000–2,000-m AGL layer compared to the 0–1,000-m AGL layer. The number of TAMDAR

observations per 1,000-m band gradually decreases with height in the layers above 2,000 m AGL. The substantial variability in the number of TAMDAR observations among cases seen temporally (Fig. 2a, 2c, 2e) is also seen vertically. For example, in the lowest 1,000 m AGL, 1 March has  $\approx 300$  temperature TAMDAR observations (Fig. 2d) whereas 5 March only has  $\approx 115$  TAMDAR temperature observations.

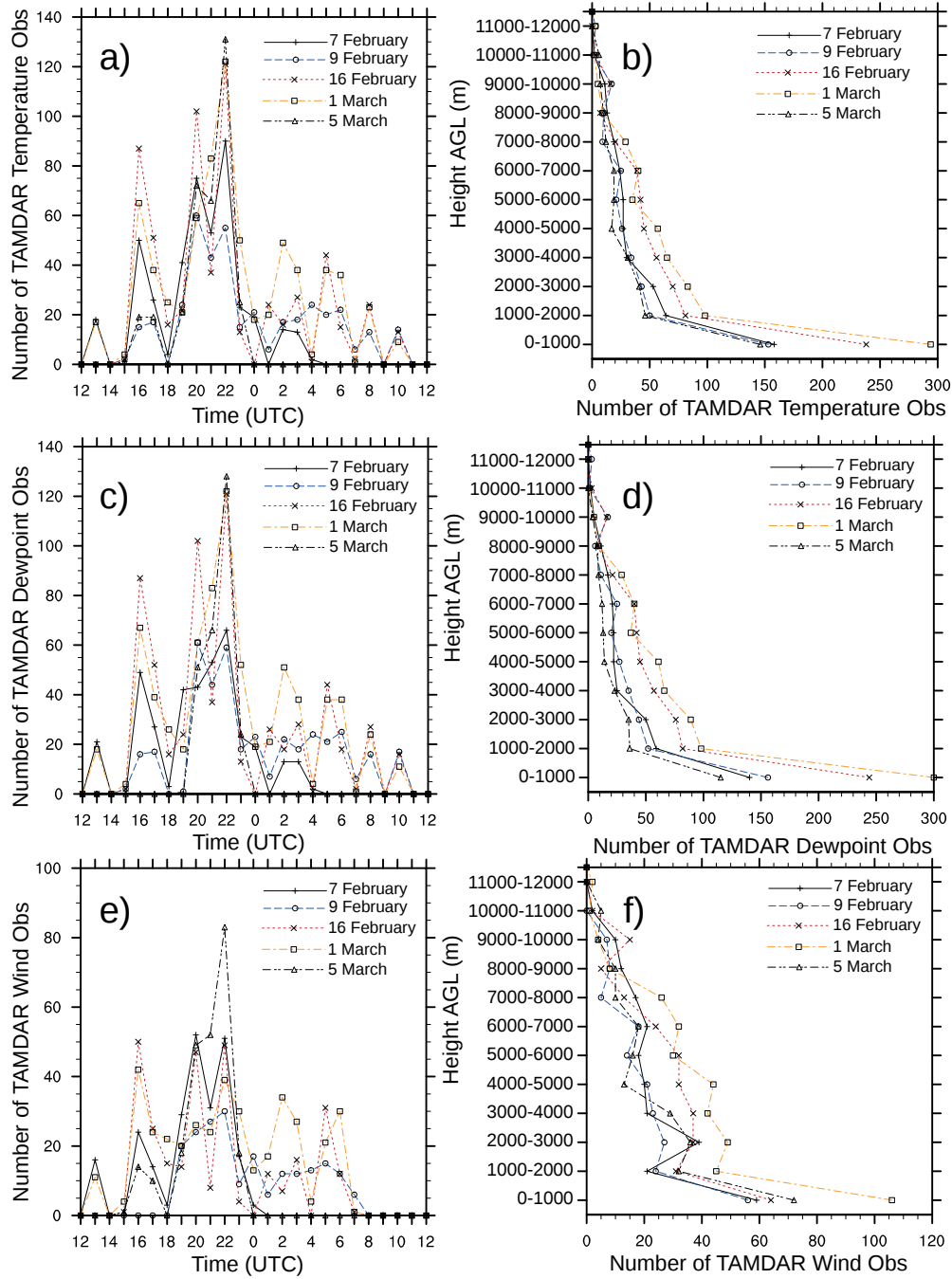


Fig. 2 Plots of the number of TAMДАР observations within the 3-km WRF domain for each of the 5 case days. Time series of the number of all observations between 0 and 12,000-m AGL are shown for a) temperature observations, c) dewpoint observations, and e) wind observations. Profiles of all observations from 12 UTC on the case day until the end of the WRF simulation at 12 UTC on the next day are shown for b) temperature observations, d) dewpoint observations, and f) wind observations.

The horizontal distribution of TAMDAR observations for the time period during which they are assimilated for some experiments is shown in Fig. 3. The plots show all TAMDAR observations between 1131 and 1800 UTC inclusive. Although TAMDAR observations prior to 1130 UTC may be used in the data assimilation if they are within the temporal window, here we include only those observations after 1130 UTC since the model begins integrating at 1200 UTC. For all of the case days, there is a greater concentration of TAMDAR in the vicinity of San Francisco's airport (located in the northwest portion of the 9-km domain) and in the vicinity of the Los Angeles airport (located in the northwest portion of the 3-km domain). There are also TAMDAR observations in Mexico on the 9-km domain on each case day that appear to be related to the airport in Hermosillo, Sonora, Mexico. On 7 February and 1 March, it appears that one of these flights uses the airport in Mexicali, Baja California, Mexico (just south of the California border). Note that there are no TAMDAR observations on the 1-km domain during this time period.

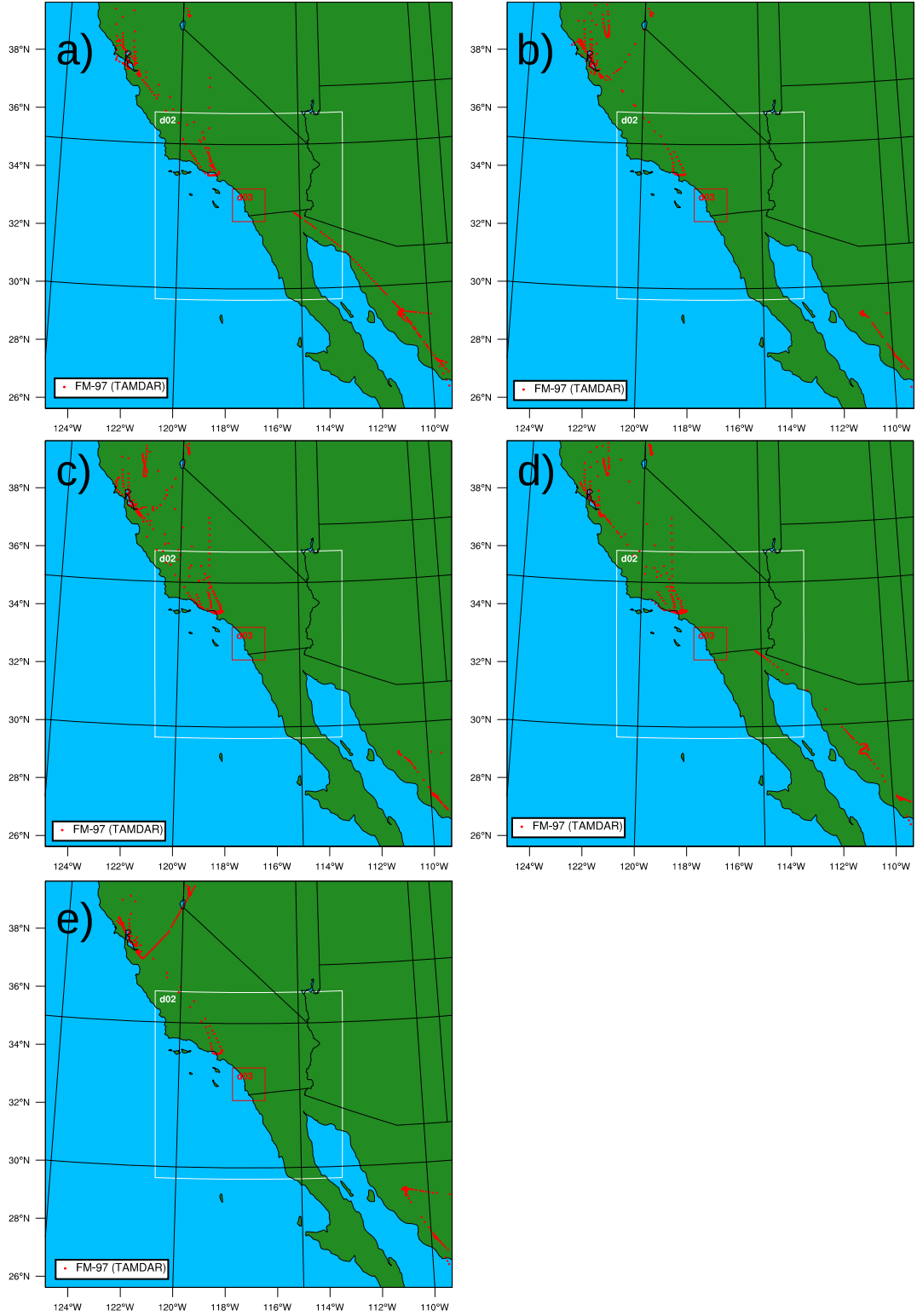


Fig. 3 Location of TAMDAR observations between 1131 and 1800 UTC inclusive for a) 7 February, b) 9 February, c) 16 February, d) 1 March, and e) 5 March. The extent of the plot matches the extent of the 9-km domain, and the 3-km domain is the white square labeled “d02” while the 1-km domain is the red square labeled “d03”.

Rawinsondes are available at various locations within the model domains, as indicated in Fig. 4. Note that rawinsondes are not available during the data-assimilation time period for KEDW (Edwards Air Force Base, CA) and KNSI (San Nicolas Island, CA) on all days. The KNKX rawinsonde (Marine Corps Air Station Miramar in San Diego, CA) is the only rawinsonde available within the 1-km domain.

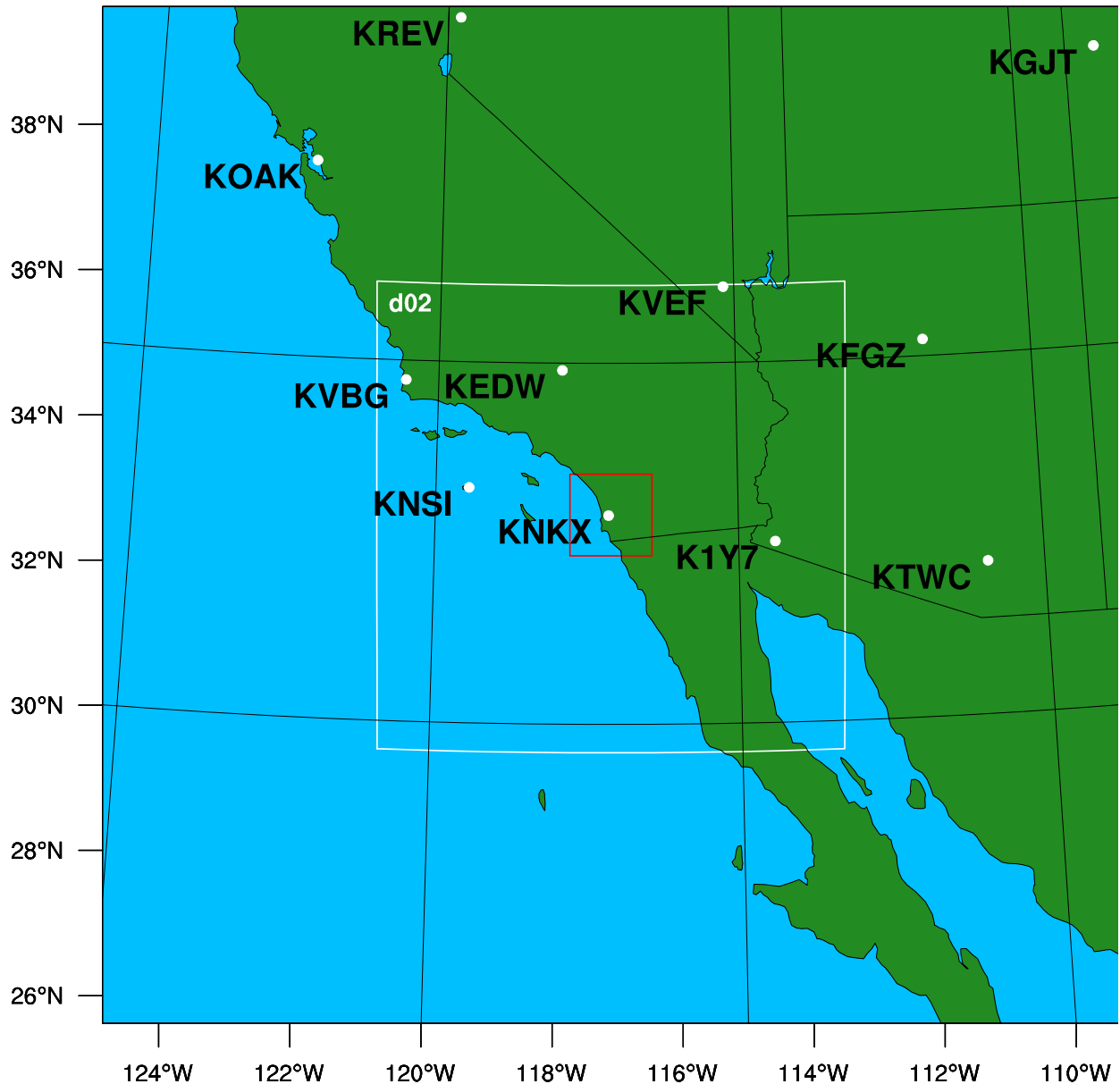


Fig. 4 Locations where a rawinsonde is available for at least one of the case days during the data-assimilation period (specifically 1131–1800 UTC). Note that KEDW has a rawinsonde during these cases only for 9 February and 16 February, and that KNSI only has a rawinsonde for these case days for 1 March.

The locations with at least one surface observation available on at least one of the case days during the approximate data assimilation period (1131–1800 UTC) are plotted in Fig. 5 for all 3

domains. The fact that mesonet stations are much more prevalent than non-mesonet stations is clearly evident, as is the clustering of observations in certain areas. Figure 6 also shows the locations of surface observations but shows only the 1-km domain. In general, there is fairly good coverage of mesonet stations over land except in Mexico, where very few observations are available. The apparent presence of mesonet stations just offshore is likely due to the reported locations of some mesonet stations being slightly inaccurate or imprecise.

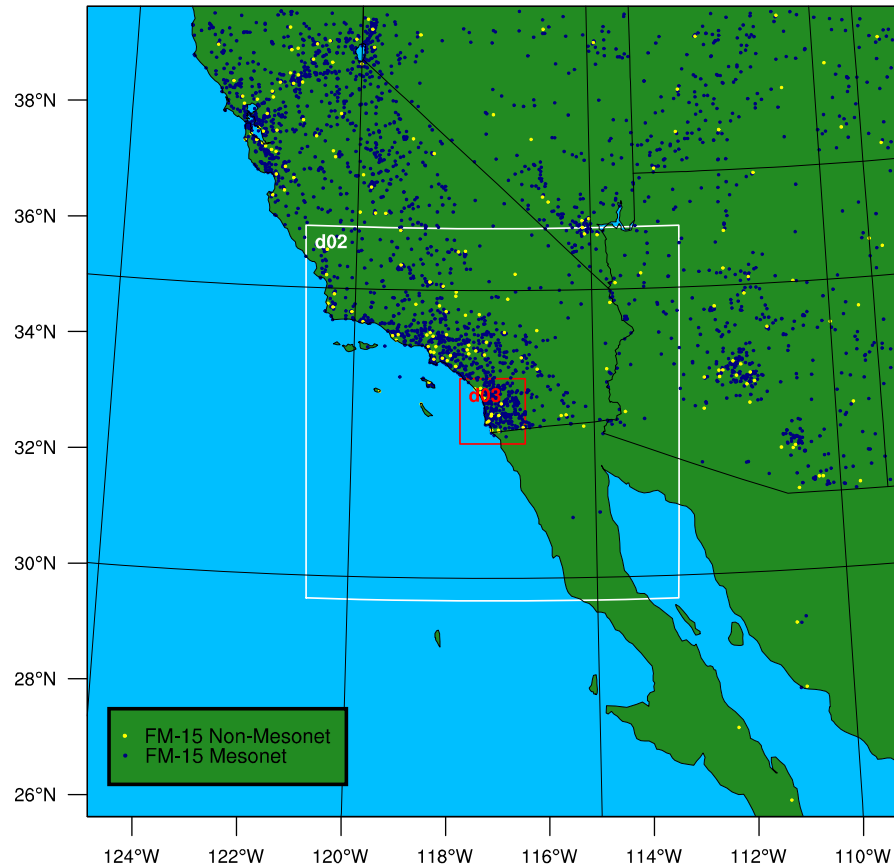


Fig. 5 Map of all surface mesonet and non-mesonet observations available within the MADIS database for the 3 WRF domains. The area covered by the figure is coincident with the area of the 9-km domain. The 3-km domain is the white square labeled “d02” and the 1-km domain is the red square labeled “d03”.

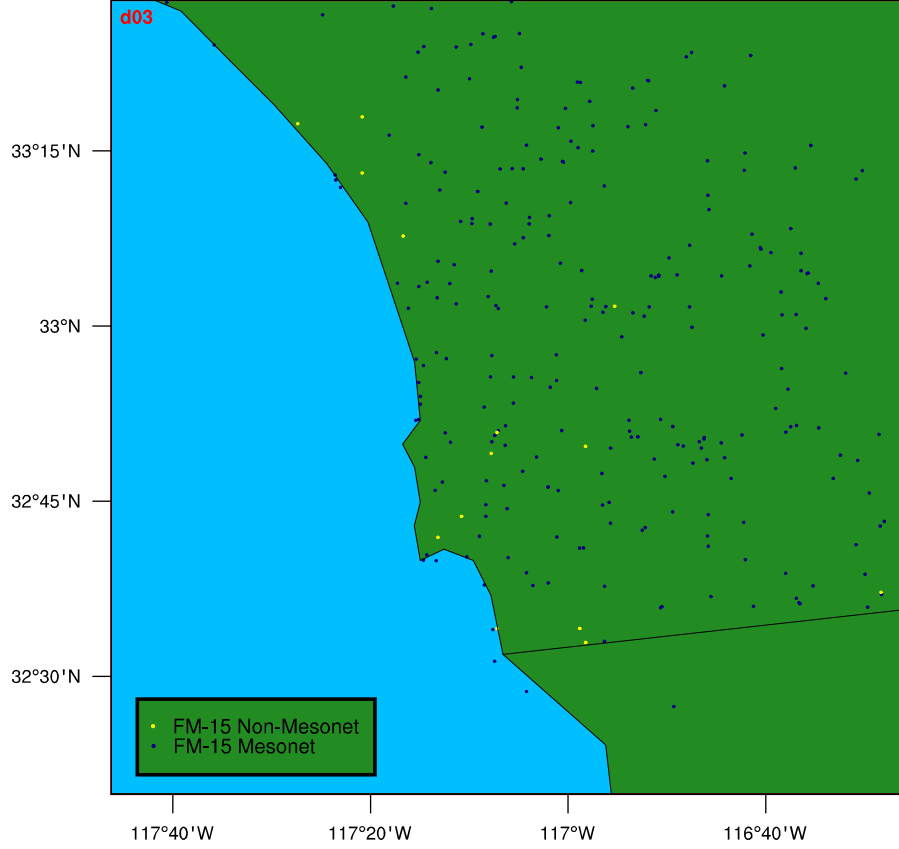


Fig. 6 Map of all surface mesonet and non-mesonet observations available within the MADIS database for the 1-km WRF domain

---

## 4. Methodology

---

### 4.1 Observation Preparation

The first step of quality control on the observations was applying use/reject lists from a non-operational version of the Real-Time Mesoscale Analysis (RTMA) (De Pondeva et al. 2011; Levine et al. 2011; Levine et al. 2012; Pondeva et al. 2012) to filter the mesonet data. Universal reject lists as well as separate day/night reject lists are used for temperature and moisture. For wind, mesonet observations are rejected unless they are on the universal accept list or the observed wind direction is within a wind-direction bin that is listed as acceptable for that station. The use of these use/reject lists is designed to maximize the positive impact of mesonet observations while minimizing the potential negative impact of mesonet observations that may not accurately reflect the actual meteorological conditions for the desired vertical location and spatial area due to issues such as siting (e.g., wind observations at heights other than 10 m AGL or obstructions near the observation location).



The majority of the quality control took place in the WRF component Obsgrid. The quality-control component of Obsgrid includes checking observations for gross errors, comparing observations to nearby observations (“buddy check”), and comparing observations to a background field (here, GFS). For moisture observations, in addition to checking relative humidity, buddy checks and checks against the background field for dewpoint were applied as noted in Reen et al. (2014b) to allow overly dry observations to be removed more efficiently. For multi-level, above-surface observations (e.g., rawinsondes), Obsgrid interpolates the vertical profile to pressure levels where GFS data exist in order to enable the background check to occur. The Ungrib component of the standard version of the WRF preprocessing system (WPS) merely converts coarse grid model data (e.g., GFS) from Gridded Binary (GRIB) format to a WPS format. Here, we use a modified version of Ungrib provided by the National Center for Atmospheric Research (NCAR) that additionally interpolates the coarse grid model data to user-specified levels. This minimizes the interpolation of multi-level, above-surface observations needed to enable the background check to occur, and allows for a more detailed vertical structure to be maintained in high vertical-resolution observations.

The standard version of Obsgrid will only effectively process single-level, above-surface observations if they are specific types of data. This is because of difficulties doing the background check of the observations: The single-level, above-surface observations are unable to be interpolated to a coarse-grid model pressure level (since they consist of a single level of data) and they are unlikely to fall exactly on a coarse-grid model pressure level. For observations labeled “FM-97 AIREP” and “FM-88 SATOB”, Obsgrid will attempt to create a new observation at the nearest coarse-grid model pressure level. It does this by adjusting temperature using a standard lapse rate, keeping the observed values of wind and discarding moisture. In order for the TAMDAR data and the MADIS aircraft data to be quality-controlled without doing these adjustments and discarding moisture, Obsgrid was modified to allow single-level, above-surface observations to be quality-controlled against nearby coarse-grid model pressure levels, rather than requiring the observation to be exactly on the pressure level. Combining this with the version of Ungrib used here to interpolate the coarse-grid model data to additional vertical levels allows the aircraft data to have background-check quality control performed without any adjustments to the observation itself.

## 4.2 Observation Nudging

Observation nudging adds a non-physical term to the tendency equations, and is implemented in WRF as:

$$\frac{\partial q\mu}{\partial t}(x, y, z, t) = F_q(x, y, z, t) + \mu G_q \frac{\sum_{i=1}^N W_q^2(i, x, y, z, t) [q_o(i) - q_m(x_i, y_i, z_i, t)]}{\sum_{i=1}^N W_q(i, x, y, z, t)} \quad (1)$$

where  $q$  is the quantity being nudged (e.g., water-vapor mixing ratio);  $\mu$  is the dry hydrostatic pressure;  $F_q$  represents the physical-tendency terms of  $q$ ;  $G_q$  is the nudging strength for  $q$ ;  $N$  is the total number of observations;  $i$  is the index to the current observation;  $W_q$  is the spatiotemporal weighting function;  $q_o$  is the observed value of  $q$ ; and  $q_m(x_i, y_i, z_i, t)$  is the model value of  $q$  interpolated to the observation location. The quantity  $q_o - q_m$  is the innovation.

In WRF observation nudging, the effects of surface observations are spread horizontally along the model surface whereas the effects of above-surface observations are spread horizontally in pressure. This is based on the assumption that model error at the surface at point A is better correlated with model error at the surface at point B than with the model error at the model level with the same pressure at point B. Note that unlike the standard WRF observation-nudging code, surface observations reported as part of a sounding are treated as surface observations by the observation nudging rather than as part of the sounding. This allows these observations to be spread along the surface rather than being spread horizontally based on pressure. In areas where the terrain height differs, spreading surface observations along a constant-pressure surface may be problematic.

---

## 5. Exploring Observation-Nudging Parameters for TAMDAR Assimilation

---

### 5.1 Experimental Design

In order to determine how to best assimilate TAMDAR observations, a series of model experiments utilizing the 9- and 3-km domains were completed for the 1 March 2012 case. These experiments assimilate TAMDAR observations only on the 3-km domain in order to better isolate the effects of various nudging configurations on this domain. Specifically, these experiments vary the strength with which observation nudging is applied and the size of the area over which the observation nudging applies corrections for a given observation.

The nudging strength,  $G_q$ , determines how quickly the model value approaches the observed value. If one assumes that the nudging term is the only term in the tendency equation, the inverse nudging strength is the  $e$ -folding time of the model error. Therefore the error is divided by  $e$  (i.e., 2.71828...) every time interval of  $1/G_q$ . Figure 7 shows the decrease in error with time due to observation nudging and assuming that all other tendency terms are zero. Nudging strengths ranging from  $1 \times 10^{-4}$  to  $128 \times 10^{-4} \text{ s}^{-1}$  are shown, which converts to  $e$ -folding times between  $\approx 167$  minutes to  $\approx 1.3$  minutes. Note that although the larger nudging strengths should result in the model more closely matching the observation, with larger nudging strengths the physical-tendency terms are less likely to dominate and thus the dynamical consistency of the model will not necessarily be maintained. Also, by forcing the model very strongly toward a given observation, we are assuming that there is no observational error. Thus, the stronger nudging

strengths can result in noise and overfitting. We investigate varying the nudging strength between  $1 \times 10^{-4}$  and  $128 \times 10^{-4} \text{ s}^{-1}$ .

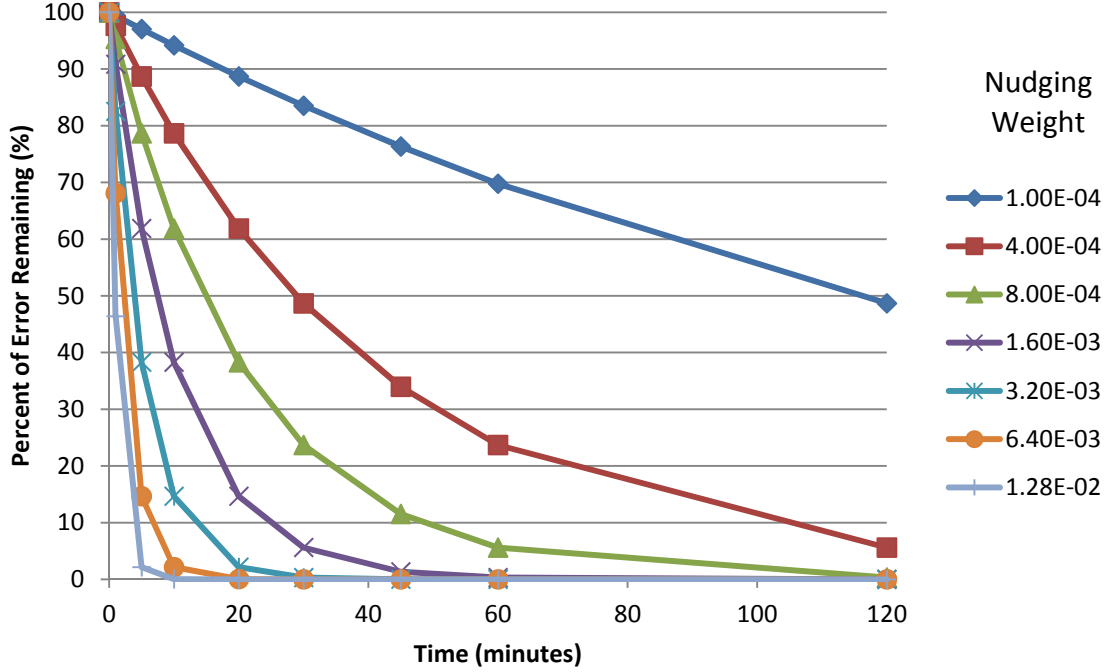


Fig. 7 Time series showing the percentage of the error at time 0 that is still extant at a given time. This assumes that the only factor affecting the field is the nudging term.

One component of the spatiotemporal weighting function,  $W_q$ , is the horizontal radius of influence, which is specified by the user using the option *obs\_rinxy*. Between the surface and 500 hPa, the user-chosen value is linearly increased with pressure to twice the chosen value, and remains at twice the chosen value above 500 hPa. For example, if one chooses *obs\_rinxy* = 60 km, then the radius of influence is 60 km just above the surface but increases linearly to 120 km at 500 hPa, and remains 120 km above 500 hPa. For surface observations the user may choose to decrease the effective radius of influence via a factor, but our focus here is on TAMDAR observations, which are above the surface. The horizontal radius of influence represents the error-correlation length scale, i.e., the maximum distance from the observation at which errors are correlated with errors at the observation location. The actual horizontal weighting function is:  $W_{xy} = (RIN^2 - DIST^2)/(RIN^2 + DIST^2)$  where *RIN* is the effective radius of influence for this observation (based on *obs\_rinxy* and the vertical placement of the observation) and *DIST* is the distance between the observation and current model point where the innovation is being applied. If the horizontal radius of influence is too large, we would be using an observation to correct the model at locations where the error is not correlated with the error at the observation location, and thus the corrections will not necessarily improve the model. If the horizontal radius of influence we utilize is too small, then we will not be as

effective in decreasing the model error as we could be. Here, we test varying the *obs\_rinxy* setting between 30 and 120 km.

The model experiments for the 1 March 2012 case that test the strength of the nudging and the horizontal extent of the nudging are listed in Table 1. For verification we use all of the observations described in Section 4.1 during the forecast period (19–12 UTC); these include standard surface observations as well as mesonet data, maritime observations, profiler data, aircraft data (both TAMDAR and ACARS), and rawinsondes.

Table 1 List of WRF-ARW experiments exploring the assimilation of TAMDAR observations on 1 March 2012 using varying nudging strengths and horizontal radii of influence

<i>obs_rinxy</i> (km)	Weight ( $\times 10^{-4} \text{ s}^{-1}$ )						
	None	1	4	8	16	32	64
30	X		X	X	X		
45			X	X	X		
60		X	X	X	X	X	X
90			X	X	X		
120			X	X	X		

As implemented in Reen et al. (2014b) we place a limit on negative water-vapor mixing ratio innovations when they are applied to locations where the model is drier than the model is at the observation location. Specifically, the magnitude of a negative moisture innovation applied to a location with less moisture than the location the innovation is calculated at is limited to be no more than the model water-vapor mixing ratio at the location the innovation is being applied to.

In other words, when applying an observation  $q_o(i)$  to  $(x, y, z, t)$  if:

$$\{[q_o(i) - q_m(x_i, y_i, z_i, t)] < 0\} \wedge \{q_m(x, y, z, t) < q_m(x_i, y_i, z_i, t)\} \quad (2)$$

then the nudging equation becomes:

$$\frac{\partial q \mu}{\partial t}(x, y, z, t) = F_q(x, y, z, t) + \mu G_q \frac{\sum_{i=1}^N W_q^2(i, x, y, z, t) \max\{[q_o(i) - q_m(x_i, y_i, z_i, t)] - q_m(x, y, z, t)\}}{\sum_{i=1}^N W_q(i, x, y, z, t)} \quad (3)$$

## 5.2 Results

### 5.2.1 Noise

To evaluate the noise in the model solution, we examine the domain-average absolute value of the tendency of perturbation dry air mass ( $d\mu/dt$ ). The purpose of this is to look for rapid changes in pressure, which would indicate noise. It is difficult to evaluate the meaning of this variable alone, but we can look at its value relative to a control experiment. Here we investigate the noise added via various observation-nudging configurations and use a model experiment with no data assimilation as the control experiment. Figure 8 shows the noise of each experiment on 1 March relative to the noise of the control experiment to show the added noise from data assimilation. As expected, the largest noise is seen in the experiment with the strongest nudging ( $G_q = 64 \times 10^{-4} \text{ s}^{-1}$ ). Data assimilation is applied at full strength through the first 6 h and then with linearly decreasing strength through the next hour. This is consistent with the added noise of data assimilation rapidly decreasing by 7 h. Also, note that most of the TAMDAR observations that were used for nudging were made between 4 and 6 h into the data assimilation (Fig. 2a, 2c, 2e), consistent with the largest noise occurring during this time period. Besides a spike to about 1.2 times the noise of the non-nudging experiment between 6 and 7 h, the  $8 \times 10^{-4} \text{ s}^{-1}$  experiment generally has low relative noise, and all experiments with  $G_q < 8 \times 10^{-4} \text{ s}^{-1}$  have very little noise compared to the experiment with strong nudging. This suggests that the optimal configuration should probably use  $G_q < 16 \times 10^{-4} \text{ s}^{-1}$ .

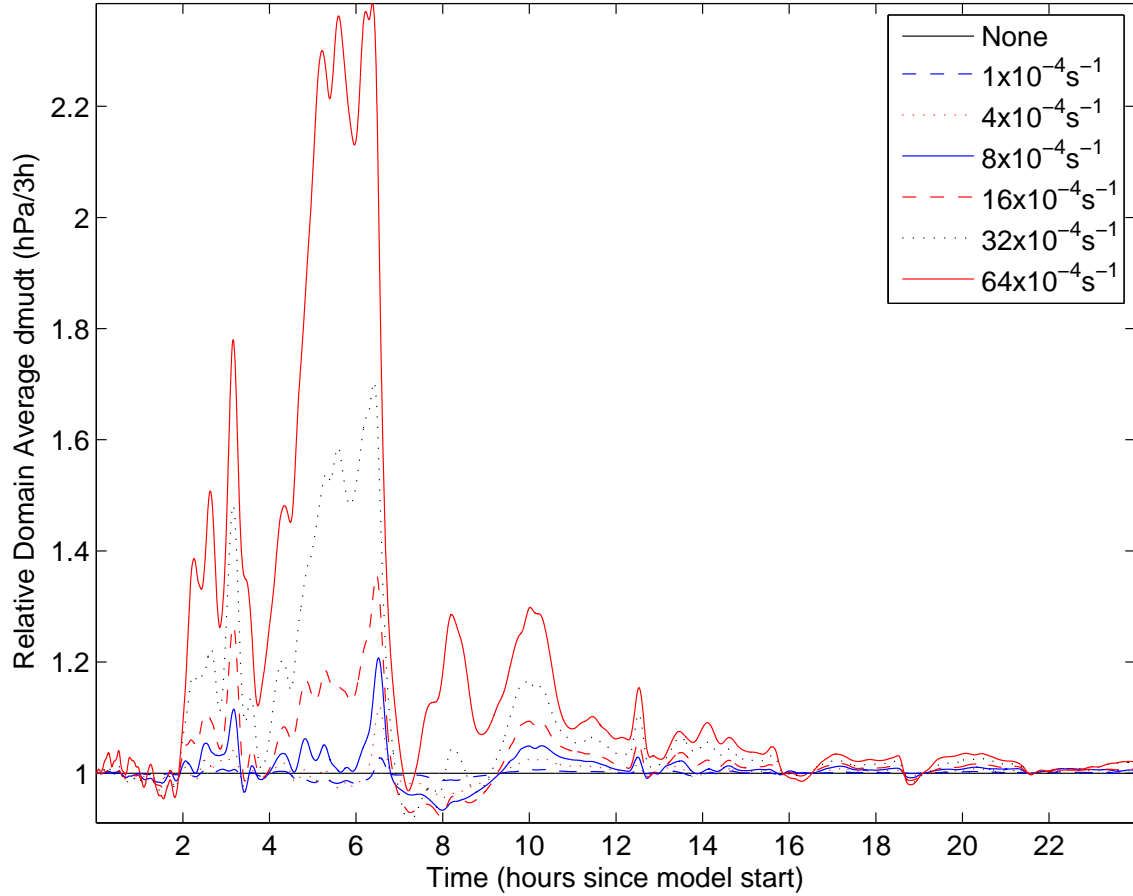


Fig. 8 Time series of 3-km domain's average tendency of perturbation dry air mass ( $d\mu/dt$ ) relative to the experiment with no data assimilation for all experiments with an *obs\_rinxy* of 60 km for 1 March 2012. A 100-point centered average was applied to smooth out the high-frequency variability.

### 5.2.2 Verification

The temperature mean absolute error (MAE) for each experiment for the first 6 h of the forecast (19–00 UTC) is shown in the left column of Fig. 9a, 9c, and 9e. Recall that a 6-hour (h) dynamic initialization using observation-nudging data assimilation precedes the beginning of the forecast. No observations during the forecast period are included in the data assimilation and so the evaluation here is against observations that were not used in the data assimilation. Also, note that verification was completed by horizontally interpolating the model to the observation location and vertically interpolating the model to the height above ground level of the observation. Figure 9a indicates that the temperature MAE in the lowest 12,000-m AGL for the first 6 h of the forecast generally decreases with increasing  $G_q$ , consistent with stronger nudging being more able to bring the model into agreement with observations; thus it provides more accurate conditions for the start of the forecast period. There are exceptions, with the temperature MAE of the 90-km and 120-km experiments higher for  $G_q = 16 \times 10^{-4} \text{ s}^{-1}$  than for  $G_q = 4$  or  $8 \times 10^{-4} \text{ s}^{-1}$ . All experiments have lower 0–12,000-m temperature MAE than the control experiment with no

data assimilation. If one excludes experiments with  $G_q > 8 \times 10^{-4} \text{ s}^{-1}$  due to the increased noise in those experiments, the best experiments are those with  $G_q$  of 4 or  $8 \times 10^{-4} \text{ s}^{-1}$  and  $obs\_rinxy$  of 90 or 120 km. (Recall that  $obs\_rinxy$  is the radius of influence just above the surface; the radius of influence increases linearly to twice this value at 500 hPa and remains at this value above 500 hPa.) For the 0–1,000-m layer for 19–00 UTC (Fig. 9c)—the layer in Fig. 2 with the most TAMDAR observations—there is a similar pattern, with temperature MAE generally decreasing with increasing  $G_q$ . The magnitude of the improvement in temperature MAE is notably larger in the 0–1,000-m layer than the 0–12,000-m layer, with the difference between the no-nudging experiment and the strongest-nudging experiment ( $64 \times 10^{-4} \text{ s}^{-1}$ )  $\approx 0.09 \text{ K}$  for 0–12,000 m, but  $0.44 \text{ K}$  for 0–1,000 m. As in the 0–12,000-m AGL layer, the best experiments with  $G_q \leq 8 \times 10^{-4} \text{ s}^{-1}$  are those with  $G_q$  of 4 or  $8 \times 10^{-4} \text{ s}^{-1}$  and  $obs\_rinxy$  of 90 or 120 km. Note that the 0–1,000-m AGL layer plots do not include surface observations, since the surface observations for 19–00 UTC are evaluated against the model 2-m AGL diagnostic temperature in Fig. 9e. For the surface observations there is a similar pattern of decreasing temperature MAE with increasing nudging strength, but the magnitude of the improvements due to nudging TAMDAR are quite small:  $0.03\text{-K}$  between the no-nudging experiment and the nudging experiment with the lowest temperature MAE in this time period. As in the 0–1,000-m and 0–12,000-m AGL layers for this time period, the temperature MAE for the experiments with  $G_q$  of 4 or  $8 \times 10^{-4} \text{ s}^{-1}$  and  $obs\_rinxy$  of 90 km are among the 4 best experiments with  $G_q \leq 8 \times 10^{-4} \text{ s}^{-1}$ ; however, instead of the similar pair of experiments with an  $obs\_rinxy$  of 120 km being part of the 4 best experiments, the pair of  $obs\_rinxy = 60\text{-km}$  experiments constitute the 2 other experiments with the lowest surface-temperature MAE for this time period. This may suggest that nudging based on the above-surface TAMDAR observations with an  $obs\_rinxy$  of 120 km spreads the influence of TAMDAR observations to areas where the surface-temperature error is not correlated with the error at the location of the TAMDAR observation. However, the very small magnitude of the differences in temperature MAEs among the experiments at the surface makes it difficult to make definite statements regarding the interpretation of the MAE differences.

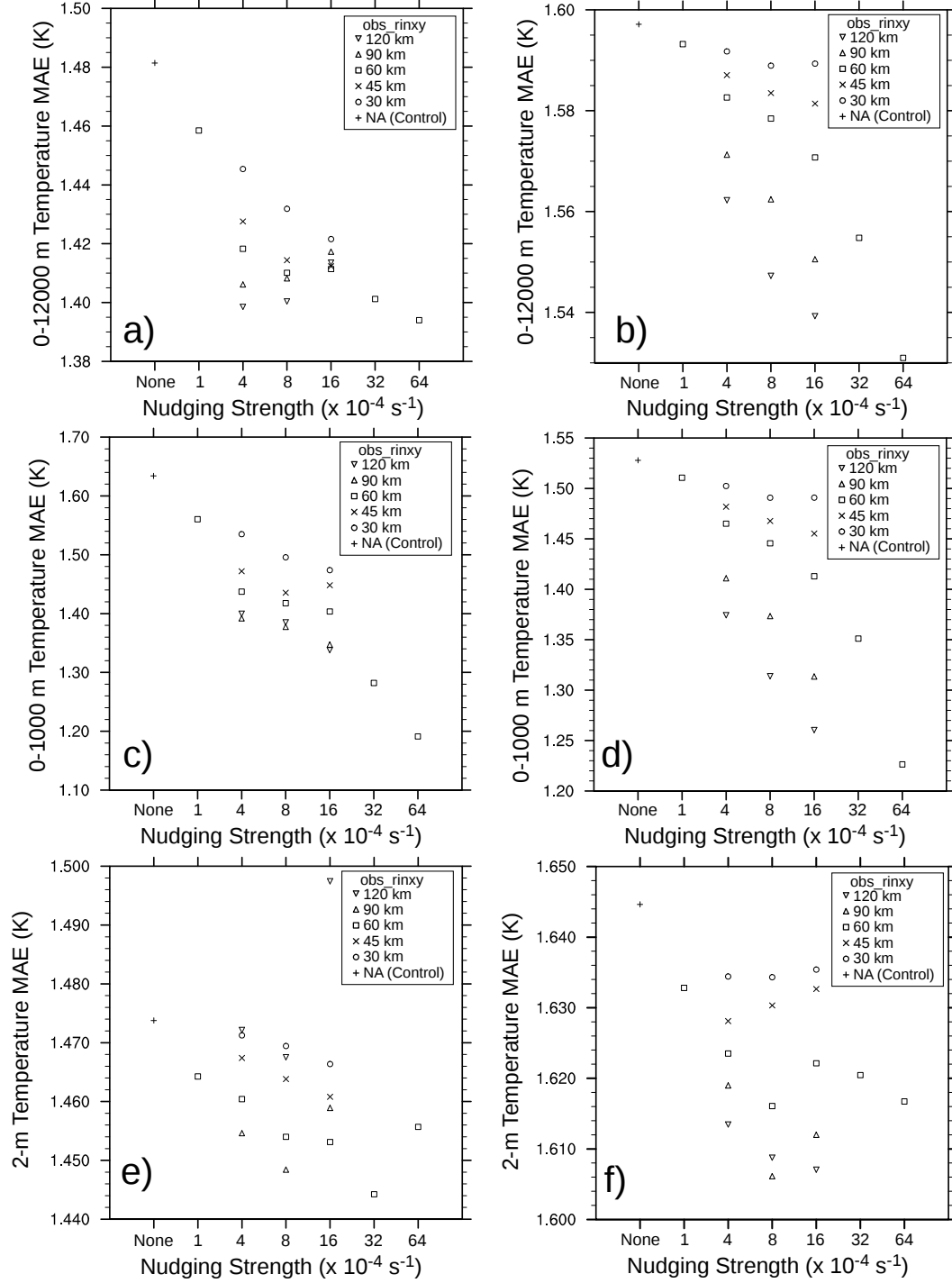


Fig. 9 Temperature MAE (K) for the experiments in Table 1: for 19–00 UTC (1–6-h forecast; a, c, e) and for 01–12 UTC (7–18-h forecast; b, d, f); at 2-m AGL (e, f), at 0–1,000-m AGL (c, d), and at 0–12,000-m AGL (a, b). The x-axis indicates the nudging strength ( $G_q$ ) of the experiment and the symbols indicate the *obs\_rinxy* setting used to determine horizontal radius of influence.

While the left column of Fig. 9 shows temperature MAE for the first 6 h of the forecast period (19–00 UTC; Fig. 9a, 9c, 9e), the right column shows the remaining portion of the forecast



period (01–12 UTC; Fig. 9b, 9d, 9f). Recall that the data assimilation only includes observations through the first 6 h (12–18 UTC) and the nudging of these observations is linearly decreased to zero by 19 UTC. One would expect that the benefits of the nudging would decrease with time and thus that the temperature MAE improvements for 01–12 UTC would be less than those for 19–00 UTC. Consistent with this expectation, the range in temperature MAE among the experiments for 19–00 UTC (Fig. 9a, 9c, 9e) is indeed larger than for 01–12 UTC (Fig. 9b, 9d, 9f). For the 01–12 UTC period, temperature MAE for experiments with  $G_q \leq 8 \times 10^{-4} \text{ s}^{-1}$  is lowest for those with  $G_q$  of 4 or  $8 \times 10^{-4} \text{ s}^{-1}$  and *obs\_rinxy* of 90 or 120 km. Unlike the 19–00 UTC period, this is also true for surface temperature.

Figure 10 contains the same format as Fig. 9 but plots the dewpoint MAE rather than the temperature MAE, and shows many similarities to the temperature MAE plots. As with temperature, dewpoint MAE generally decreases with increasing  $G_q$ , and data assimilation has a larger impact on MAE in the 0–1,000-m AGL layer than at the surface or throughout the lowest 12,000 m. However, for the entire 0–12,000-m AGL layer for the first 6 h of the forecast (Fig. 10a), dewpoint MAE increases with increasing  $G_q$  for  $G_q > 8 \times 10^{-4} \text{ s}^{-1}$ . This may suggest that water vapor is more prone to overfitting and that there is more spatial variation in water vapor than temperature. However, consistent with temperature, the experiments with  $G_q \leq 8 \times 10^{-4} \text{ s}^{-1}$  that perform the best are those with  $G_q$  of 4 or  $8 \times 10^{-4} \text{ s}^{-1}$  and *obs\_rinxy* of 90 or 120 km.

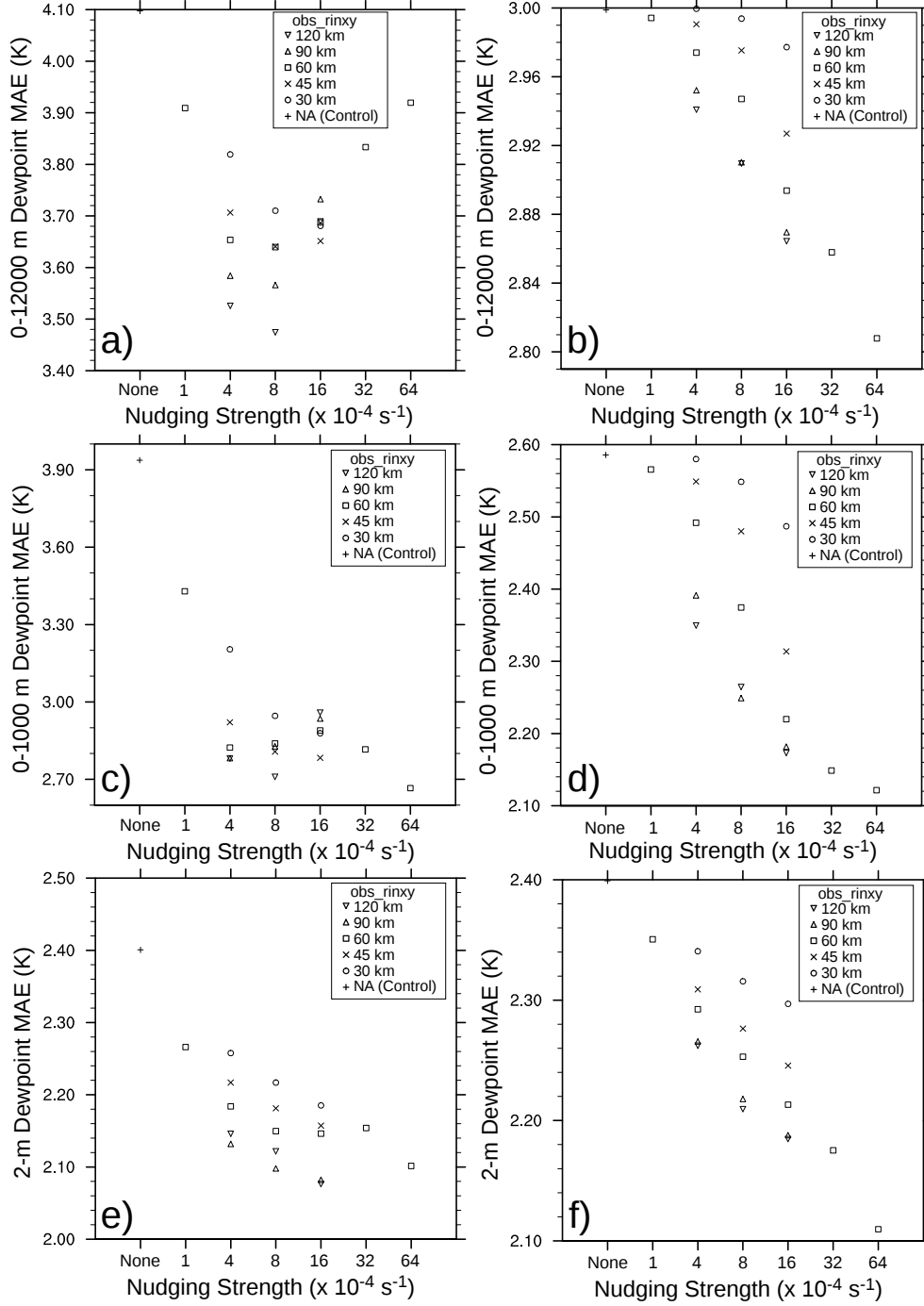


Fig. 10 Dewpoint temperature MAE (K) for the experiments in Table 1: for 19–00 UTC (1–6 h-forecast; a, c, e) and 01–12 UTC (7–18-h forecast; b, d, f); at 2-m AGL (e, f), at 0–1,000-m AGL (c, d), and at 0–12,000- m AGL (a, b). The x-axis indicates the nudging strength ( $G_d$ ) of the experiment and the symbols indicate the *obs\_rinxy* setting used to determine horizontal radius of influence.

The wind-speed MAEs in Fig. 11 and the wind-direction MAEs in Fig. 12 have patterns in the experiments that are similar to those of the dewpoint-temperature MAEs in Fig. 10. Consistent with temperature and dewpoint, wind speed and direction MAEs generally decrease with increasing nudging strength; however, similar to dewpoint MAE, wind speed and direction MAEs increase at large  $G_q$  for the first 6 h in the 0–12,000-m AGL layer (Fig. 11a and 12a). Consistent with temperature and dewpoint, the experiments with  $G_q \leq 8 \times 10^{-4} \text{ s}^{-1}$  that perform the best in wind MAE are generally those with  $G_q$  of 4 or  $8 \times 10^{-4} \text{ s}^{-1}$  and *obs\_rinxy* of 90 or 120 km. For the 0–12,000-m AGL level for 01–12 UTC, it is more difficult to determine which experiments performed best. The very small differences in MAE among many of the experiments make it likely that some of the differences are insignificant.

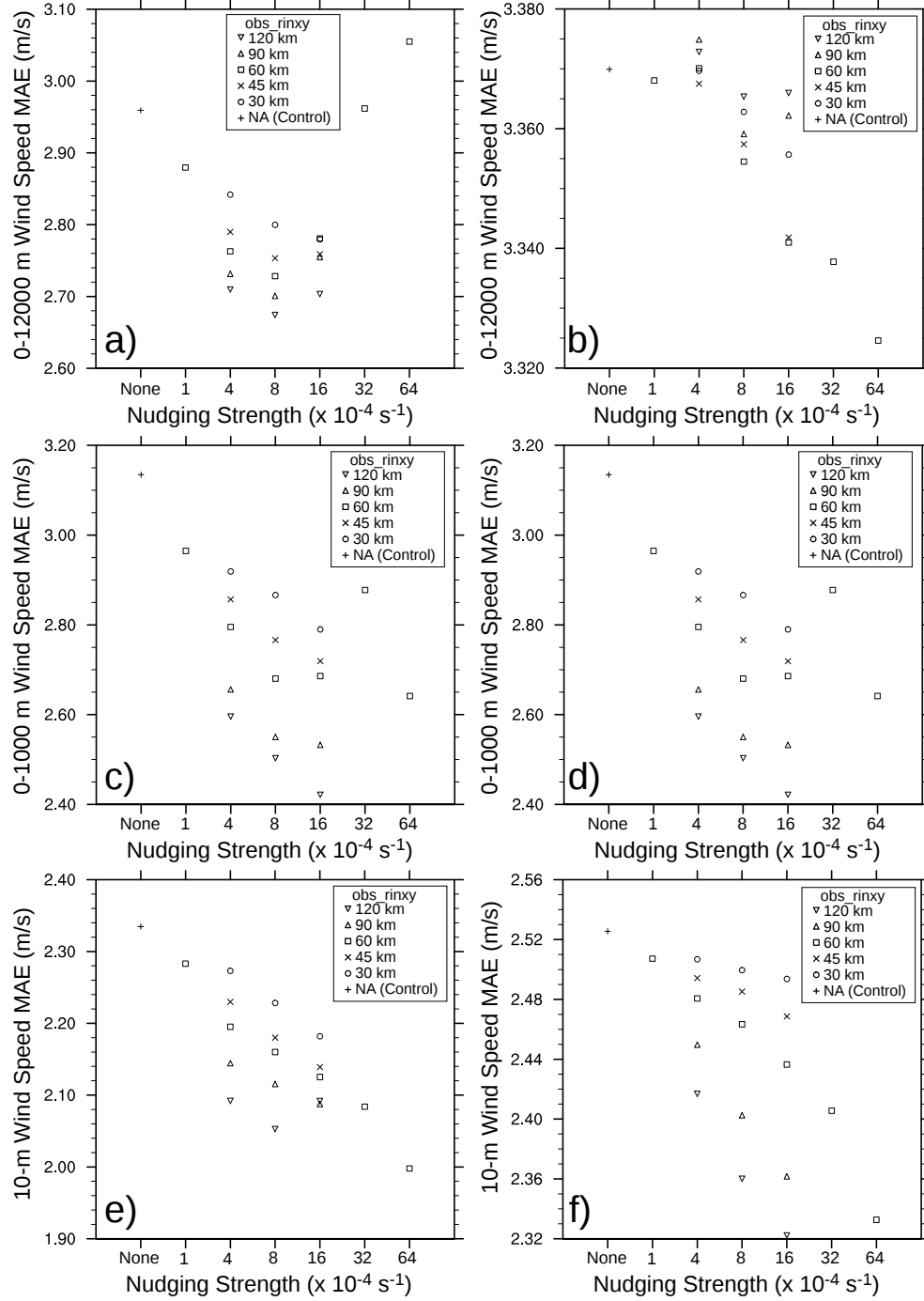


Fig. 11 Wind-speed MAE (m/s) for the experiments in Table 1: for 19–00 UTC (1–6-h forecast; a, c, e) and for 01–12 UTC (7–18-h forecast; b, d, f); at 10-m AGL (e, f), at 0–1,000-m AGL (c, d), and at 0–12,000-m AGL (a, b). The x-axis indicates the nudging strength ( $G_q$ ) of the experiment and the symbols indicate the *obs\_rinxy* setting used to determine horizontal radius of influence.

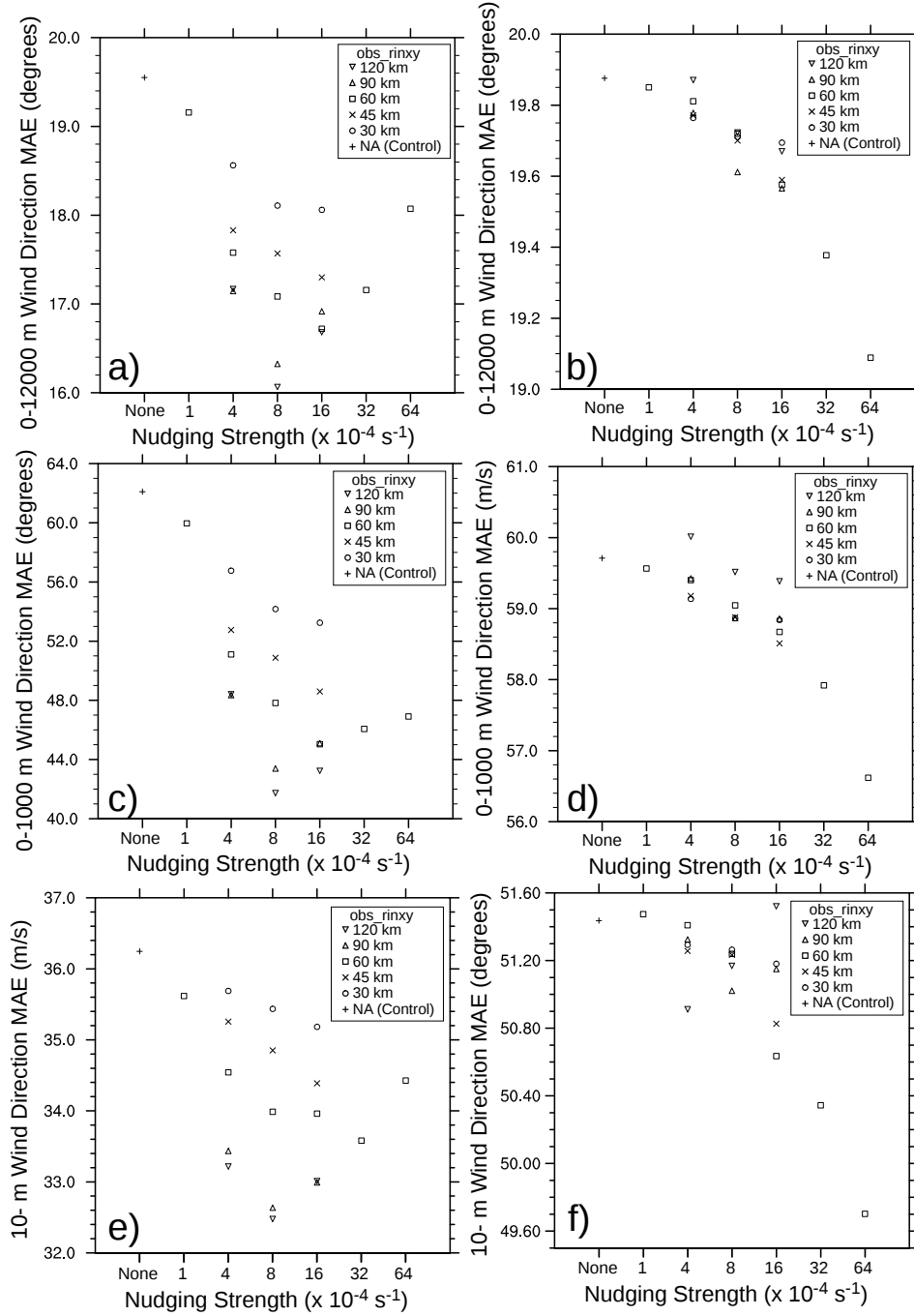


Fig. 12 Wind-direction MAE (degrees) for the experiments in Table 1: for 19–00 UTC (1–6 h-forecast; a, c, e) and for 01–12 UTC (7–18-h forecast; b, d, f); at 10-m AGL (e, f), at 0–1,000-m AGL (c, d), and at 0–12,000-m AGL (a, b). The x-axis indicates the nudging strength ( $G_q$ ) of the experiment and the symbols indicate the *obs\_rinxy* setting used to determine horizontal radius of influence.

In order to determine which of the 4 experiments performs best overall, a simple ranking was employed for each of the panels in Fig. 9–12. Thus, the ranking will consider MAE of temperature, dewpoint, wind speed, and wind direction for surface, 0–1,000-m AGL, and 0–12,000-m AGL, and for the first 6 h of the forecast and the latter portion of the forecast. The rankings for wind speed and wind direction will be ranked with half as much weight as temperature and dewpoint because they are representing 2 aspects of the same field. This ranking is shown in Table 2. It indicates the overall ranking from best to worst among the overall 4 best experiments: 1)  $G_q = 8 \times 10^{-4} \text{ s}^{-1}$  and  $obs\_rinxy = 120 \text{ km}$ , 2)  $G_q = 8 \times 10^{-4} \text{ s}^{-1}$  and  $obs\_rinxy = 90 \text{ km}$ , 3)  $G_q = 4 \times 10^{-4} \text{ s}^{-1}$  and  $obs\_rinxy = 120 \text{ km}$ , and 4)  $G_q = 4 \times 10^{-4} \text{ s}^{-1}$  and  $obs\_rinxy = 90 \text{ km}$ . This suggests that the best configuration for this case is  $G_q = 8 \times 10^{-4} \text{ s}^{-1}$  and  $obs\_rinxy = 120 \text{ km}$ . Note, however, that the  $G_q = 8 \times 10^{-4} \text{ s}^{-1}$  and  $obs\_rinxy = 90 \text{ km}$  experiment ranks very closely for temperature and is the best experiment for wind direction.

Table 2 Ranking of MAE values for the 4 experiments with the lowest MAE, with “1” being the best of the 4 experiments and “4” being the worst

			$G_q \text{ (s}^{-1}\text{)}$	$4 \times 10^{-4}$		$8 \times 10^{-4}$	
Field	Time (UTC)	Height (m AGL)	<i>obs_rinxy</i> (km)	90	120	90	120
Temp. (K)	19 - 00	0-12000		3	1	4	2
	01 - 12			4	2.5	2.5	1
	19 - 00	0-1000		3	4	1	2
	01 - 12			4	2.5	2.5	1
	19 - 00	2		2	4	1	3
	01 - 12			4	3	1	2
	Mean			3.33	2.83	2.00	1.83
Dewpoint (K)	19 - 00	0-12000		4	2.	3	1
	01 - 12			3.5	3.5	2	1
	19 - 00	0-1000		2.5	2.5	4	1
	01 - 12			3.	4	2	1
	19 - 00	2		3.	4	2	1
	01 - 12			4	3	2	1
	Mean			3.33	3.17	2.50	1.00
Wind Speed (m/s)	19 - 00	0-12000		4	3	2	1
	01 - 12			4	3	1	2
	19 - 00	0-1000		4	3	2	1
	01 - 12			4	2	3	1
	19 - 00	10		4	2	3	1
	01 - 12			4	3	2	1
	Mean			4.00	2.67	2.17	1.17
Wind Direction (degrees)	19 - 00	0-12000		3	4	2	1
	01 - 12			3	4	1	2
	19 - 00	0-1000		3.5	3.5	2	1
	01 - 12			2	4	1	3
	19 - 00	10		4	3	2	1
	01 - 12			4	1	2	3
	Mean			3.25	3.25	1.67	1.83
Wind	Wind Mean			3.63	2.96	1.92	1.50
Mean	Overall Mean			3.43	2.99	2.14	1.44

### 5.2.3 Data-Assimilation Benefit vs. Degradation

When assimilating data via observation nudging, a larger horizontal radius of influence may decrease the overall error, but do so by decreasing error near the observation while increasing error farther from the observation. To investigate this issue, we examined whether a given data-assimilation configuration improved, degraded, or caused no change in the verification of each individual observation and then determined how many observations fell into each category. “No change” was defined here as changes  $\leq 0.1$  K for temperature and dewpoint,  $\leq 0.1$  m/s for wind speed, and  $\leq 1.0^\circ$  for wind direction. Based on this information, plots are constructed of the percentage of observations where the data assimilation improved the model. Plots are also constructed that take the subset of observations where the data assimilation results in a non-negligible change (either positive or negative) and find the percentage of these observations where the change was positive. This quantity is referred to here as the percentage changed improved (PCI). A value of PCI greater than 50% indicates that where the data assimilation is changing the solution, it is more often improving the solution than degrading the solution.

For temperature in the 0–1,000-m AGL layer for 19–00 UTC, the percent of observation locations where the data assimilation improves the model solution (Fig. 13a) generally increases as nudging strength increases. This height layer and time period were chosen because the largest effects of nudging occur in these categories. Stronger nudging allows the data assimilation to more strongly affect the model at the grid points within the radius of influence; for temperature, this allows the nudging to benefit the model solution at an increasing number of observation points as  $G_q$  increases. The percent of observation locations where the model solution improves also increases with increasing *obs\_rinxy*. This indicates that nudging over a larger area allows a larger number of model grid points to improve. Note, however, that this plot says nothing about the percentage of grid points at observation locations for which the assimilation degrades the solution.

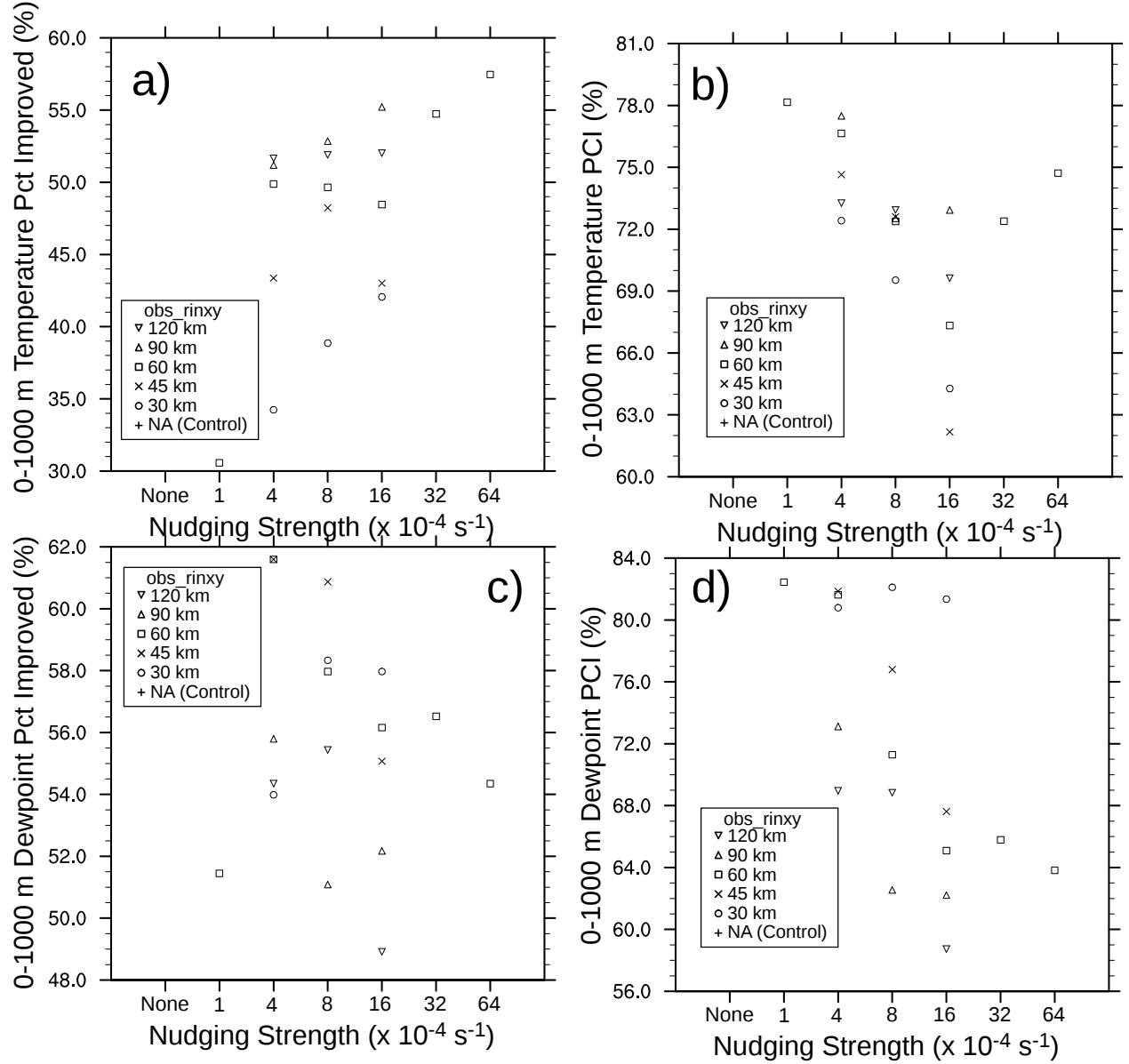


Fig. 13 The percentage of observations against which the model verifies non-negligibly better as compared to the no-nudging experiments (a, c), and of the subset of observation against which the change is an improvement (PCI; b, d). These are plotted for all experiments for the 0–1,000-m AGL level for 19–00 UTC for both temperature (a, b) and dewpoint (c, d).

The PCI plot for temperature during this time period in the 0–1,000-m AGL layer (Fig. 13b) takes into account both the improvements and the degradations caused by the data assimilation. In general, the PCI decreases with increasing nudging strength, suggesting although nudging more strongly increases the number of grid points where the model solution improves, there is a stronger increase in the number of grid points where the model solution degrades. For the very strongest nudging ( $G_q \geq 16 \times 10^{-4} \text{ s}^{-1}$ ) the PCI increases; however, since there are only experiments for one *obs\_rinxy* for these values of  $G_q$  and this is only one time period of one case



at one height level, perhaps this is an anomaly. One might expect that PCI would decrease with increasing *obs\_rinxy*, because with smaller *obs\_rinxy* we will confine the changes due to nudging to a smaller area around the observation, and the error at the observation location is more likely to be correlated with error at correlations closer to the observation location. However, for temperature in this case, during this time period and vertical layer, this is not the case. There is not a clear relationship between *obs\_rinxy* and PCI here. For  $G_q = 4$  and  $16 \times 10^{-4} \text{ s}^{-1}$ , an *obs\_rinxy* of 90 km results in the best PCI, while at  $8 \times 10^{-4} \text{ s}^{-1}$  all but *obs\_rinxy* = 30 km have a similar PCI.

Unlike temperature, for dewpoint the percent of observation locations where the model improves (Fig. 13c) does not generally increase with increasing  $G_q$  or with increasing *obs\_rinxy*. There is no obvious relationship between the  $G_q$  and the percent improved, but the larger values of *obs\_rinxy* are generally associated with lower percentages of observation locations where the model improves. This suggests that increasing the area over which a moisture observation affects the solution can degrade the solution, at least for the larger of the values of *obs\_rinxy* tested here. Comparing these results for moisture (Fig. 13c) to those for temperature (Fig. 13a) suggests that the horizontal error-correlation length scales for moisture may be smaller than those for temperature.

For dewpoint PCI (Fig. 13d), we do see the increase in PCI with decreasing *obs\_rinxy* that one might expect but that was not present for temperature. The largest dewpoint PCIs in this layer at this time are for the smaller values of *obs\_rinxy*. At  $G_q = 4 \times 10^{-4} \text{ s}^{-1}$  the experiments with *obs\_rinxy* = 30–60 km have very similar PCIs ( $\approx 80\%$ ), while the PCI for *obs\_rinxy* = 90 km is  $\approx 73\%$  and for *obs\_rinxy* = 120 km the PCI is  $\approx 69\%$ . At  $G_q = 8 \times 10^{-4} \text{ s}^{-1}$  the PCI for the experiments with *obs\_rinxy* = 30, 45, 60, 90, and 120 km are approximately 82%, 77%, 71%, 62%, and 69%, respectively. These results are consistent with the percent-improved statistics in Fig. 13c in suggesting that the horizontal error-correlation length scales are smaller for moisture than for temperature.

Like dewpoint but unlike temperature, the percent of observation locations where the model wind speed (Fig. 14a) and direction (Fig. 14c) are improved by observation nudging does not show a general increase with  $G_q$ . However, similar to temperature, wind speed (and to a lesser degree, wind direction) generally indicates a larger percentage of model grid points coincident with observations are improved for larger values of *obs\_rinxy*. This suggests that the error-correlation length scales of wind are perhaps more similar to those of temperature than those of water vapor.

It is difficult to see a pattern in the wind speed and wind direction PCIs (Fig. 14b and 14d). Smaller values of *obs\_rinxy* are generally associated with smaller PCIs (at least at  $G_q = 4$  and  $8 \times 10^{-4} \text{ s}^{-1}$ ), which is in contrast to the opposite signal seen in dewpoint (Fig. 13c). This is also consistent with the wind error-correlation length scales perhaps being closer to those for temperature than moisture.

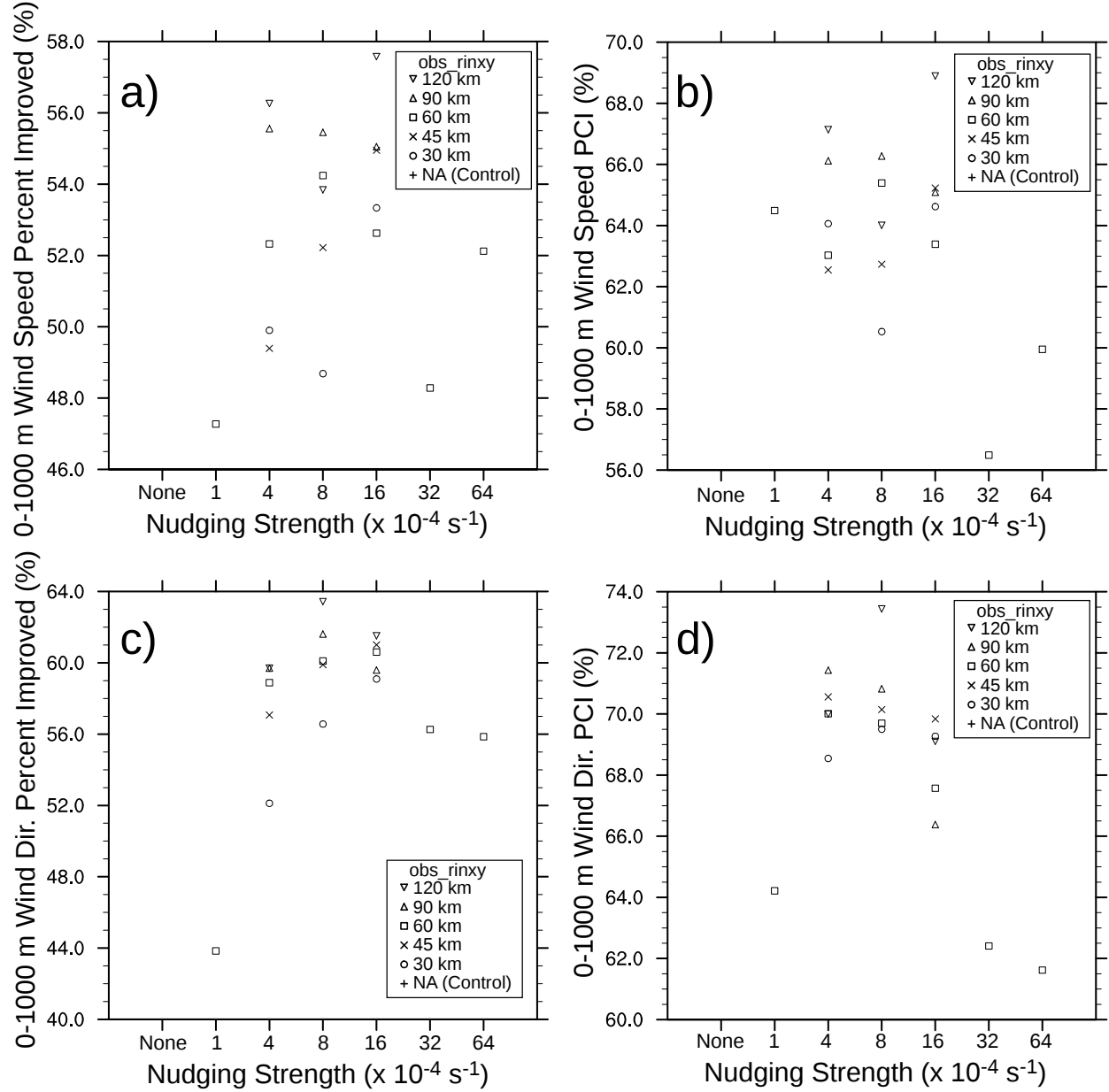


Fig. 14 The percentage of observations against which the model verifies non-negligibly better as compared to the no-nudging experiments (a, c), and of the subset of observations against which the model verifies non-negligibly differently than the no-nudging experiments, the percentage for which the change is an improvement (PCI; b, d). These are plotted for all experiments for the 0–1,000-m AGL level for 19–00 UTC for both wind speed (a, b) and wind direction (c, d).

### 5.3 Summary and Conclusions

A set of observation-nudging experiments were completed to determine how to configure observation nudging for assimilating TAMDAR data. These were conducted for 1 March 2012 for a region centered over southern California using 9-km and 3-km horizontal grid-spacing domains. The experiments vary the strength of the nudging ( $G_q$ ) and the area over which an observation affected the model solution (*obs\_rinxy*). Recall that *obs\_rinxy* gives the radius of

influence immediately above the surface but the radius of influence increases linearly with decreasing pressure until reaching twice the value of *obs\_rinxy* at 500 hPa and above.

Three methods were used to evaluate the experiments. First, the “noise” caused by the data assimilation was evaluated to determine which experiments contain unacceptable levels of model noise that suggest the data assimilation is degrading the model solution. This evaluation of the noise caused by the observation nudging indicates that in order to minimize noise, it is probably best to use experiments  $G_q \leq 8 \times 10^{-4} \text{ s}^{-1}$ . Second, the mean absolute errors of temperature, dewpoint, wind speed, and wind direction were evaluated during the model forecast (after the completion of the model preforecast). This evaluation indicated that the largest effects of observation nudging are in the first 6 h of the forecast (compared to the latter 11 h) and in the lowest 1,000 m of the atmosphere above the surface (compared to the surface and to the entire 0–12,000-m AGL layer). The experiment with the best overall MAE is the experiment with  $G_q = 8 \times 10^{-4} \text{ s}^{-1}$  and *obs\_rinxy* = 120 km, with the next best experiment also with  $G_q = 8 \times 10^{-4} \text{ s}^{-1}$  but with *obs\_rinxy* = 90 km. Third, we examined the relationship between the number of observations indicating the model forecast improved and the number of observations indicating the model forecast degraded. This analysis suggested that the error-correlation length scale of water vapor is likely smaller than that of temperature and wind. Due to this, it may be best to use the experiment found to have the second-smallest MAE because it has a smaller value of *obs\_rinxy* than the experiment with the lowest MAE; namely, the experiment with  $G_q = 8 \times 10^{-4} \text{ s}^{-1}$  and with *obs\_rinxy* = 90 km. Future experiments exploring the ability to use a different horizontal radius of influence for different variables could result in further improvements in model forecasts.

It is important to note that these results are from a single case day, and their generality is not known. The next section will include tests of using the  $G_q = 8 \times 10^{-4} \text{ s}^{-1}$  and *obs\_rinxy* = 90 km for 4 other case days.

---

## 6. Exploring the Value of Various Observational Data Sources

---

### 6.1 Experimental Design

In order to determine the relative value of TAMDAR observations as well as other observations, a series of model experiments utilizing the 9-, 3-, and 1-km horizontal grid-spacing domains were completed for the 5 case days from 2012 (described in Section 3): 7 February, 9 February, 16 February, 1 March, and 5 March. These experiments are designed to apply the lessons learned (in Section 5) assimilating TAMDAR observations on one case day on the 3-km domain to the task of creating the best possible model forecast.

As noted in Table 3, there are 7 experiments for each case day. Experiment C is the control experiment and assimilates no observations via observation; it also used GFS data for initial

conditions with no enhancement via observations. Experiment T uses observation nudging to assimilate only the TAMDAR observations; it also uses TAMDAR data to enhance the initial condition analysis from GFS. (Note that all experiments use initial conditions consisting of GFS data enhanced by the observations being assimilated in that experiment.) The value of assimilating “standard” observations is explored in Exp. S. There, standard observations refer to standard surface observations and rawinsonde observations (RAOBs). These are the observations included in the MADIS METAR (Aviation Routine Weather Report), maritime, and RAOB data sets. The METAR data set consists of stations reporting surface observations in the METAR format (including Automated Surface Observing System [ASOS], Automated Weather Observing System [AWOS], and non-automated stations). The maritime data set consists of reports from ships. The RAOB data set contains rawinsondes. The added value of TAMDAR observations compared to only using standard observations is demonstrated via comparing Exp. TS to Exp. S.

Table 3 Experimental design for Section 6 indicating which observations are assimilated in each experiment (“Y” is yes)

Exp. Name	Observations Assimilated			
	Standard	KNKX	TAMDAR	Mesonet
C				
T			Y	
S	Y	Y		
TS	Y	Y	Y	
SK	Y			
TSK	Y		Y	
SM	Y	Y		Y

In order to determine the added value of having a local rawinsonde, an experiment using the standard observations but omitting the Miramar, CA, rawinsonde (KNKX), was completed (Exp. SK). A similar experiment was completed that also used the TAMDAR data to see if the TAMDAR data could serve as a replacement for the rawinsonde data. Finally, Exp. SM investigates the added value of more dense surface observations by using the MADIS mesonet data set in addition to the standard observations.

For each experiment, observation nudging was applied on all 3 domains for observations no later than 18 UTC, 6 h into the model integration. The strength of the observation nudging of observations no later than 18 UTC was then linearly decreased to zero between 18 UTC and 19 UTC (multiplied by the temporal weighting functions applied to the individual observations based on the difference between the observation time and the current model time). A  $G_q$  of  $8 \times 10^{-4} \text{ s}^{-1}$  and an *obs\_rinxy* of 90 km was used on the 3-km domain, based on the results in Section 5. Note that although the *obs\_rinxy* of 120 km led to lower overall MAE, there were indications that 120 km may be larger than the error-correlation length scale for water vapor. Therefore, the experiment with the second-best MAE was utilized here since it had a lower *obs\_rinxy*, and thus will be less likely to spread the influence of water-vapor observations over too large of an area.

The same nudging strength was also applied to the 9- and 1-km domains. Because the experiments in Section 5 did not utilize observation nudging on the 9- or 1-km domains, they do not provide direct guidance on the best *obs\_rinxy* to apply on those domains. Therefore, we have used twice the *obs\_rinxy* on 9-km domain than on the 3-km and one-half the *obs\_rinxy* on the 1-km as on the 3-km domain. This is designed to account for the smaller-scale features that are resolvable on finer-resolution model forecasts that may result in smaller error-correlation length scales. The horizontal radius of influence used for surface observations is 0.7 times *obs\_rinxy*. Full weighting is given to the innovation based on an observation for a 90-minute period centered on the observation time, with weighting linearly decreasing to zero in the 45-minute period before and after the full weighting period. For surface observations this is decreased to a 68-minute period centered on the observation time, with weighting linearly decreasing to zero in the  $\approx 34$ -minute period before and after the full weighting period.

Note that Exp. T is similar to the  $G_q = 8 \times 10^{-4} \text{ s}^{-1}$ , *obs\_rinxy* = 90 km experiment in Section 5 but differs in a few potentially important ways. Here, the initial conditions at the beginning of the nudging period are enhanced by completing an analysis in Obsgrid that incorporates observations onto the GFS analysis, but in Section 5, the GFS analyses are used without enhancement. Another difference is that here we use data assimilation on all of the domains, whereas in Section 5 data assimilation was used only on the 3-km domain. These 2 differences may potentially affect the 3-km solution in significant ways. Another difference is that here we include a 1-km nest, whereas in Section 5 only 9- and 3-km nests were utilized. We also do not use the observation-nudging modifications that ameliorate the creation of very dry conditions in these three-domain experiments. Note also that in Section 5 we only used model forecasts from one of the 5 case days, whereas here all 5 case days were simulated.

## 6.2 Results

### 6.2.1 Value of TAMDAR Observations

In order to evaluate the value of TAMDAR observations, the control experiment with no data assimilation (Exp. C) will be compared to Exp. T, which nudges only TAMDAR observations; Exp. S, which nudges only standard observations; and Exp. TS, which assimilates both standard and TAMDAR observations. Comparing Exp. T to Exp. C demonstrates the value of TAMDAR observations if there are no other observations available. Comparing Exp. TS to Exp. S demonstrates the added value of TAMDAR observations as compared to assimilating the standard observations.

Since TAMDAR observations are not available on the 1-km domain during the data assimilation period, initial evaluation of the impacts of assimilating TAMDAR data will be completed using the 3-km domain. Following this an evaluation of the effects of TAMDAR data on the 1-km domain will be completed. These effects will occur entirely through differences in the lateral boundary conditions fed from the 3-km domain to the 1-km domain.

### 6.2.1.1 Three-kilometer Domain

Figure 15 shows the MAEs for the vertical layer (0–1,000-m AGL) and time period (19–00 UTC, forecast h 1–6) likely to be most impacted from assimilating TAMDAR observations, given that there are more TAMDAR observations in this layer than in any other 1,000-m layer and that this time period immediately follows the end of data assimilation. The case day examined in Section 5 was 1 March. There is notable improvement on this case day in temperature from the inclusion of TAMDAR data; compare the square in the column for Exp. C with the square in the column for Exp. T in Fig. 15a. On 1 March, utilizing only standard data (compare Exp. S to Exp. C) actually degraded the model temperature forecast above the surface from 0–1,000 m during the first 6 h of the forecast. Adding the TAMDAR data to the standard data (Exp. TS) improves the solution compared to the standard-data-only solution and less so compared to the no-nudging experiment. The TAMDAR-only nudging experiment (Exp. T) best predicts temperature on this case day for this time and vertical bin. Looking at the other case days, the value of the TAMDAR observations for improving forecast temperature for this time and vertical bin is much less clear. In fact, on 3 case days assimilating only TAMDAR data slightly degrades the temperature forecast. That the forecast is unimproved via data assimilation is not limited to TAMDAR data: While assimilating only standard data results yields a clear improvement on 3 case days (7 February, 9 February, and 16 February), it degrades the forecast on one case day (1 March) and makes very little difference on another (5 March). The addition of TAMDAR data to standard data (Exp. TS compared to Exp. S) is a clear benefit on 2 days (1 March, 5 March), a slight benefit on one day (16 February), a slight degradation on one day (7 February), and a small degradation on the final day (9 February).

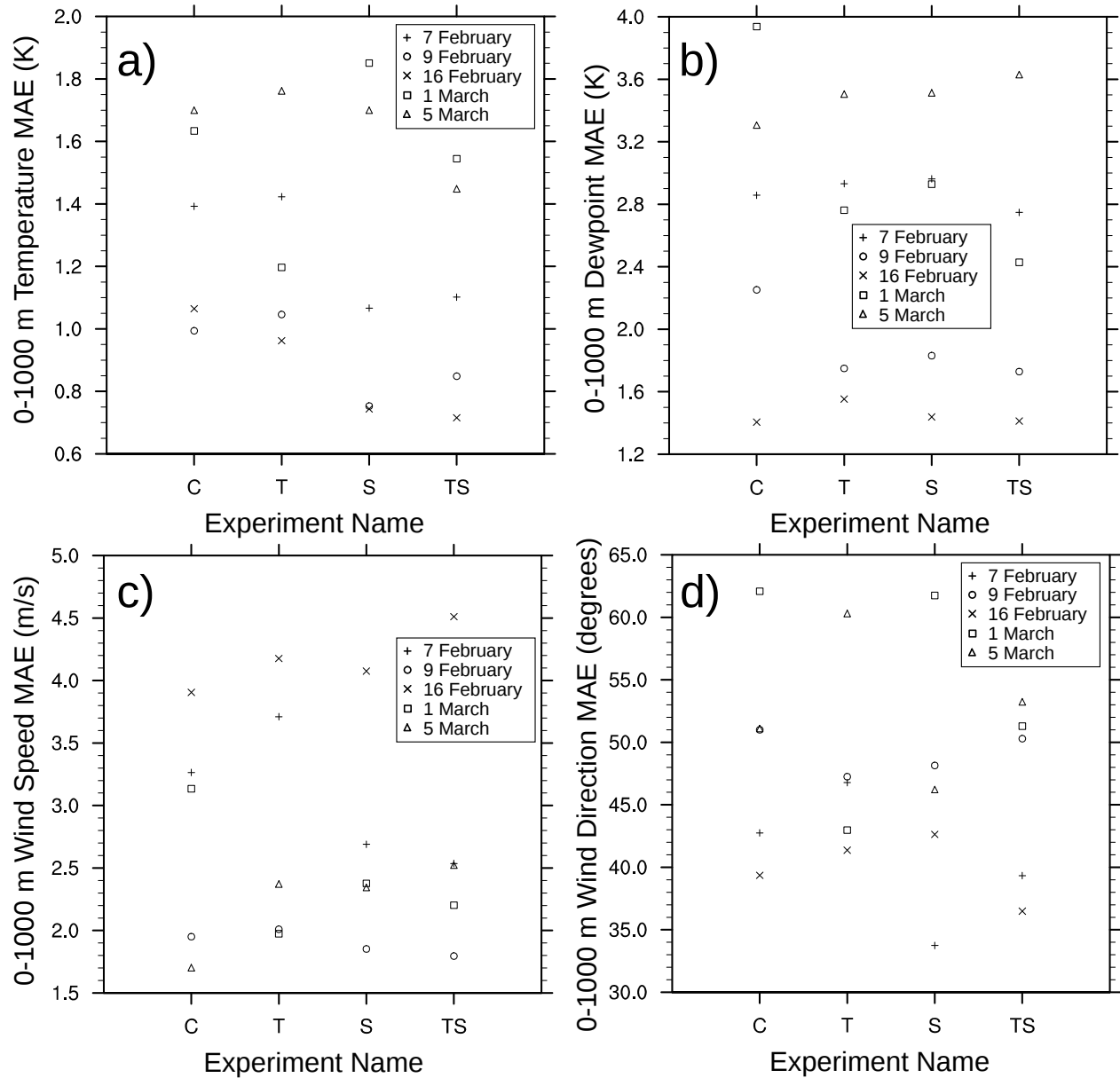


Fig. 15 WRF 3-km domain MAEs for Exp. C, T, S, and TS from Table 3 verified against non-surface observations in the 0–1,000-m AGL layer for 19–00 UTC for a) temperature, b) dewpoint, c) wind speed, and d) wind direction. The x-axis indicates the experiment’s name and the symbols indicate the case day of the experiment.

For dewpoint (Fig. 15b), the best improvement from TAMDAR data is once again on 1 March (the day examined in Section 5). Assimilating only TAMDAR data benefits 2 of the cases; however, only one of the 5 case days (16 February) indicates that nudging only TAMDAR data (Exp. T) performs worse than the assimilation of only standard observations. Similarly, adding TAMDAR data to the standard data only degrades one case day (5 March).

Wind-speed and wind-direction MAEs for 0–1,000-m AGL for the first 6 h of the forecast (Fig. 15c and 15d) show results similar to those of temperature and dewpoint. For both wind speed

and direction, 1 March is the case day when assimilating only TAMDAR data is the most beneficial, while some case days indicate degradations from the use of TAMDAR data (whether alone or in concert with standard data).

In order to more effectively analyze the potential benefits of TAMDAR-data assimilation, plots were created indicating the added value of assimilating TAMDAR data. Figures 16 and 17 demonstrate the potential benefits of assimilating TAMDAR data based on the difference in MAE between experiments with TAMDAR data and those without TAMDAR data for the first 6 h of the forecast period (19–00 UTC). If a column in these figures was labeled “A-B”, a point above the horizontal line indicating a zero MAE difference represents a case day when experiment B had a lower MAE than experiment A and thus experiment B performed better than experiment A. Figure 16a indicates that, averaged over the case days, the 1–6 h forecasts improve due to the assimilation of TAMDAR data compared to not nudging at all (Exp. C-T) and compared to nudging only standard data (S-TS), as seen by the mean value always being above the zero temperature MAE difference horizontal line. Note, however, that there is variation from day to day, with some days indicating small degradations due to nudging TAMDAR data for certain heights. The TAMDAR-data assimilation never increases the domain-average MAE by more than 0.1 K, while it sometimes does cause improvements of more than 0.1 K. For dewpoint (Fig. 16b), TAMDAR-data assimilation once again has, in general, a positive impact on dewpoint. As with temperature, there is notable variation from day to day. Perhaps the most striking variation is for the 0–1,000-m AGL layer, where the use of TAMDAR observations when compared to not doing data assimilation (Exp. C-T) decreased the dewpoint MAE by  $\approx 1.2$  K on 1 March, but increased the error by  $\approx 0.2$  K on 5 March.



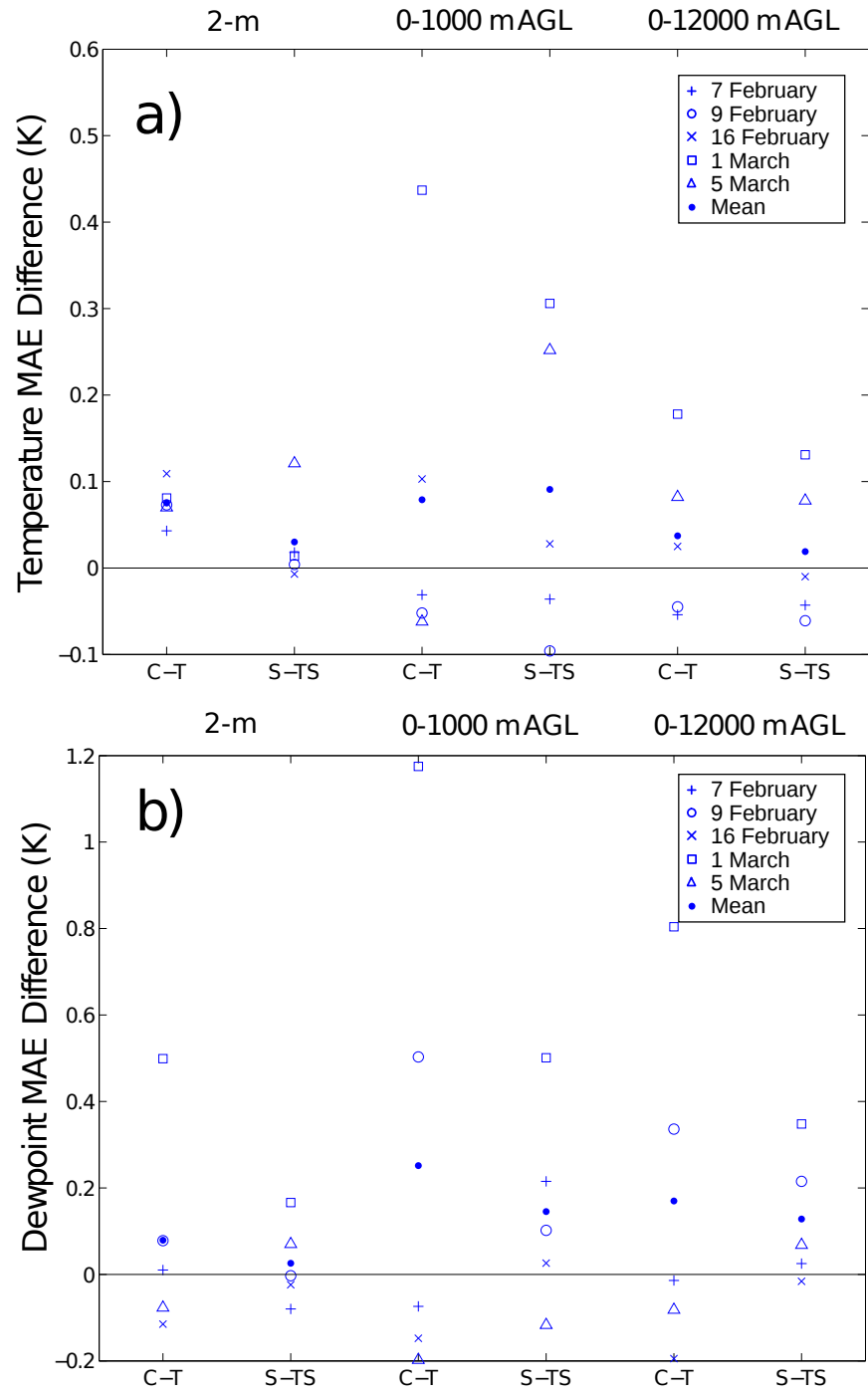


Fig. 16 Difference in MAE between Exp. C and Exp. T (columns labeled C-T) and between Exp. S and Exp. TS (columns labeled S-TS) for 19–00 UTC for 2 m, 0–1,000-m AGL, and 0–12,000-m AGL on the 3-km domain for a) temperature and b) dewpoint. Positive values indicate Exp. T performs better than Exp. C and that Exp. TS performs better than Exp. S, respectively. A point is plotted for each case day as well as the mean of all of the case days, as noted in the figure legend.

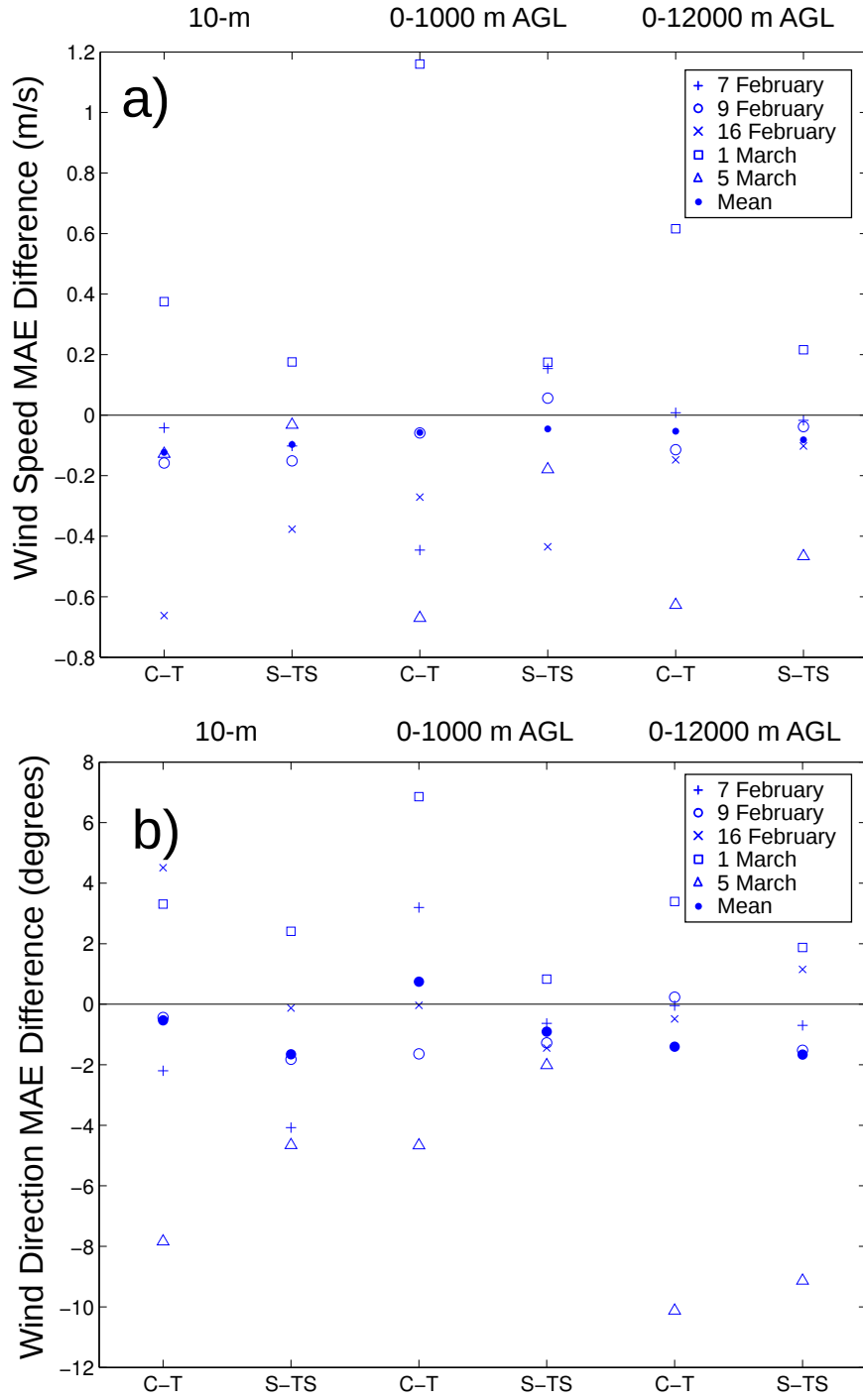


Fig. 17 Difference in MAE between Exp. C and Exp. T (columns labeled C-T) and between Exp. S and Exp. TS (columns labeled S-TS) for 19–00 UTC for 10 m, 0–1,000-m AGL, and 0–12,000-m AGL on the 3-km domain for a) wind speed and b) wind direction. Positive values indicate Exp. T performs better than Exp. C and that Exp. TS performs better than Exp. S, respectively. A point is plotted for each case day as well as the mean of all of the case days, as noted in the figure legend.

Figure 17 indicates that, on average, assimilation of TAMDAR data degrades wind speed and wind direction in the first 6 h of the forecast (19–00 UTC). The 1 March case is a notable exception: Both wind speed and wind direction are improved for all height bins, both when comparing TAMDAR assimilation to no assimilation (C-T) and when comparing TAMDAR assimilation to assimilation of only standard observations. Because the average degradation caused in the wind fields is relatively small ( $\approx 0.1$  m/s and  $\approx 2^\circ$ ) these results may not be significant.

We have been analyzing the model performance for the first 6 h of the forecast (19–00 UTC) which is the portion of the forecast period when the impacts of the nudging should be strongest; next, we investigate the impacts on the rest of the forecast period (01–12 UTC; 7–18-h forecast). Figure 18 shows the MAE difference caused by utilizing TAMDAR observations in the 0–1,000-m AGL layer (excluding surface observations). For temperature (Fig. 18a) and dewpoint (Fig. 18b) forecasts, using TAMDAR data on average resulted in small improvements: a decrease in case-day mean MAE of  $\approx 0.1$  K for temperature and  $\approx 0.1$  K for dewpoint when TAMDAR is added to standard observations; however, there is very little improvement in dewpoint when assimilating TAMDAR observations is compared to not assimilating any observations. For wind speed (Fig. 18c) there is a small improvement in the case-day mean MAE of  $\approx 0.25$  m/s when the use of TAMDAR data is compared to non-use of any observations (C-T) and  $\approx 0.1$  m/s when using TAMDAR data in addition to standard data (S-TS). For wind direction (Fig. 18d), the MAE differences due to the use of TAMDAR data averaged over the 5 cases days are very small ( $\leq 1^\circ$ ). For the 7–18-h forecast, the use of TAMDAR data, on average, results in small improvements.

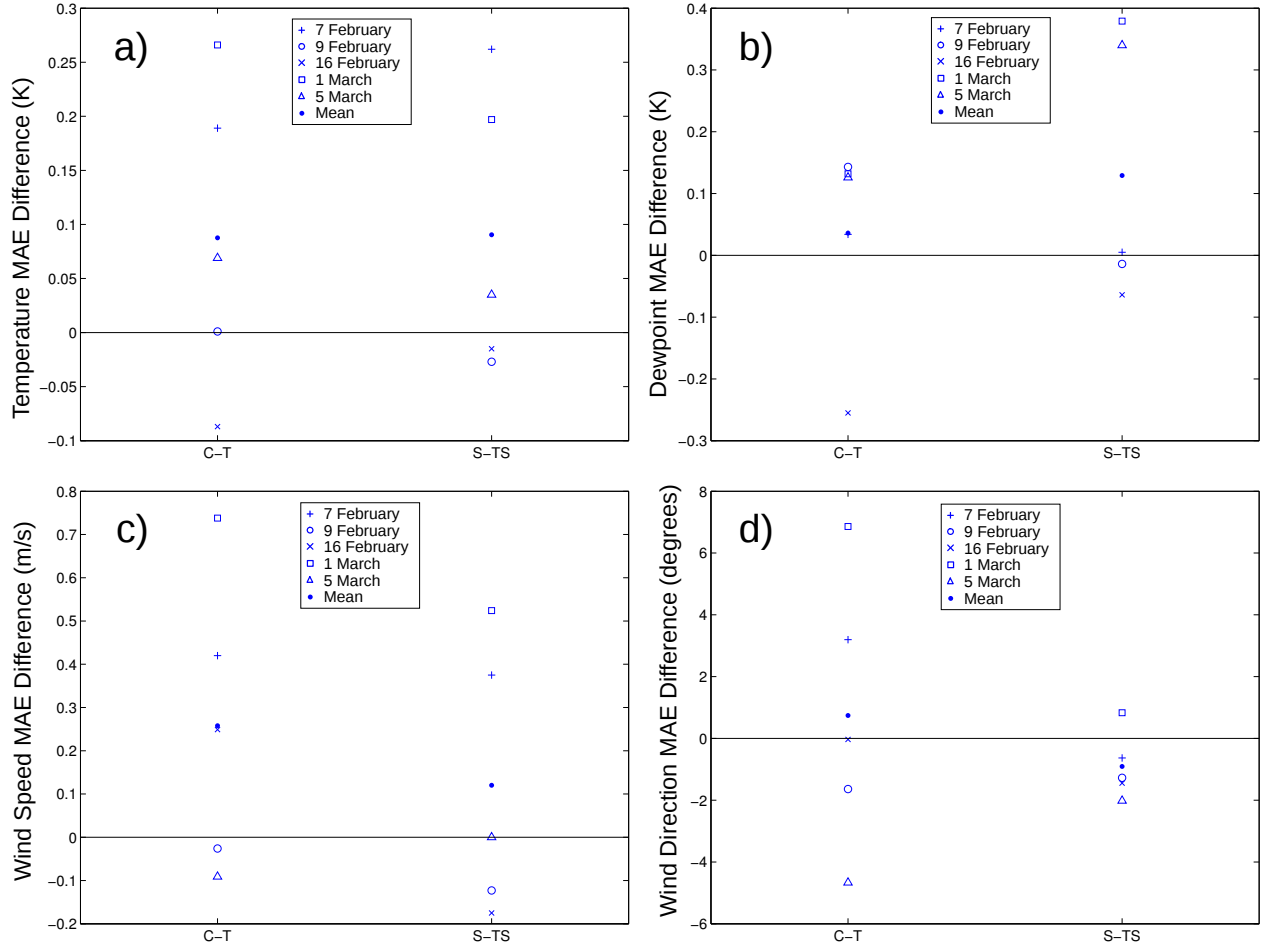


Fig. 18 Difference in MAE between Exp. C and Exp. T (columns labeled C-T) and between Exp. S and Exp. TS (columns labeled S-TS) for 01–12 UTC for, 0–1,000-m AGL on the 3-km domain for a) temperature, b) dewpoint, c) wind speed, and d) wind direction. Positive values indicate Exp. T performs better than Exp. C and that Exp. TS performs better than Exp. S, respectively. A point is plotted for each case day as well as the mean of all of the case days, as noted in the figure legend.

Overall, assimilating TAMDAR data improved the 3-km forecast of temperature and dewpoint, especially during the first 6 h of the forecast, while the overall impact on wind was less clear. During the first 6 h of the forecast, assimilation of TAMDAR data degrades the case-day mean wind forecast; during the latter 11 h, the wind speed is improved while the case-day mean wind-direction MAE is impacted very little by the TAMDAR data. It should be stressed that there is significant variability among the case days, in these results.

#### 6.2.1.2 One-kilometer Domain

Since there are no TAMDAR observations available within the 1-km domain to assimilate, the impacts of TAMDAR observations will be through the lateral boundary conditions. Note that care should be taken when comparing the 1-km verification statistics against the 3-km verification statistics because the 1-km grid covers a small subset of the 3-km grid; thus the verifications of the 2 grids are over different areas. It may be that the verification statistics of the

2 domains would be more similar if the 3-km grid were verified only over the portion of the 3-km domain coincident with the 1-km grid.

Figure 19 shows the 1-km MAE for the 0–1,000-m AGL layer during the first 6 h of the forecast. This is similar to Fig. 15 but shows the verification for the 1-km domain instead of 3-km domain. The use of TAMDAR observations (Exp. T), compared to not using any observations (Exp. C), improves model forecast temperature (Fig. 19a) for this layer and time for 3 of the 5 cases, with the other 2 cases showing very slight degradations from the use of the TAMDAR data. Using TAMDAR observations in addition to normal observations (compare Exp. S to Exp. TS) indicates that temperature forecasts are improved in this layer for 2 case days (1 March and 5 March), slightly improved in one case (16 February), slightly degraded in one case (7 February), and almost unchanged for the other case (9 February). For dewpoint (Fig. 19b) there does not appear to be a benefit compared to using no observations; when compared to assimilating only standard observations, however, there is a small benefit. Whether TAMDAR improves or degrades the wind is dependent on the specific case. The MAE differences will be plotted as with the 3-km domain in order to aid with the model analysis.

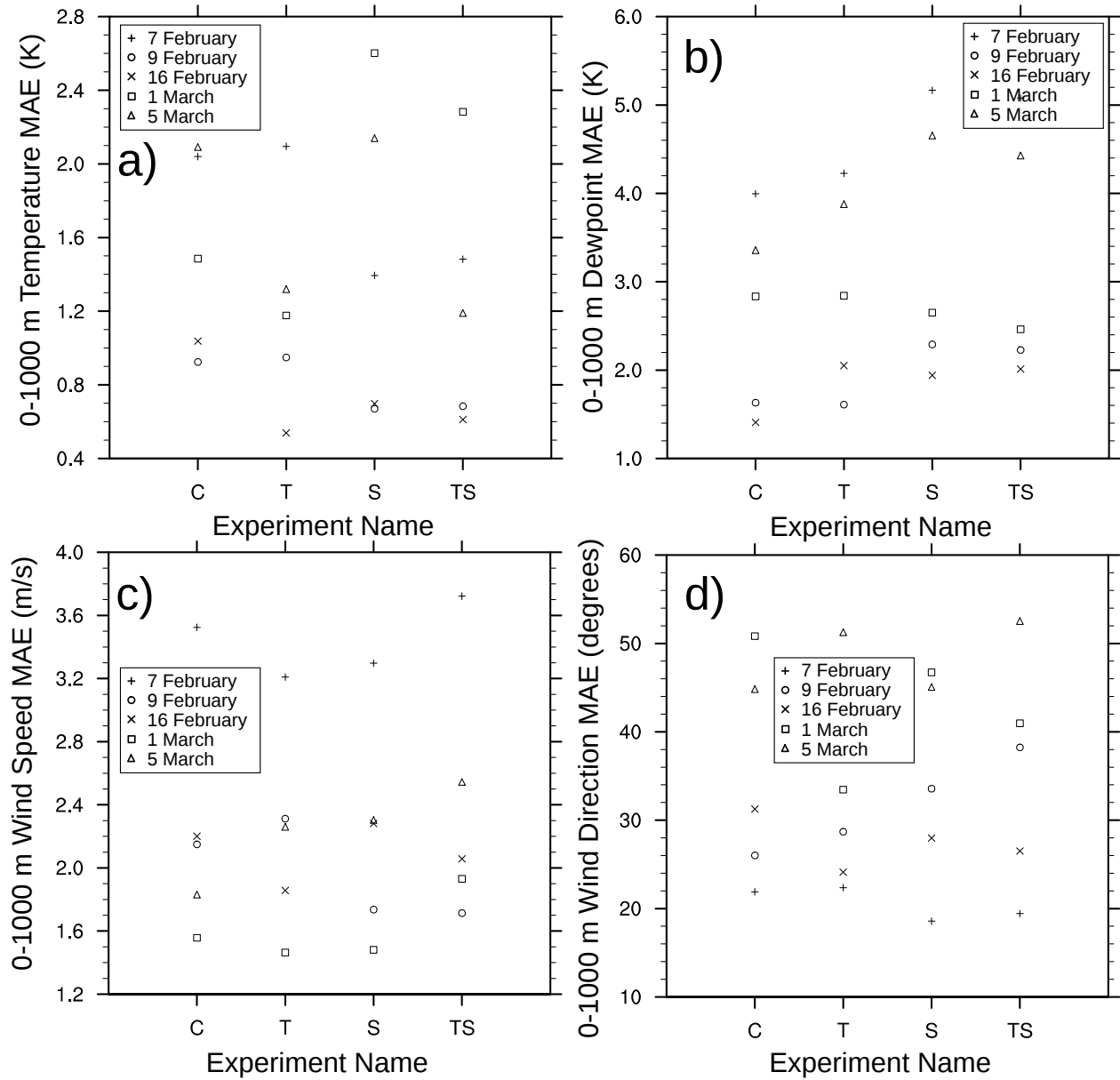


Fig. 19 WRF 1-km domain MAE for experiments C, T, S, and TS from Table 3 verified against non-surface observations in the 0–1,000-m AGL layer for 19–00 UTC for a) temperature, b) dewpoint, c) wind speed, and d) wind direction. The x-axis indicates the experiment’s name and the symbols indicate the case day of the experiment.

The case day’s mean temperature MAE difference (Fig. 20a) indicates that on average TAMDAR assimilation improves the 1-km temperature forecast for 19–00 UTC. As on the 3-km domain, there is notable variability among the case days. For dewpoint (Fig. 20b) the case-day mean MAE difference is positive for some measures and negative for others. This indicates that the TAMDAR-data assimilation neither clearly benefits nor clearly degrades the 1-km domain moisture field. The MAE difference for wind fields (Fig. 21) indicates that on average the TAMDAR assimilation has a slightly negative influence on the 1-km domain winds.

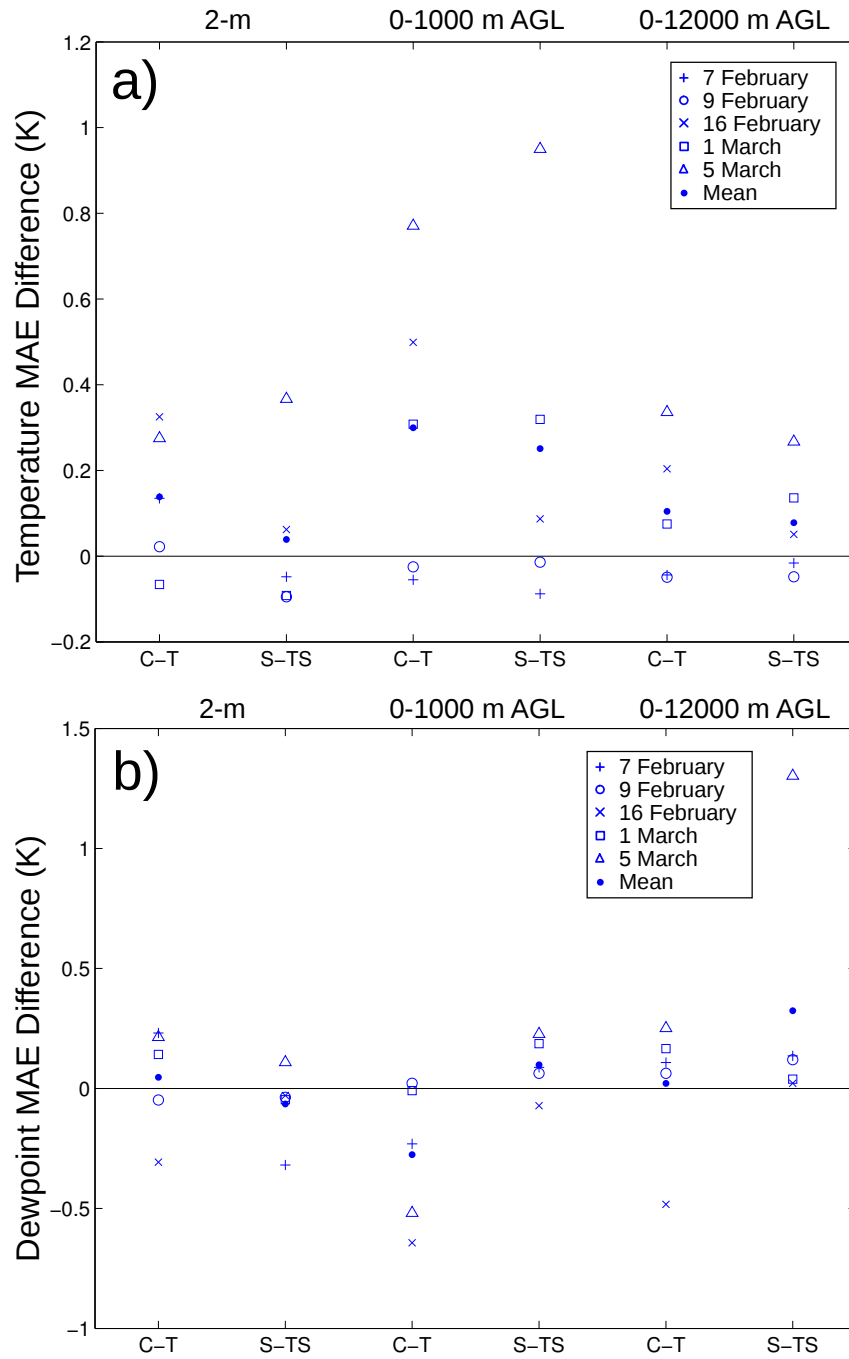


Fig. 20 Difference in MAE between Exp. C and Exp. T (columns labeled C-T) and between Exp. S and Exp. TS (columns labeled S-TS) for 19–00 UTC for 2 m, 0–1,000-m AGL, and 0–12,000-m AGL on the 1-km domain for a) temperature and b) dewpoint. Positive values indicate Exp. T performs better than Exp. C and that Exp. TS performs better than Exp. S, respectively. A point is plotted for each case day as well as the mean of all of the case days, as noted in the figure legend.

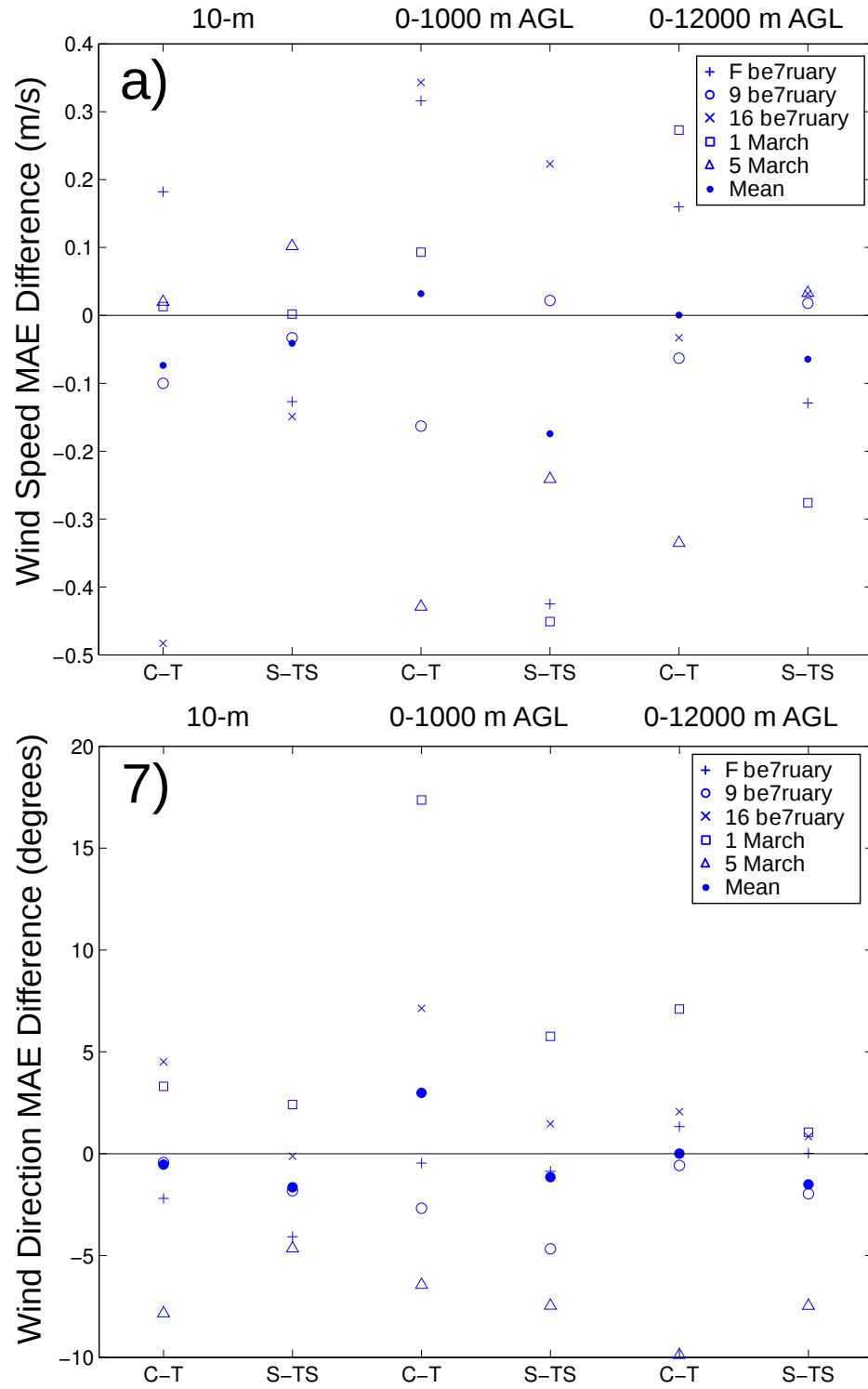


Fig. 21 Difference in MAE between Exp. C and Exp. T (columns labeled C-T) and between Exp. S and Exp. TS (columns labeled S-TS) for 19-00 UTC for 10 m, 0-1,000-m AGL, and 0-12,000-m AGL on the 1-km domain for a) wind speed and b) wind direction. Positive values indicate Exp. T performs better than Exp. C and that Exp. TS performs better than Exp. S, respectively. A point is plotted for each case day as well as the mean of all of the case days, as noted in the figure legend.



The latter portion of the model forecast (01–12 UTC; 7–18-h forecast) shown in Fig. 22 has significant variability among the case days. Averaged over the case days, the temperature MAE difference (Fig. 22a) indicates very small changes due to TAMDAR data ( $<0.1$  K). For dewpoint (Fig. 22b), adding TAMDAR observations (C-T) is a degradation when compared to not using any observations, whereas adding TAMDAR observations to standard observations (S-TS) has very little mean effect. Averaged over the case days, wind speed (Fig. 22c) for this period is improved by the addition of TAMDAR data especially compared to the use of no observations. While the individual case days' wind direction is impacted by the TAMDAR data, the mean effect averaged over the case days is nearly zero (Fig. 22d).

Overall, on the 1-km domain during the first 6 h of the model forecast, the use of TAMDAR observations improves the temperature forecast, has mixed effects on the dewpoint forecast, and degrades the winds slightly. During that latter portion of the forecast (01–12 UTC) the effects are mixed, with an improvement seen in wind speed.

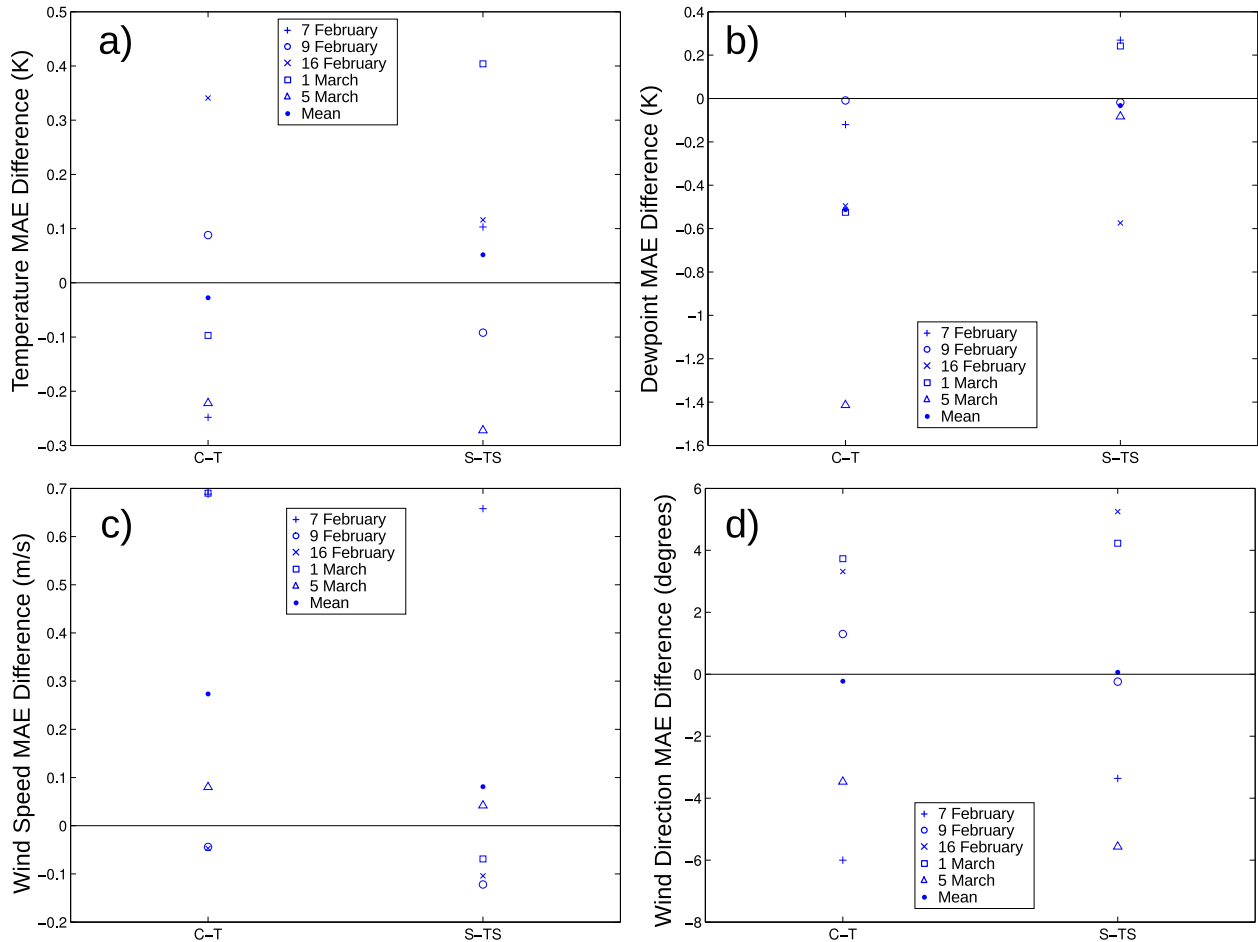


Fig. 22 Difference in MAE between Exp. C and Exp. T (columns labeled C-T) and between Exp. S and Exp. TS (columns labeled S-TS) for 01–12 UTC for 0–1,000-m AGL on the 1-km domain for a) temperature, b) dewpoint, c) wind speed, and d) wind direction. Positive values indicate Exp. T performs better than Exp. C and that Exp. TS performs better than Exp. S, respectively. A point is plotted for each case day as well as the mean of all of the case days, as noted in the figure legend.

### 6.2.2 Value of Local Rawinsonde

To investigate a local rawinsonde's value to the model forecast, we examine Exp. S, SK, TS, and TSK; also, we investigate whether TAMDAR data's value can equal a local rawinsonde's by examining Exp. S and TSK. Exp. S utilizes standard data (standard surface observations, ship reports, and rawinsonde) to both enhance the initial condition analysis from GFS as well as to assimilate into the model during a preforecast period. Exp. SK removes the KNKX/Miramar rawinsonde (Fig. 4) from the observations and is used to determine the value of the rawinsonde by comparing Exp. SK with Exp. S. Exp. TS and TSK are similar to Exp. S and SK but also include TAMDAR data; comparison between Exp. TS and TSK indicates the value of the rawinsonde if TAMDAR data is present. By comparing Exp. TSK to Exp. S, one can determine whether using TAMDAR data compensates for the lack of a local rawinsonde.

The evaluation for this section will concentrate on the 1-km domain. This is because the rawinsonde is within this domain and because we are interested in the value of the *local* rawinsonde and limiting our evaluation to the 1-km domain ensures that the rawinsonde remains more local than if we evaluated the larger 3-km domain.

The KNKX rawinsonde removed for some experiments (Exps. SK and TSK) occurs at 12 UTC, at the beginning of the model integration, whereas the forecast begins at 18 UTC, and the verification at 19 UTC. Since the effects of assimilating an observation tend to fade with time, the benefits of the rawinsonde are likely to be less pronounced at that time than if they were evaluated closer to the time of the rawinsonde. However, since rawinsondes are often only available every 12 h, one will often not have any very recent rawinsondes available to assimilate, so the experimental configuration here is not inconsistent with real-world conditions.

Figures 23 and 24 show the improvements on the 1-km domain during the first 6 h of the forecast (19–00 UTC) due to the inclusion of the local rawinsonde (Miramar, CA) in the initial conditions and data assimilation. The forecast's surface-temperature, case-day mean MAE decreases with the use of the local rawinsonde (seen in Fig. 23a in the leftmost column, labeled 2-m SK-S, where the mean value is positive indicating that Exp. SK has larger temperature MAE than Exp. S), but only slightly and there is large case-day to case-day variability. The addition of the local rawinsonde to the experiment that included TAMDAR data in addition to the typical data of standard surface observations and rawinsondes (columns labeled TSK-TS) actually slightly degrades the case-day mean surface-temperature MAE. For the 0–1,000-m AGL layer, the addition of the local rawinsonde slightly improves the case-day mean MAE both with and without TAMDAR data. For the entire 0–12,000-m AGL layer, the case-day mean temperature MAE is nearly zero. The dewpoint forecast (Fig. 23b) is on average degraded through the addition of the local rawinsonde (by between  $\approx 0.1$  K and  $\approx 0.5$  K depending on the vertical level and whether TAMDAR data are utilized). The local rawinsonde generally improved the case-day mean wind-speed and wind-direction MAE, especially in the 0–1,000-m AGL layer (Fig. 24).

Overall, the rawinsonde appears to have the greatest benefit in 0–1,000-m temperature and winds, and actually appears to degrade model forecast dewpoint.

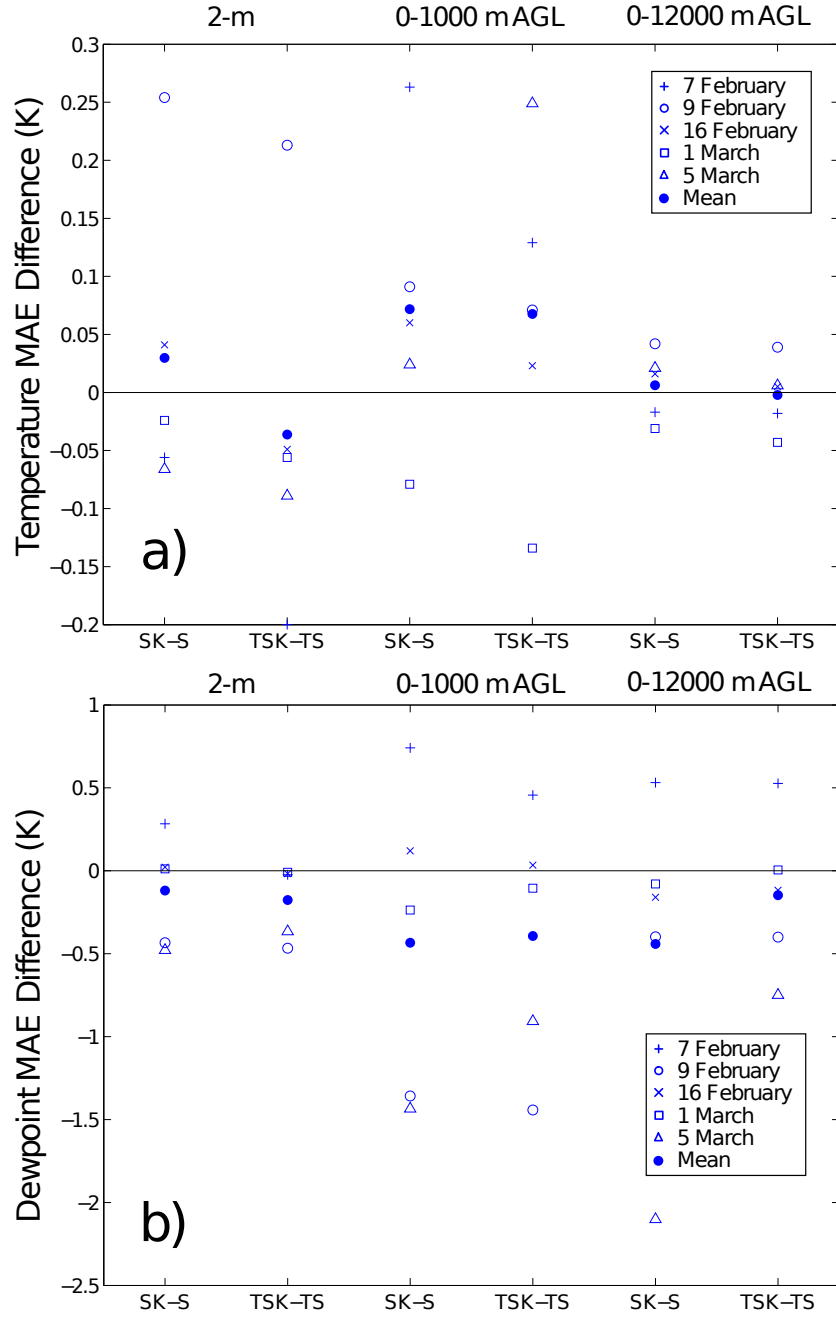


Fig. 23 Difference in MAE between Exp. SK and Exp. S (columns labeled SK-S) and between Exp. TSK and Exp. TS (columns labeled TSK-TS) for 19–00 UTC for 2 m, 0–1,000-m AGL, and 0–12,000-m AGL on the 1-km domain for a) temperature and b) dewpoint. Positive values indicate Exp. S performs better than Exp. SK and that Exp. TS performs better than Exp. TSK, respectively. A point is plotted for each case day as well as the mean of all of the case days, as noted in the figure legend.

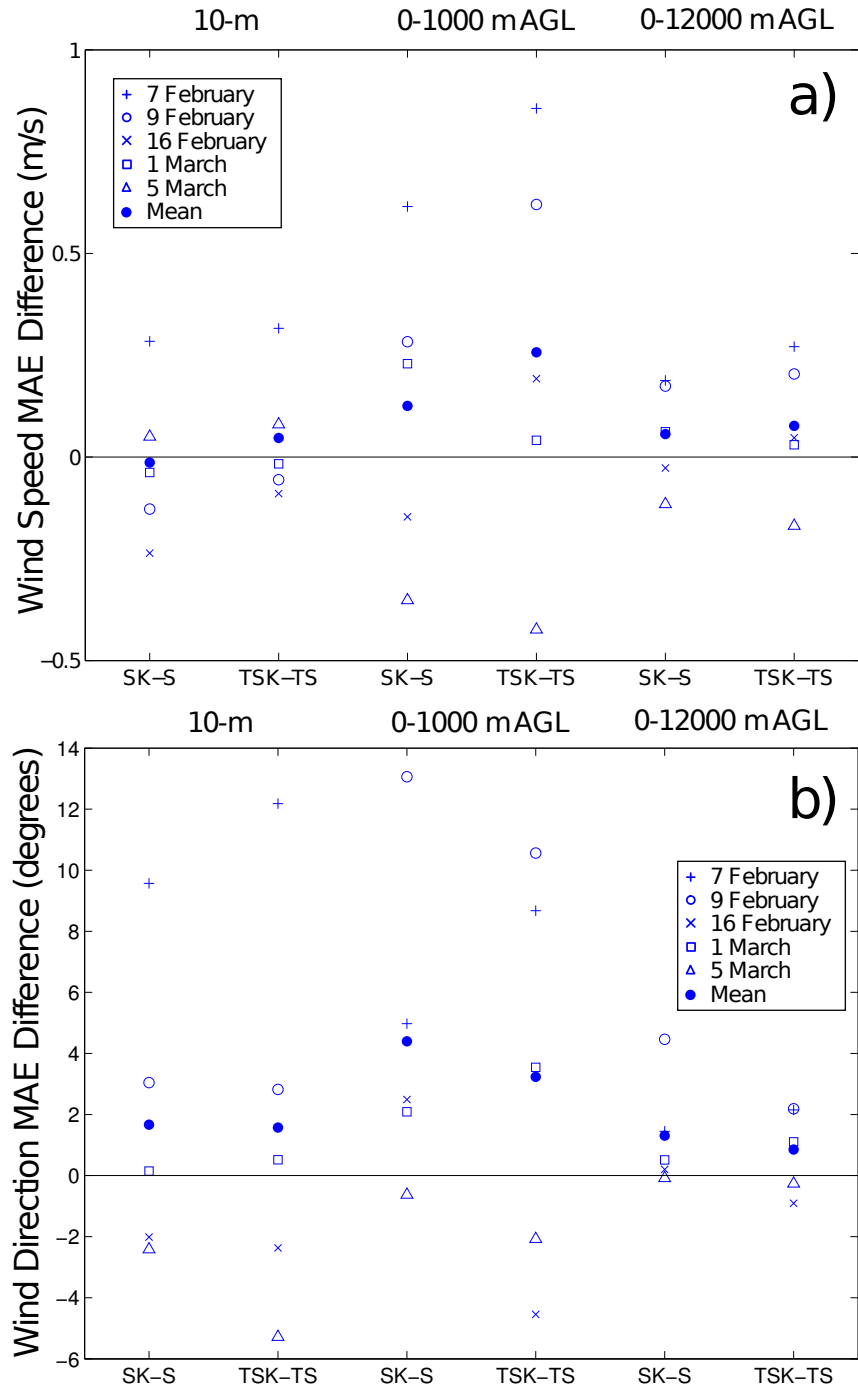


Fig. 24 Difference in MAE between Exp. SK and Exp. S (columns labeled SK-S) and between Exp. TSK and Exp. TS (columns labeled TSK-TS) for 19–00 UTC for 10 m, 0–1,000-m AGL, and 0–12,000-m AGL on the 1-km domain for a) wind speed and b) wind direction. Positive values indicate Exp. S performs better than Exp. SK and that Exp. TS performs better than Exp. TSK, respectively. A point is plotted for each case day as well as the mean of all of the case days, as noted in the figure legend.

Looking further into the forecast (01–12 UTC; 7–18-h forecast), the local rawinsonde slightly degrades surface temperature but slightly improves the temperature forecast above the surface (Fig. 25a). The case-day mean effect on the dewpoint is very small, except in the lowest 1,000 m where the local rawinsonde improves the dewpoint forecast by about 0.3K for the experiment without TAMDAR and by about 0.6K for the experiment with TAMDAR (Fig. 25b). For wind (Fig. 26), the local rawinsonde on average degrades wind speed very slightly but has a mixed impact on the wind direction. In the 7–18-h forecast the greatest benefit from the local rawinsonde appears to be in temperature and moisture in the lowest 1,000 m.

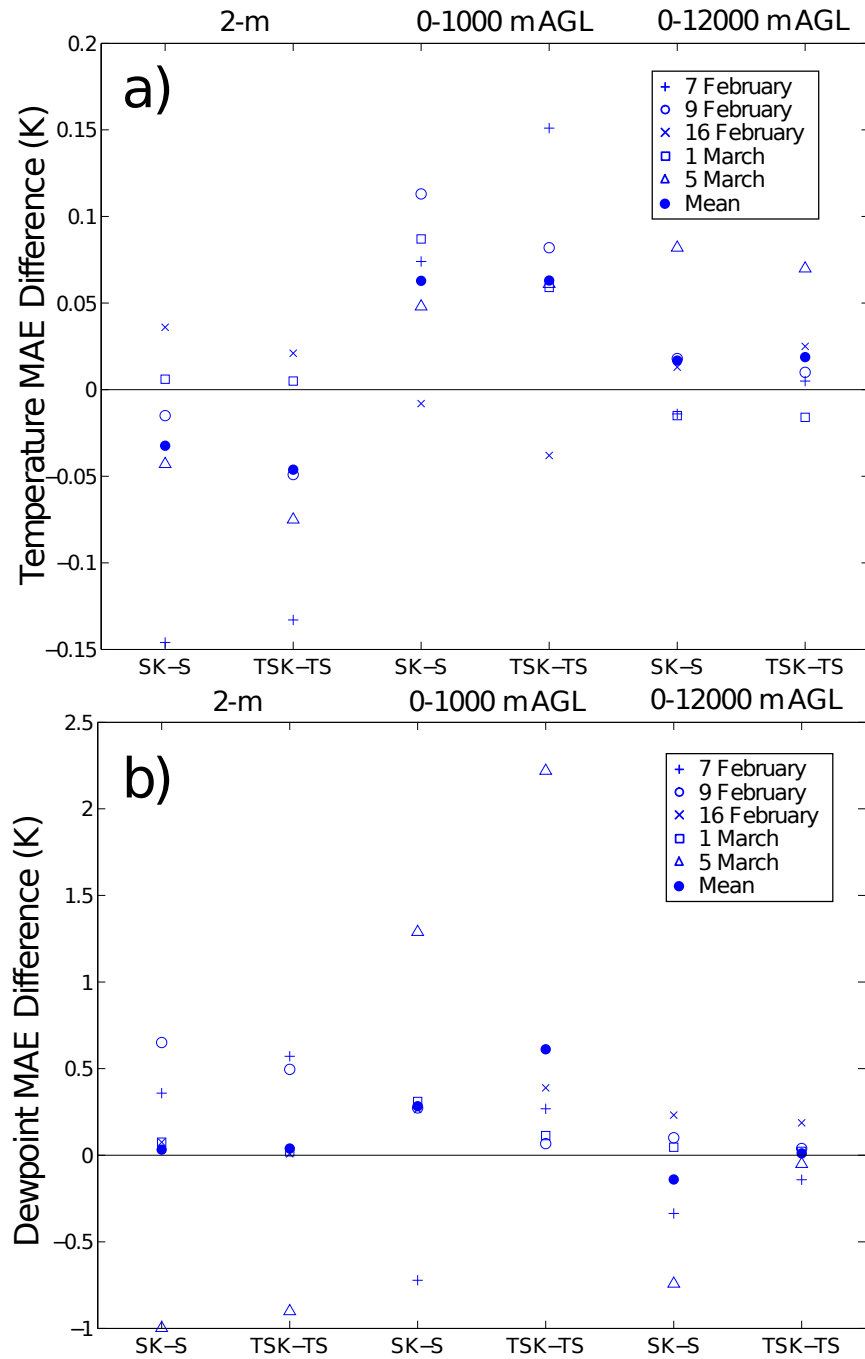


Fig. 25 Difference in MAE between Exp. SK and Exp. S (columns labeled SK-S) and between Exp. TSK and Exp. TS (columns labeled TSK-TS) for 01–12 UTC for 2 m, 0–1,000-m AGL, and 0–12,000-m AGL on the 1-km domain for a) temperature and b) dewpoint. Positive values indicate Exp. S performs better than Exp. SK and that Exp. TS performs better than Exp. TSK, respectively. A point is plotted for each case day as well as the mean of all of the case days, as noted in the figure legend.

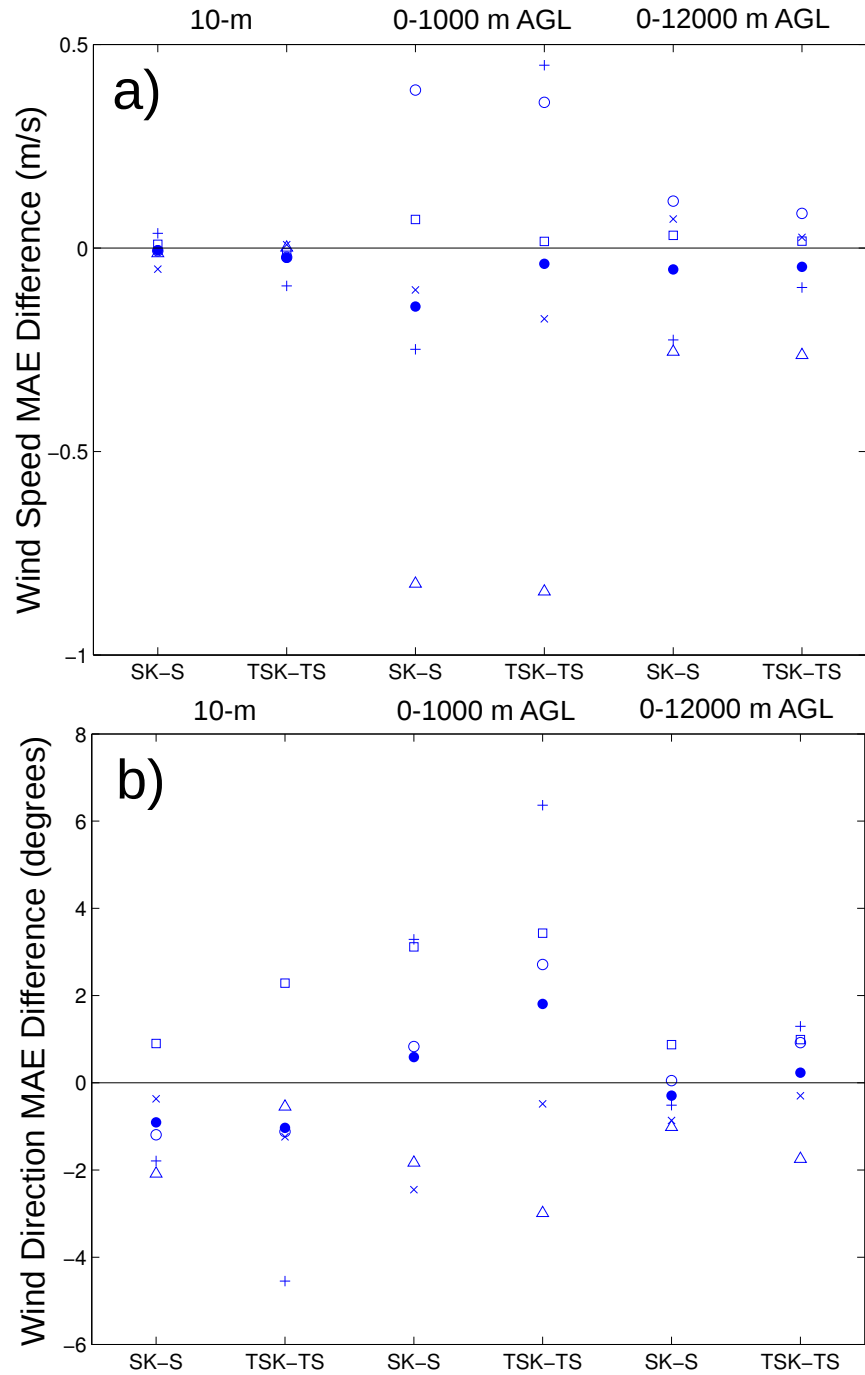


Fig. 26 Difference in MAE between Exp. SK and Exp. S (columns labeled SK-S) and between Exp. TSK and Exp. TS (columns labeled TSK-TS) for 01–12 UTC for 10 m, 0–1,000-m AGL, and 0–12,000-m AGL on the 1-km domain for a) wind speed and b) wind direction. Positive values indicate Exp. S performs better than Exp. SK and that Exp. TS performs better than Exp. TSK, respectively. A point is plotted for each case day as well as the mean of all of the case days, as noted in the figure legend.

The vertical profile of MAE is examined in order to determine whether there are any consistent signals in the vertical-error structure among the 5 case days. The 1-km domain vertical profile of temperature for the first 6 h of the forecast (19–00 UTC; 1–6-h forecast) is shown in Fig. 27 for Exp. S, which utilizes standard observations, and Exp. SK, which is the same as Exp. S but omits the local rawinsonde. If the use of the local rawinsonde improves the forecast, then the MAE for Exp. S will be smaller than the MAE for Exp. SK. For these cases, there does not appear to be a consistent day-to-day signal in the vertical distribution of the effects of using the local rawinsonde. It can be seen that the magnitude of the effect of the local rawinsonde on the MAE varies notably by case and within a specific case day by height. Note that the number of observations available for verification decreases with height (Fig. 27f). The limited number of observations at some heights (e.g., on 9 February there are 8 observations in the 7,000–8,000-m layer for this time period) calls into questions the statistical significance of the statistics at the upper levels. For dewpoint (Fig. 28) there also does not seem to be a consistent pattern across the case days in regard to the impact of the local rawinsonde. For example, while on 7 February the local rawinsonde lowers the dewpoint MAE in the 0–3,000-m AGL layer, on 5 March there is a significant degradation from the local rawinsonde in this layer. Note that the number of dewpoint observations available for verification (Fig. 28f) is notably less than for temperature (Fig. 27f); a very limited number of dewpoint observations is available for verification above 6,000-m AGL (Fig. 28f). For wind speed, there are again no clear patterns apparent in the vertical MAE profile; however, note that 7 February (Fig. 29a) does demonstrate that sometimes the local rawinsonde can result in notable improvements, such as the 4,000–5,000-m AGL level here where wind-speed MAE is decreased from 5.8 to 4.5 m/s. For wind direction (Fig. 30), the rawinsonde results in at least a small improvement in MAE in the lowest 1,000 m, except for one case day when the MAE changes less than 1°. Overall, it is difficult to ascertain clear patterns in the vertical MAE from day to day except for the near-surface improvement in wind direction.



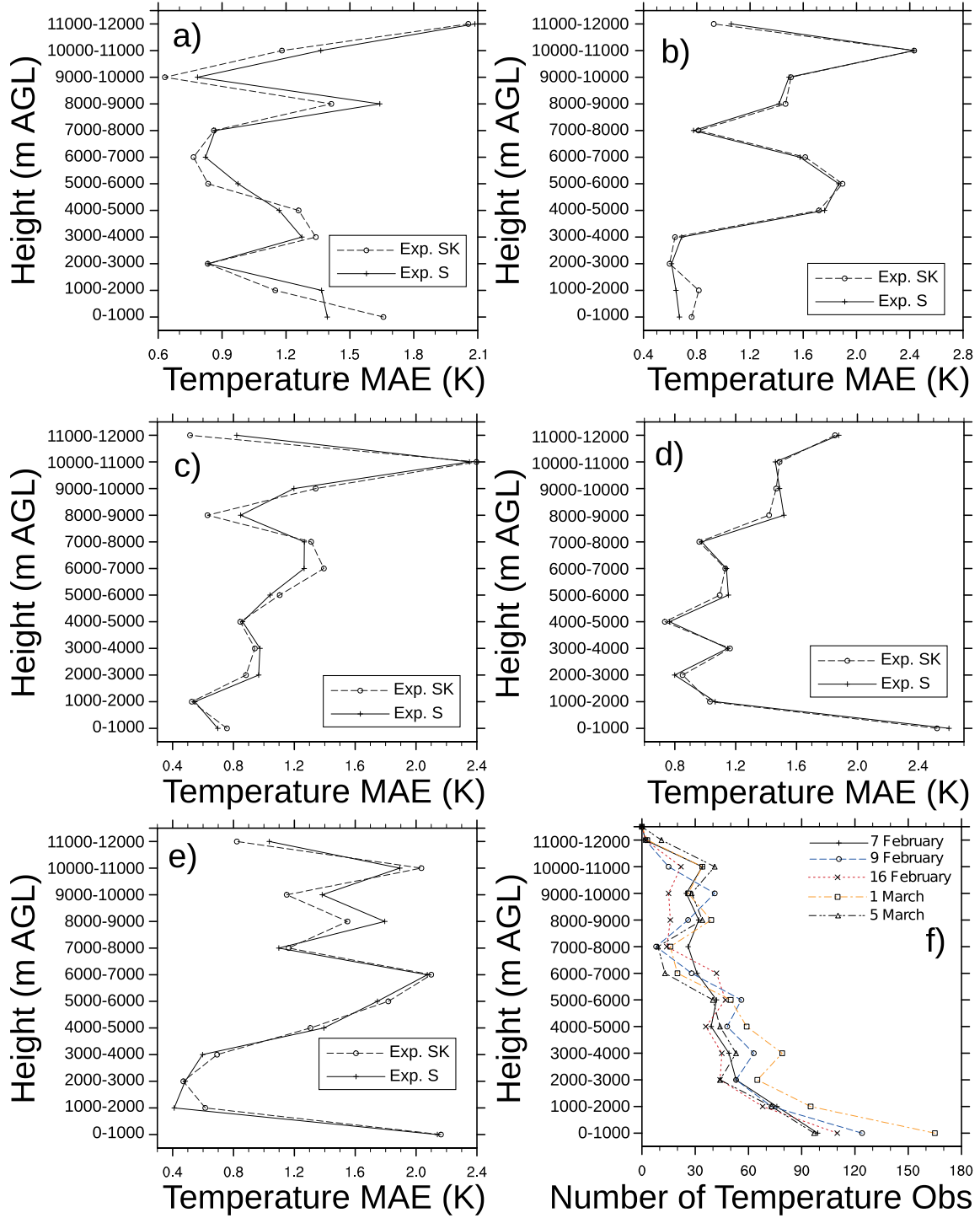


Fig. 27 Vertical profiles of temperature MAE (excluding surface observations) for 19–00 UTC for Exp. SK and Exp. S for a) 7 February, b) 9 February, c) 16 February, d) 1 March, and e) 5 March. Panel f is a vertical profile of the number of observations used to construct the MAE in panels a–e.

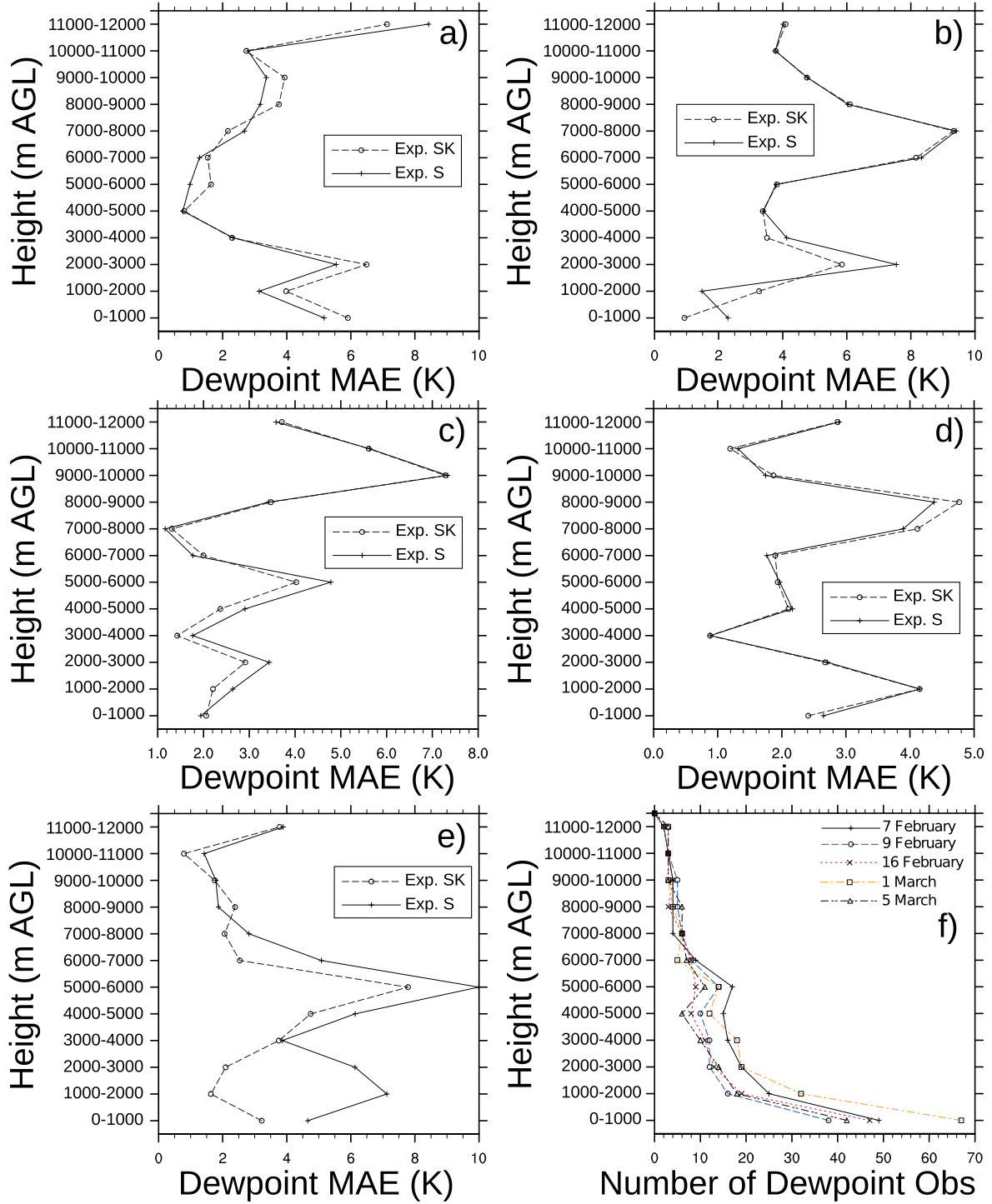


Fig. 28 Vertical profiles of dewpoint MAE (excluding surface observations) for 19–00 UTC for Exp. SK and Exp. S for a) 7 February, b) 9 February, c) 16 February, d) 1 March, and e) 5 March. Panel f is a vertical profile of the number of observations used to construct the MAE in panels a–e.

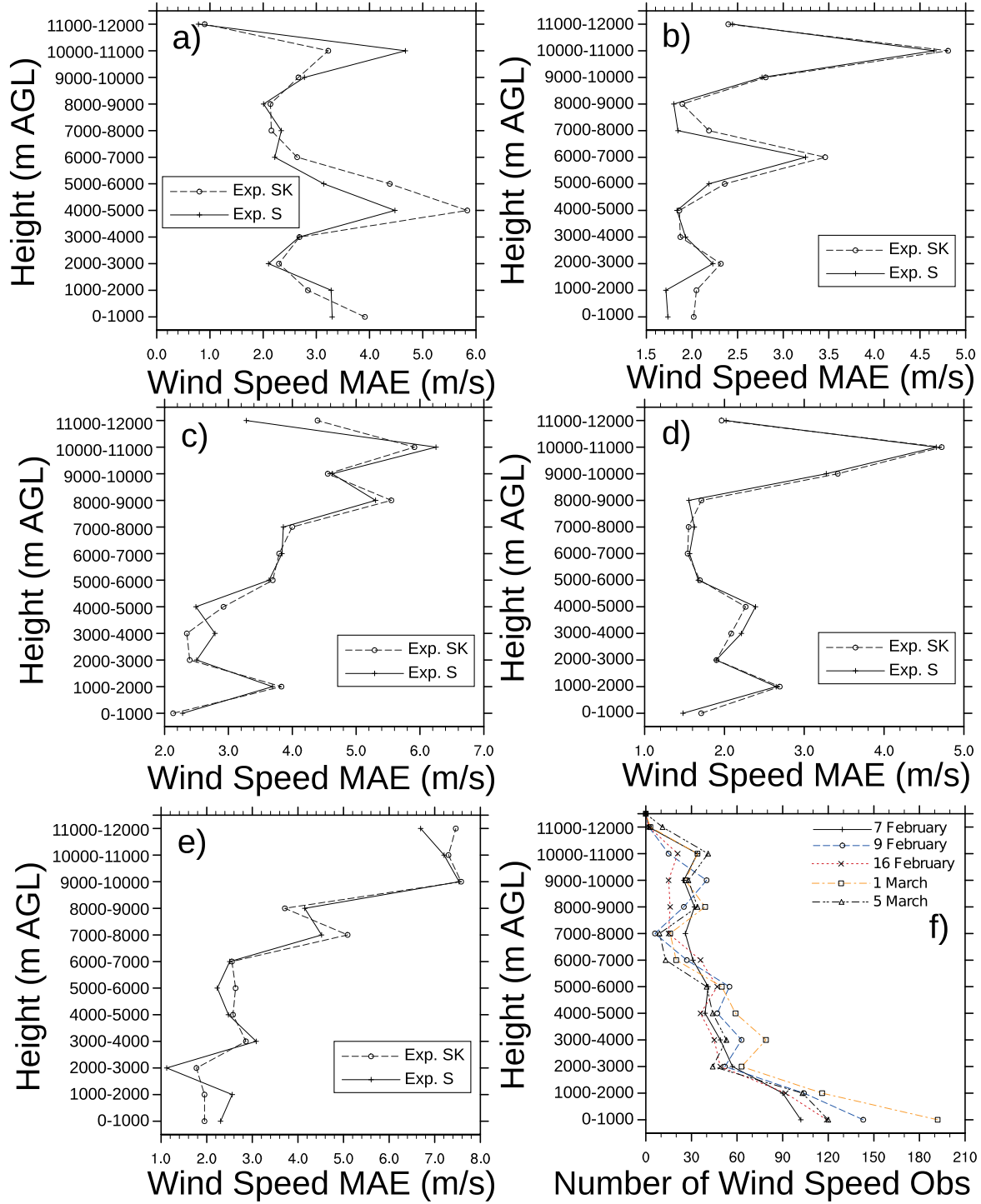


Fig. 29 Vertical profiles of wind-speed MAE (excluding surface observations) for 19–00 UTC for Exp. SK and Exp. S for a) 7 February, b) 9 February, c) 16 February, d) 1 March, and e) 5 March. Panel f is a vertical profile of the number of observations used to construct the MAE in panels a–e.

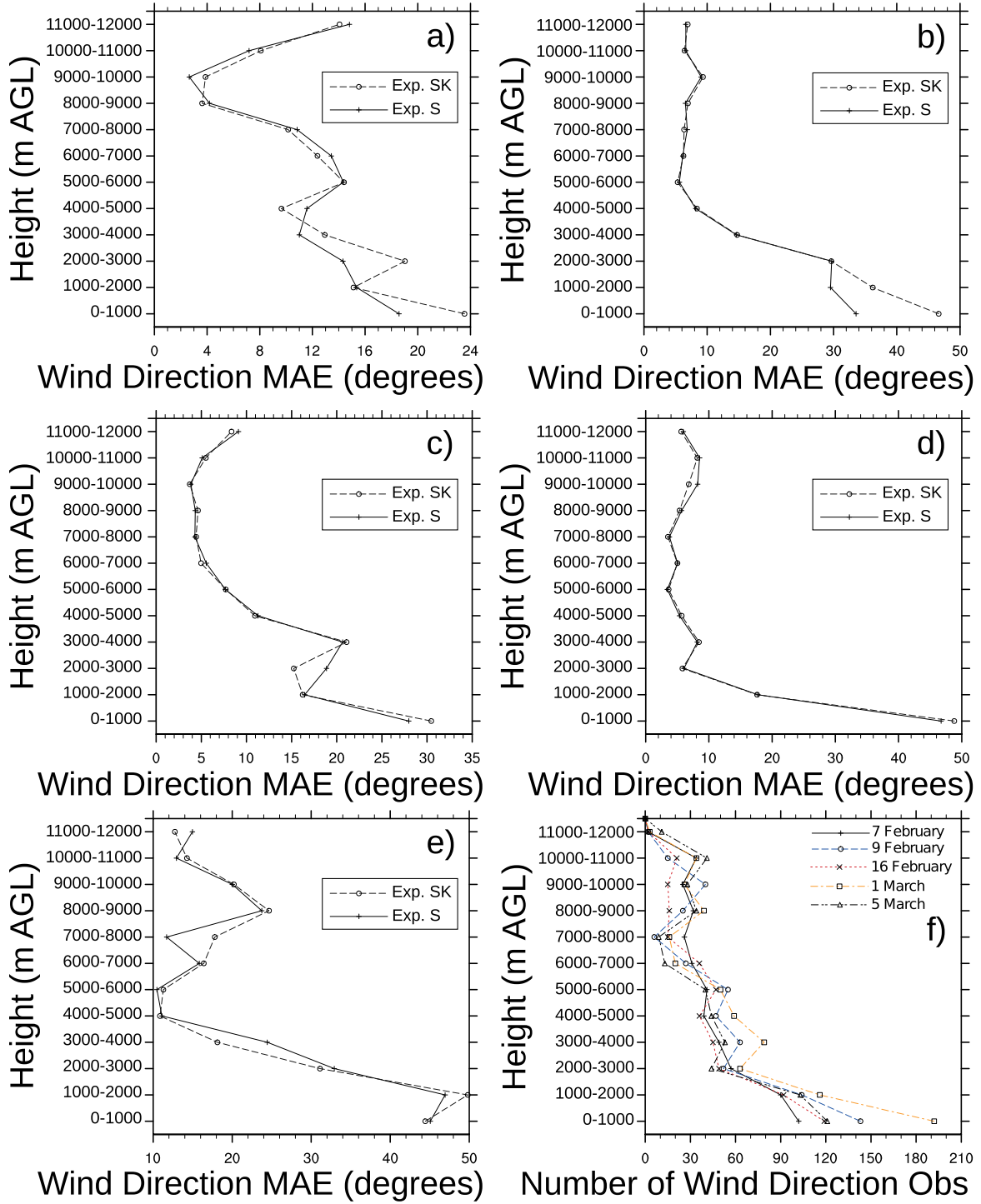


Fig. 30 Vertical profiles of wind-direction MAE (excluding surface observations) for 19–00 UTC for Exp. SK and Exp. S for a) 7 February, b) 9 February, c) 16 February, d) 1 March, and e) 5 March. Panel f is a vertical profile of the number of observations used to construct the MAE in panels a–e.

To investigate whether TAMDAR observations could serve as a replacement for the local rawinsonde, we compare Exp. S, which assimilates standard surface data and rawinsondes, with Exp. TSK, which assimilates standard surface data, rawinsondes besides the local rawinsonde, and TAMDAR data. If the MAE of Exp. TSK is lower than the MAE of Exp. S, this indicates that use of the TAMDAR data was able to make up any accuracy lost with the loss of the rawinsonde data. Figure 31 shows this comparison for the first 6 h of the forecast (19–00 UTC). For temperature (Fig. 31a) and dewpoint (Fig. 31b) the case-day mean MAE difference is positive at the surface, in the 0–1,000-m AGL layer, and in the 0–12,000-m AGL layer. However, for wind speed (Fig. 31c) and wind direction (Fig. 31d) the case-day mean MAE difference is negative. This suggests that for the short-term forecast (0–6 h), TAMDAR data are sufficient to compensate for the lack of a local rawinsonde for temperature and dewpoint, but not so for wind. For the longer forecast (7–18 h), the case-day mean MAE difference for temperature is very small (Fig. 32a), while for dewpoint TAMDAR is unable to compensate for the loss of a local rawinsonde in the lower atmosphere (0–1,000-m AGL; Fig. 32b). During this time period the inclusion of TAMDAR data result in a slightly better wind-speed and slightly worse wind-direction forecast above the surface than the inclusion of the local rawinsonde (Fig. 32c and 32d). Overall, the TAMDAR data appear sufficient to compensate for the loss of a local rawinsonde for short-term (1–6 h) temperature and dewpoint forecasts, but not for wind forecasts. For the longer term (7–18 h), the interpretation is less clear.

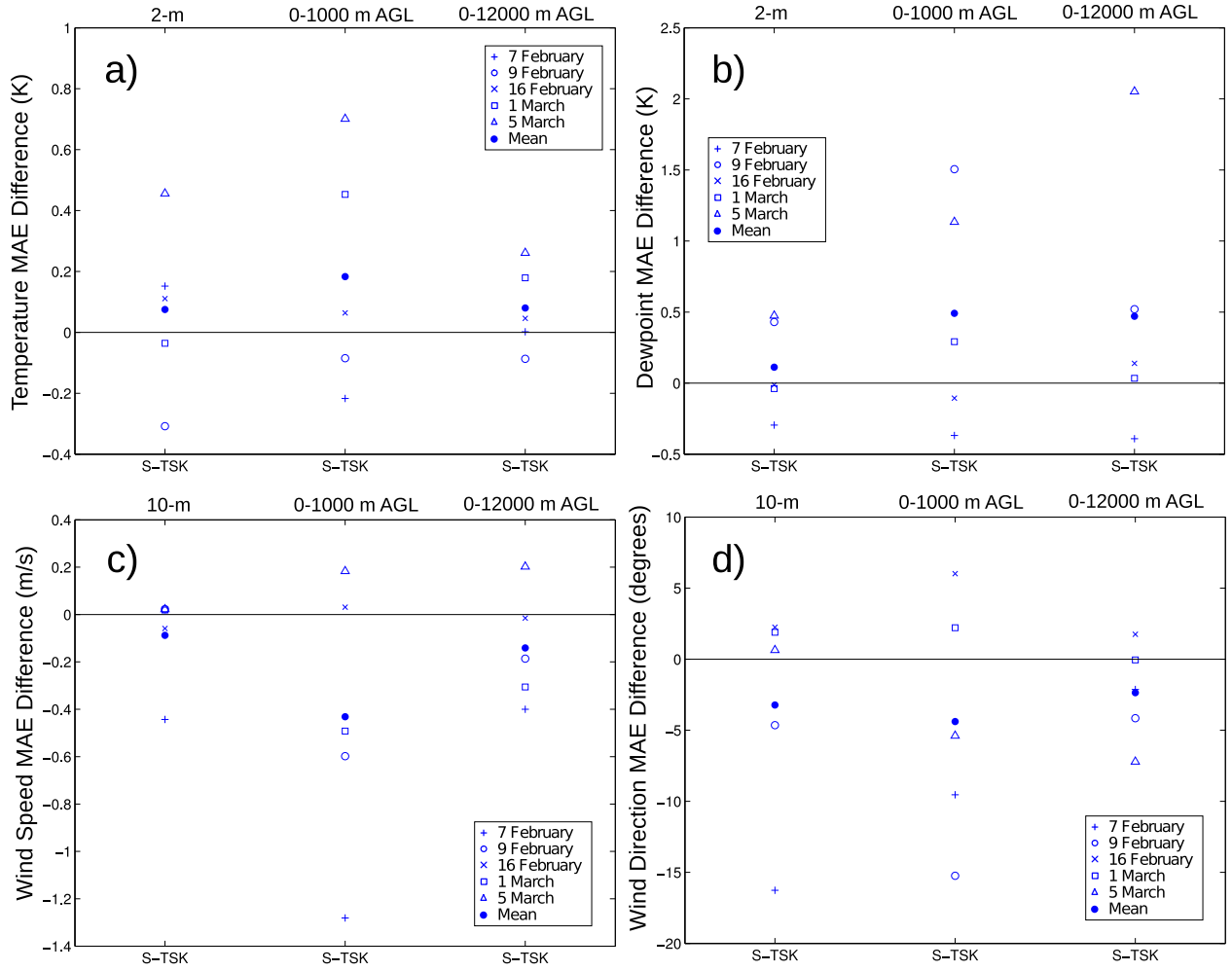


Fig. 31 Differences in MAE between Exp. S and Exp. TSK for 19–00 UTC for surface, 0–1,000-m AGL, and 0–12,000-m AGL on the 1-km domain for a) temperature, b) dewpoint, c) wind speed, and d) wind direction. Positive values indicate Exp. TSK performs better than Exp. S. A point is plotted for each case day as well as the mean of all of the case days, as noted in the figure legend.

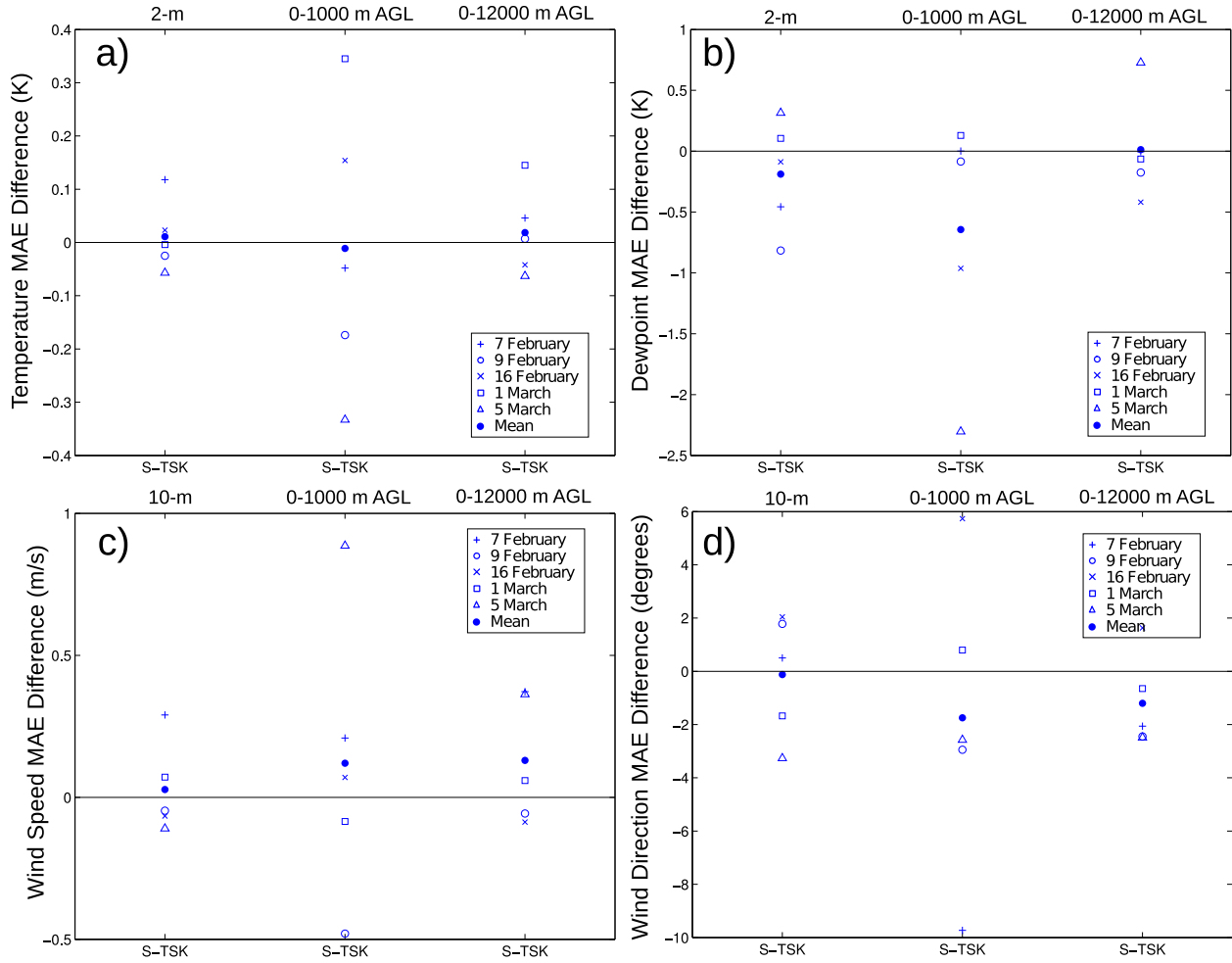


Fig. 32 Differences in MAE between Exp. S and Exp. TSK for 01–12 UTC for surface, 0–1,000-m AGL, and 0–12,000-m AGL on the 1-km domain for a) temperature, b) dewpoint, c) wind speed, and d) wind direction. Positive values indicate Exp. TSK performs better than Exp. S. A point is plotted for each case day as well as the mean of all of the case days, as noted in the figure legend.

We investigated the effects of removing the local rawinsonde from the observations that are used to create the analysis used as initial conditions and from the observations used for observation nudging. The local rawinsonde in general improves the 1–6-h forecast of temperature and wind in the lowest 1,000 m, but degrades the forecast for dewpoint in this layer. For the longer-term forecast in the 0–1,000-m layer (7–18 h), temperature and dewpoint MAE are generally improved while wind-speed MAE is slightly degraded and wind direction almost unchanged. A similar comparison was completed using experiments that additionally used TAMDAR data. We also investigated the potential to use TAMDAR data in place of a local rawinsonde and found that for these cases TAMDAR is an effective replacement in terms of the accuracy of short-term temperature and dewpoint forecasts.

### 6.2.3 Value of Denser Surface Observations

To determine the value added by increasing the density of surface observations, we compare Exp. S, using standard surface observations and rawinsondes, with Exp. SM that additionally includes mesonet surface observations from the MADIS data set. The extent of the standard surface observations and the mesonet surface observations for all 3 WRF domains are shown in Fig. 5. The significantly enhanced spatial coverage provided by inclusion of the mesonet observations is clearly visible. (Figure 6 provides the same details but only for the 1-km domain.)

Figure 33 shows the difference between Exp. S and Exp. SM in MAE for the first 6 h of the forecast (19–00 UTC). For temperature, dewpoint, wind speed, and wind direction at the surface there is at least a slight improvement through the use of the mesonet observations when averaged over the case days. For temperature the MAE improves very slightly above the surface with the use of the mesonet observations; for dewpoint, wind speed, and wind direction above the surface, however, the case-day mean MAE difference indicates either a degradation or very little impact from the use of the mesonet observations. The improvement at the surface accompanied by degradation above the surface for temperature, dewpoint, and wind speed suggest that the vertical spreading of the influence of the surface observation may not be optimal.



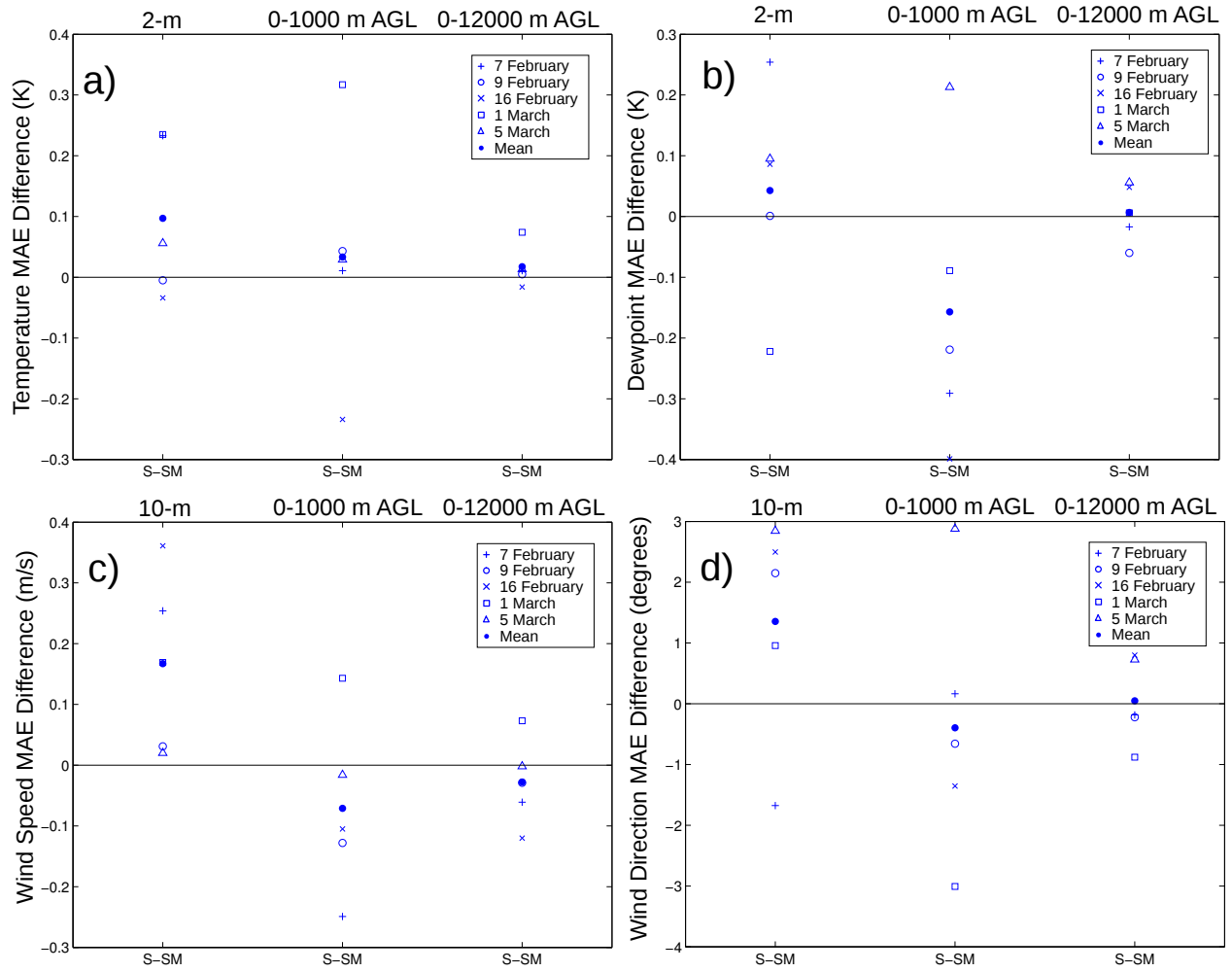


Fig. 33 Differences in MAE between Exp. S and Exp. SM for 19–00 UTC for surface, 0–1,000-m AGL, and 0–12,000-m AGL on the 1-km domain for a) temperature, b) dewpoint, c) wind speed, and d) wind direction. Positive values indicate Exp. SM performs better than Exp. S. A point is plotted for each case day as well as the mean of all of the case days, as noted in the figure legend.

For the longer-term forecast (01–12 UTC) the case-day mean effects of the mesonet data are generally fairly small (Fig. 34). Generally the case-day mean effects of the mesonet are at least slightly positive, although the 2-m temperature and 0–1,000-m dewpoint are degraded slightly by the introduction of mesonet data.

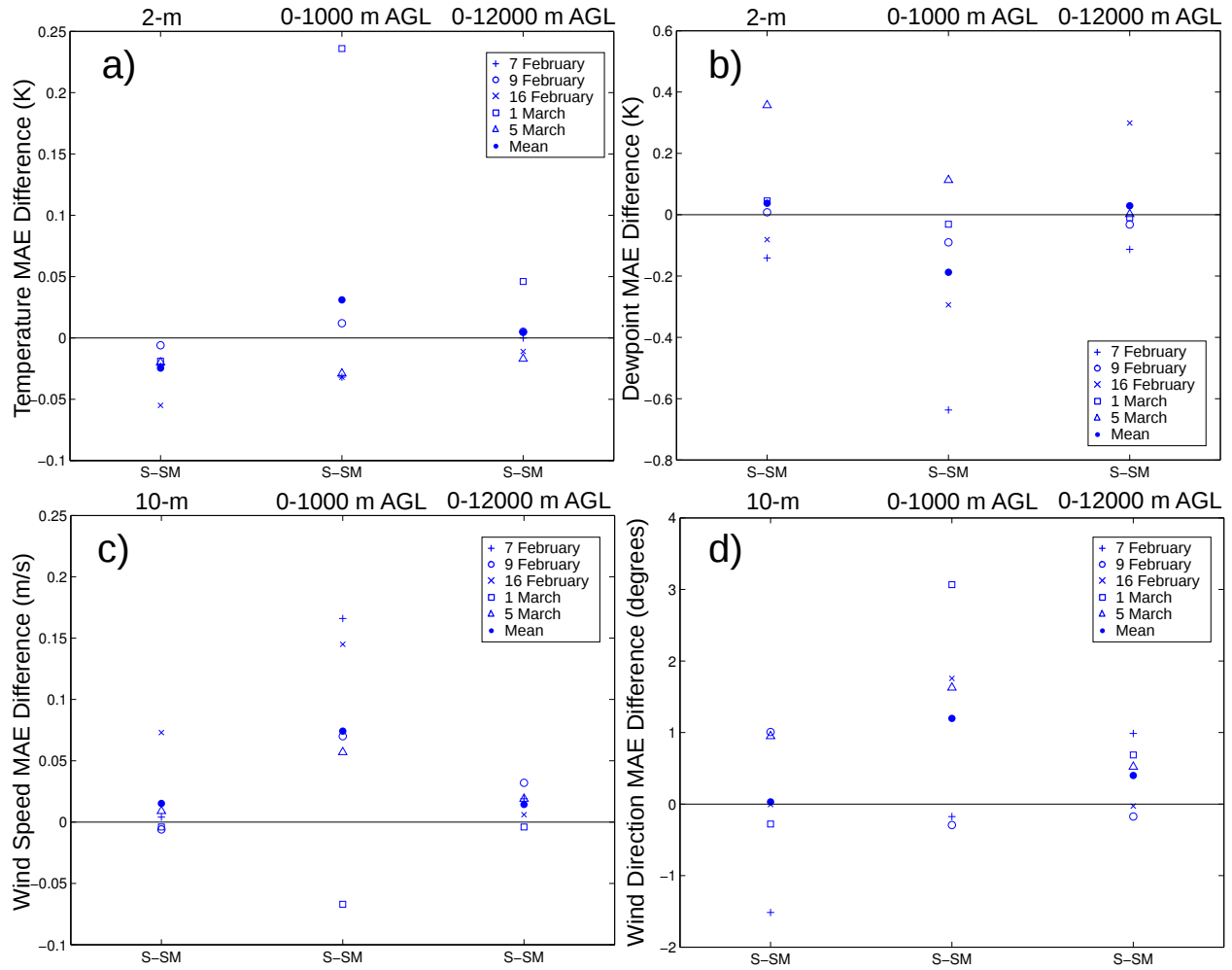


Fig. 34 Differences in MAE between Exp. S and Exp. SM for 01–12 UTC for surface, 0–1,000-m AGL, and 0–12,000-m AGL on the 1-km domain for a) temperature, b) dewpoint, c) wind speed, and d) wind direction. Positive values indicate Exp. SM performs better than Exp. S. A point is plotted for each case day as well as the mean of all of the case days, as noted in the figure legend.

Since the largest impacts of utilizing surface observations are expected to be at the surface, and because observations at the surface are often available hourly (compared to above-surface observations, which may be every 12 h), we examine the time series of model error at the surface. Specifically, in Fig. 35 we look at the difference between the time series of MAE of Exp. S to that of Exp. SM, where a positive value indicates that Exp. SM has a lower MAE than Exp. S and thus that mesonet data benefit the model solution. For temperature (Fig. 35a), on most case days the inclusion of mesonet data results in an improvement at the very beginning of the simulation (12 UTC); this is due to the addition of the mesonet data to the initial condition analysis completed by Obsgrid. The experiments using the mesonet data have a lower MAE through the period in which new observations are assimilated (12–18 UTC). Recall in Section 6.1 that observations up to 18 UTC are included in the assimilation, and the model may be nudged toward those observations up until 19 UTC as the data assimilation ramps down during

this period. The benefit of using mesonet data on the model temperature solution notably decreases by 19 UTC for 7 and 16 February, the 2 case days when model temperatures improved most due to use of the mesonet data. For 9 February and 5 March, the benefit of mesonet data is decreasing by 17 UTC, and for 9 February this trend continues so that by 19 UTC there is basically no benefit from using the mesonet observations. For 1 and 5 March the reduction in MAE from the use of mesonet observations increases between 18 and 19 UTC as the nudging ramps down; while 5 March continues its trend of showing less benefit from mesonet observations as the simulation advances, 1 March indicates the benefit stays relatively constant for a few hours after the end of the data assimilation. The case-day mean temperature MAE difference's time series is shown in Fig. 36. For temperature, Fig. 36a indicates a benefit in the initial conditions that increases until the end of the data assimilation and then decreases to about zero by  $\approx 22$  UTC.

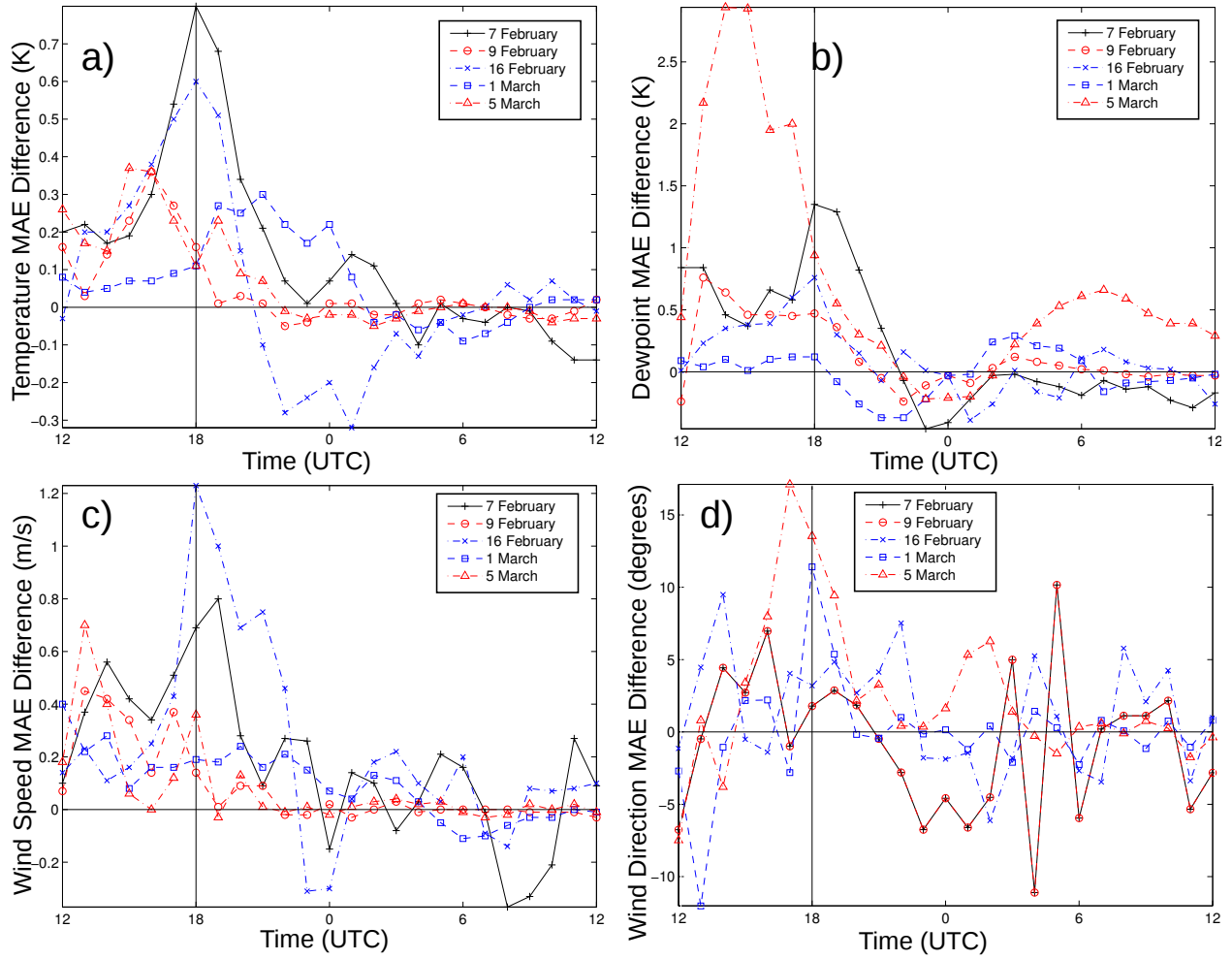


Fig. 35 Time series of the differences in MAE between Exp. S and Exp. SM on the 1-km domain for a) 2-m temperature, b) 2-m dewpoint, c) 10-m wind speed, and d) 10-m wind direction. Positive values indicate Exp. SM performs better than Exp. S. A time series is plotted for each case day, as noted in the legend. The vertical line at 18 UTC indicates the end of the preforecast period and the beginning of the forecast period during which no current observations are assimilated.

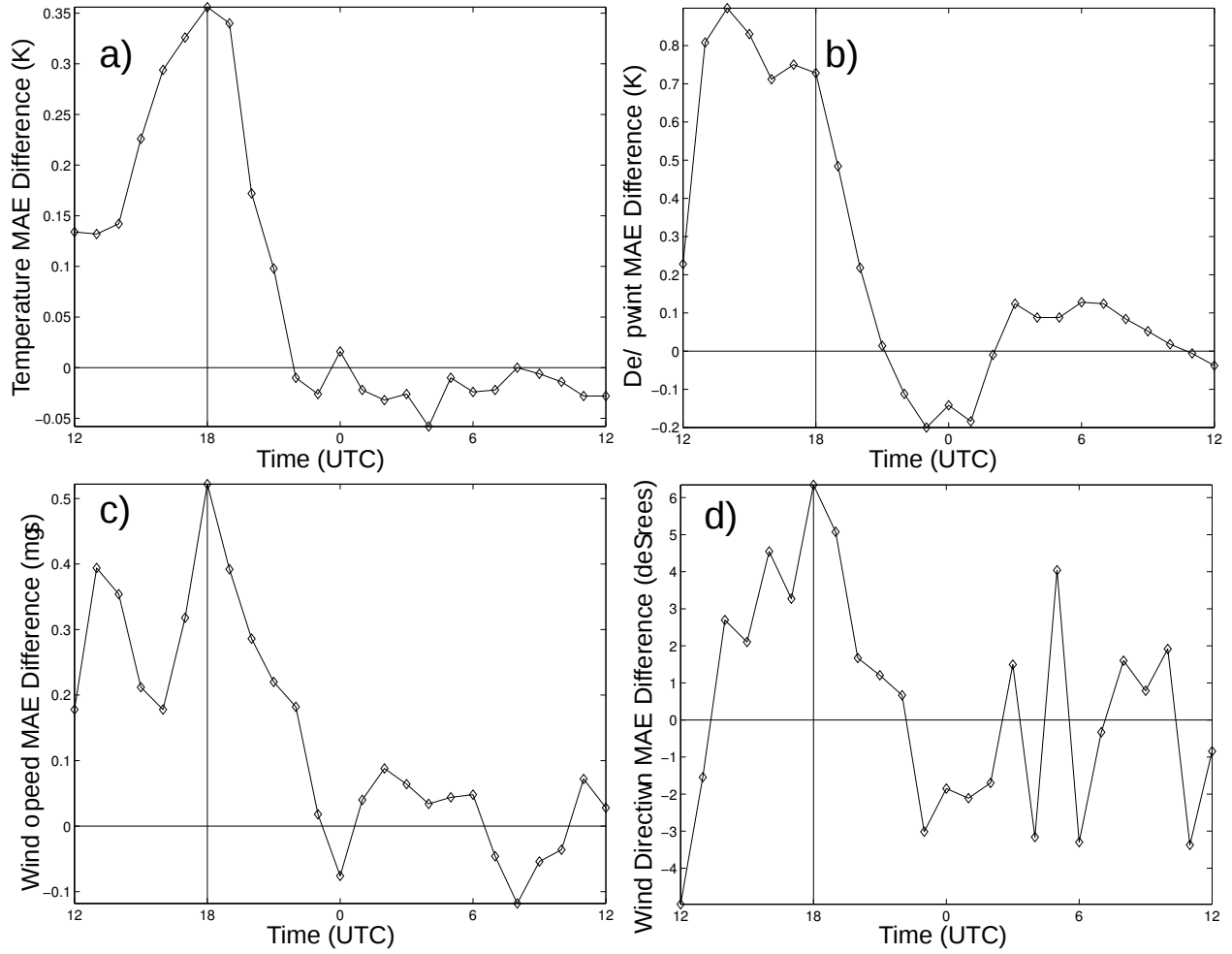


Fig. 36 Time series of the differences in MAE between Exp. S and Exp. SM averaged over the 5 case days on the 1-km domain for a) 2-m temperature, b) 2-m dewpoint, c) 10-m wind speed, and d) 10-m wind direction. Positive values indicate Exp. SM performs better than Exp. S. The vertical line at 18 UTC indicates the end of the preforecast period and the beginning of the forecast period during which no current observations are assimilated.

For dewpoint (Fig. 35b), the mesonet data generally either have little effect or improve the initial conditions. The experiment using the mesonet data has lower dewpoint MAE throughout the data-assimilation period, although the magnitude of the improvement widely varies among the case days:  $\approx 0.1$  K for 1 March to  $\approx 2.9$  K for 5 March. After the assimilation ends, the benefit of the mesonet data decreases, such that by 21–22 UTC there is very little benefit from the mesonet data (and perhaps a degradation due to the use of these observations). The case-day mean time series of MAE difference for dewpoint (Fig. 36b) shows improvements due to mesonet data reaching near zero at 21 UTC and shows small degradation, 0.1–0.2 K, for 22–01 UTC.

While mesonet data generally improve wind speed (Fig. 35c) at the initial conditions and throughout the data-assimilation period, for wind direction (Fig. 35d) the results are more mixed, with the initial-condition wind direction at least slightly degraded by the mesonet data for each

case. The domain's mean wind-speed, MAE-difference time series (Fig. 36c) shows improvements throughout the data-assimilation period, with the benefit decreasing to near zero at 23 UTC. For wind direction, the case-day mean indicates a degradation of  $\approx 8^\circ$  in the initial conditions, but by 14 UTC an improvement of  $\approx 3^\circ$  and  $\approx 6^\circ$  improvement at 18 UTC, with the benefit disappearing after 22 UTC. For wind direction at some times for some case days there is a lot of variability from hour to hour in the MAE difference between experiments.

Overall, the mesonet data improve the surface forecasts, with the benefits on average extending to 21 UTC for temperature, 20 UTC for dewpoint, 22 UTC for wind speed and wind direction. For the 0–1,000-m AGL layer, the 19–00 UTC average MAE difference suggests that while the temperature is slightly improved, dewpoint and wind speed are degraded by the use of the mesonet data.

### **6.3 Summary and Conclusions**

WRF-ARW experiments were carried out on 5 case days to investigate the impact of including 3 types of data: TAMDAR, local rawinsonde, and mesonet surface observations. Each of these experiments utilizes the observations both to enhance the initial condition analysis from GFS and to observation nudge the model toward the observations. Observations valid up until 18 UTC are assimilated, with the nudging gradually decreasing to zero by 19 UTC, providing a 6-h preforecast period (12–18 UTC) before the 18-h forecast. To evaluate the value of these observations, we examined how well the model verified against observations for both the surface, the lowest 1,000-m AGL, and the 0–12,000-m AGL layer.

The results reported here do not include tests of statistical significance. Inclusion of such tests could be beneficial in the future.

#### **6.3.1 TAMDAR**

Evaluation of the value of TAMDAR observations focuses on the 0–1,000-m AGL layer because this is the 1,000-m layer with the most TAMDAR observations. Positive impact is most prevalent for temperature, and then for dewpoint, while the impacts on wind are more mixed. The value of using TAMDAR data varies substantially from case day to case day. The 1 March case indicated the most benefit from using TAMDAR data for many measures, and this is the case day used to perform sensitivity experiments to determine the best nudging configuration for TAMDAR observations in Section 5. This raises the issue that the nudging configuration that worked best for 1 March may not be the nudging configuration that is best suited for the other case days. Sensitivity experiments varying the nudging configuration for the other case days would be helpful in determining if this is indeed the case. There are more TAMDAR observations available for assimilation on domain 2 (Fig. 2) for 1 March than some of the other case days, and this may have allowed the TAMDAR to be more effective on 1 March than on some of the other case days.

The relative impacts on the different variables suggest that the wind observations from TAMDAR may be less valuable than the temperature and moisture observations. However, model experiments would be necessary to confirm this, especially because assimilating one variable can impact others. So, for example, it is possible that the assimilation of temperature is degrading model forecasts of wind speed.

Because there were no TAMDAR observations within the 1-km domain during the data-assimilation period, we were unable to evaluate the horizontal radius of influence best used on 1-km domains for above-surface observations. Thus, utilizing a 1-km domain covering an area that includes TAMDAR data would be beneficial toward investigating TAMDAR data assimilation on the 1-km domain.

For application to the battlefield, the ability to prescribe flight paths based on what would most benefit the model forecasts could be very beneficial. During these 5 case days, on the 3-km domain the TAMDAR data are limited to the northwest quadrant of the domain on 3 of the days, and on the other 2 days there were also observations from a flight in the southeastern quadrant (Fig. 3). Presumably, the value of the TAMDAR observations may differ greatly depending on how the TAMDAR observations are distributed horizontally, vertically, and temporally. The potential to apply targeted-observations research to guide aircraft paths with TAMDAR observations on the mesoscale is an intriguing possibility that may have substantial benefits to forecast accuracy.

### **6.3.2 Local Rawinsonde**

The presence of a local rawinsonde on the 1-km domain (at Miramar, CA) in general improves the 1–6-h forecast of temperature and wind in the lowest 1,000 m but degrades the forecast for dewpoint in this layer. For the longer-term forecast in the 0–1,000-m layer (7–18 h), temperature and dewpoint MAEs are generally improved, while wind-speed MAE is slightly degraded and wind direction almost unchanged. A similar comparison was completed using experiments that additionally used TAMDAR data. We also investigated the potential to use TAMDAR data in place of a local rawinsonde and found that, for these cases, TAMDAR is effective at this for temperature and dewpoint forecasts in the short term but not for wind.

Since the local rawinsonde is available at 12 UTC, but the forecast period begins at 18 UTC and the evaluation period covers 19–00 UTC, the evaluation period is 7–12 h after the rawinsonde observation is made. The effect of the local rawinsonde may have been larger if the evaluation period was closer to the valid time of the rawinsonde. Additionally, other observations are being assimilated between 13 and 18 UTC, and the assimilation of these observations may very well be masking the potentially positive influence of the local rawinsonde. The length of the time period over which the rawinsonde was used for data assimilation and the horizontal radius of influence for this observation may not be optimal. Here, we apply the rawinsonde via observation nudging at full strength for a period of 1.5-h centered on the observation time (setting *obs\_twindo*), and then ramp down the influence for 0.75-h before and after a full-strength nudging period. A

longer time period may be appropriate for upper-air observations (e.g., 2 or 3 h at full strength instead of 1.5 h). The horizontal radius of influence for non-surface observations on the 1-km domain is set to 45-km at the surface, increasing as pressure decreases to 90-km at 500 hPa. This value may not be optimal for a 1-km WRF-ARW simulation.

Having more frequent rawinsondes on the finest domain could greatly benefit efforts to evaluate the benefit of a local rawinsonde. The number of available above-surface observations on the 1-km domain is limited and makes it difficult to evaluate the time evolution of the benefits of a local rawinsonde. Therefore, using a 1-km domain over an area completing a field experiment with frequent rawinsondes could be very beneficial.

### **6.3.3 Denser Surface Observations**

The use of additional surface observations for enhancing initial conditions and observations was tested by adding the MADIS mesonet observations to the standard surface and upper-air observations. These observations were filtered using use/reject lists used in a test version of RTMA because there are known siting issues with mesonet observations.

Overall, the mesonet data improve the 1-km domain surface forecasts, with the benefits on average extending to 21 UTC for temperature, 20 UTC for dewpoint, and 22 UTC for wind speed and wind direction. For the 0–1,000-m AGL layer, the 19–00 UTC average-MAE difference suggests that while the temperature is slightly improved, dewpoint and wind speed are degraded by the use of the mesonet data. This suggests that the spreading of the effects of the surface observations may not be optimal. Vertically, the effects of assimilating surface observations is set to be spread throughout the planetary boundary layer during convective conditions and through the lowest 100 m during stable conditions. Reen and Stauffer (2010) demonstrate the benefits of such an approach. However, the influence in the boundary layer may be being spread across too large of an area. The horizontal radius of influence for above-surface observations was tested for 1 March for TAMDAR data on the 3-km, but no experiments were completed examining horizontal radii of influence for surface observations on any of the WRF domains.

It could also be beneficial to examine the potential benefit of standard surface observations versus no surface observations. The experimental design examined the benefit of using no observations versus using standard surface and rawinsonde observations, so no experiment demonstrates the value of surface observations alone. However, surface observations are best assimilated in concert with rawinsondes: Assimilating the rawinsondes helps control the depth of the model's atmospheric boundary layer, which is used to determine the depth through which surface observations are assimilated during convective conditions.



---

## 7. References

---

- Chen F, Dudhia J. 2001. Coupling an advanced land surface-hydrology model with the Penn State-NCAR MM5 modeling system. Part I: model implementation and sensitivity. *Mon Wea Rev.* 129(4):569–585.
- Daniels TS, Murray JJ, Grainger CA, Zhou DK, Avery MA, Cagle MF, Tsoucalas G, Schaffner PR, Neece RT. Validation of tropospheric airborne meteorological data reporting (TAMDAR) temperature, relative humidity, and wind sensors during the 2003 Atlantic THORPEX regional campaign and the Alliance Icing Research Study (AIRS II). Paper presented at: 11<sup>th</sup> AMS Conference on Aviation, Range, and Aerospace; 2004 Oct 4–7; Hyannis (MA).
- Deng A, Stauffer D, Gaudet B, Dudhia J, Bruyere C, Wu W, Vandenberghe F, Lui Y, Bourgeois A. Update on WRF-ARW end-to-end multi-scale FDDA system. Paper presented at: 10th WRF Users' Workshop, NCAR; 2009 Jun 23–26; Boulder (CO).
- De Pondeca MSFV, Manikin GS, Dimego G, Benjamin SG, Parrish DF, Purser RJ, Wu W, Horel JD, Myrick DT, Lin Y, et al. The real-time mesoscale analysis at NOAA's National Centers for Environmental Prediction: current status and development. *Wea Forec.* 2011;26(5):593–612.
- Dudhia J. Numerical study of convection observed during the winter monsoon experiment using a mesoscale two-dimensional model. *J Atmos Sci.* 1989;46(20):3077–3107.
- Gao F, Zhang X, Jacobs NA, Huang X, Zhang X, Childs PP. Estimation of TAMDAR observational error and assimilation experiments. *Wea Forec.* 2012;27(4):856–877.
- Gemmill W, Katz B, Li X. Daily real-time, global sea surface temperature–high-resolution analysis: RTG\_SST\_HR. NOAA/NWS/NCEP/MMAB Office Note 260. 2007 [accessed 2013 Dec 6]. <http://polar.ncep.noaa.gov/mmab/papers/tn260/MMAB260.pdf>.
- Hong S-Y, Dudhia J, Chen S-H. A revised approach to ice microphysical processes for the bulk parameterization of clouds and precipitation. *Mon Wea Rev.* 2004;132(1):103–120.
- Hong S-Y, Lim J-O. The WRF single-moment 6-class microphysics scheme (WSM6). *J Kor Met Soc.* 2006;42(2):129–151.
- Janjić ZI. Nonsingular implementation of the Mellor-Yamada level 2.5 scheme in the NCEP meso model. NCEP Office Note. 2002;437:1–61.

- Jonassen MO, Olafsson H, Agustsson H, Rognvaldsson O, Reuder J. Improving high-resolution numerical weather simulations by assimilating data from an unmanned aerial system. *Mon Wea Rev.* 2012;140(11):3734–3756.
- Kain JS. The Kain-Fritsch convective parameterization: an update. *J Appl Meteor.* 2004;43(1):170–181.
- Lee JA, Kolczynski WC, McCandless TC, Haupt SE. An objective methodology for configuring and down-selecting an NWP ensemble for low-level wind prediction. *Mon Wea Rev.* 2012;140(7):2270–2286.
- Levine SL, Lazarus SM, Splitt ME, Pondeva MSFV. The development and utility of a database of mesonet wind observations for use in the real-time mesoscale analysis (RTMA) system. Paper presented at: 15<sup>th</sup> AMS Symposium on Integrated Observing and Assimilation Systems for Atmosphere, Oceans, and Land Surface (IOAS-AOLS), 2011 Jan 24–27; Austin (TX).
- Levine S, Pondeva M, DiMego G. Improved quality control and metadata usage in the real time mesoscale analysis (RTMA) system. Paper presented at: 46th Annual CMOS Conference/21st AMS Conference on Numerical Weather Prediction/25th Conference on Weather Analysis and Forecasting; 2012 May 29 –Jun 1; Montreal (CA-QC).
- Mlawer EJ, Taubman SJ, Brown PD, Iacono MJ, Clough SA. Radiative transfer for inhomogeneous atmosphere: RRTM, a validated correlated-k model for the long-wave. *J Geophys Res.* 1997;102(D14):16663–16682.
- Moninger WR, Benjamin SG, Jamison BD, Schlatter TW, Smith TL, Szoke EJ. Evaluation of regional aircraft observations using TAMDAR. *Wea Forec.* 2010;25(2):627–645.
- [NOHRSC] National Operational Hydrologic Remote Sensing Center, 2004. Snow Data Assimilation System (SNODAS) data products at NSIDC. Boulder (CO): National Snow and Ice Data Center; [accessed 2013 Dec 6]. <http://dx.doi.org/10.7265/N5TB14TC>.
- Office of the Federal Coordinator for Meteorological Services and Supporting Research (US), 1997: Federal Meteorological Handbook No. 3: Rawinsonde and Pibal Observations. FCM-H3-1997; [accessed 2014 May 14]. <http://www.ofcm.gov/fmh3/fmh3.htm>.
- Passner JE, Kirby S, Jameson, T. Using real-time weather data from an unmanned aircraft system to support the advanced research version of the weather research and forecast model. White Sands Missile Range (NM): Army Research Laboratory (US); April 2012. Report No.: ARL-TR-5950.

- Pondeca MSFV, Manikin G, Zhu Y, Levine S, DiMego G, Purser J, Parrish D, Keyser D, Vavra J. The third upgrade of NOAA's National Centers for Environmental Prediction's Real-Time Mesoscale Analysis. Paper presented at: 46th Annual CMOS Conference/21st AMS Conference on Numerical Weather Prediction/25th Conference on Weather Analysis and Forecasting; 2012 May 29–Jun 1; Montreal (CA-QC).
- Reen BP, Stauffer DR, Davis KJ. Land-surface heterogeneity effects in the planetary boundary layer. *Boundary-Layer Met.* 2014a;150(1):1–31.
- Reen BP, Dumais RE, Passner JE. Mitigating excessive drying from the use of observations in mesoscale modeling. Adelphi (MD): Army Research Laboratory (US); January 2014b. Report No.: ARL-TR-6775.
- Skamarock WC, Klemp JB, Dudhia J, Gill DO, Barker DM, Duda MG, Huang X-Y, Wang W, Powers JG. A description of the advanced research WRF version 3. Boulder (CO): National Center for Atmospheric Sciences (US); June 2008. Report No.: NCAR Tech. Note NCAR/TN-475+STR.
- Szoke EJ, Benjamin S, Collander RS, Jamison BD, Moninger WR, Schlatter TW, Schwartz B, Smith TL. Effect of TAMDAR data on RUC short-term forecasts of aviation-impact fields for ceiling, visibility, reflectivity, and precipitation. Paper presented at: 13<sup>th</sup> AMS Conference on Aviation, Range and Aerospace Meteorology; 2008 Jan 21–24; New Orleans (LA).
- Zhang Y, Liu Y, Childs P, Huffman A, Nipen T. Evaluation of TAMDAR data impact on 4-km CONUS WRF-based RTFDAA simulations and warm-season convection prediction. Paper presented at: 15<sup>th</sup> AMS Symposium on Integrated Observing and Assimilation Systems for Atmosphere, Oceans, and Land Surface (IOAS-AOLS); 2011 Jan 24–27; Austin (TX).

---

## List of Symbols, Abbreviations, and Acronyms

---

3DVAR	three-dimensional variational assimilation
ABL	atmospheric boundary layer
ACARS	Aircraft Communications Addressing and Reporting System
AGL	above ground level
AMDAR	Aircraft Meteorological Data Relay
ASOS	Automated Surface Observing System
AWOS	Automated Weather Observing System
GFS	Global Forecast System
GRIB	Gridded Binary
h	hour
hPa	hectopascal (=1 mb)
KEDW	Edwards Air Force Base, CA, rawinsonde location
km	kilometer
KNKX	Miramar Marine Corps Air Station, San Diego, CA, rawinsonde location
KSNI	San Nicolas Island, CA, rawinsonde location
MADIS	Meteorological Assimilation Data Ingest System
MAE	mean absolute error
MDCRS	Meteorological Data Collection and Reporting System
METAR	Aviation Routine Weather Report
m/s	meter per second
MYJ	Mellor-Yamada-Janjić turbulence parameterization
NCAR	National Center for Atmospheric Research
NCEP-EMC	National Centers for Environmental Prediction – Environmental Modeling Center
PCI	percentage changed improved

RAOB	rawinsonde observation
RRTM	Rapid Radiative Transfer Model
RTMA	Real-Time Mesoscale Analysis
RUC	Rapid Update Cycle
SNODAS	Snow Data Assimilation System
TAMDAR	Tropospheric Airborne Meteorological Data Reporting
TAMDAR-U	Tropospheric Airborne Meteorological Data Reporting - Unmanned Aerial System
TKE	turbulent kinetic energy
UAS	unmanned aerial system
UTC	Coordinated Universal Time
WPS	WRF Preprocessing System
WRF-ARW	Advanced Research version of the Weather Research and Forecasting model

---

## List of Variables

---

$\mu$  = dry hydrostatic pressure

$DIST$  = distance between the observation and the current model point

$e$  = mathematical constant (sometimes known as Napier's constant or Euler's number)

$F_q$  = physical tendency terms of  $q$

$G_q$  = nudging strength for  $q$

$i$  = index to the current observation

$q$  = quantity being nudged

$q_m$  = model value of  $q$

$q_o$  = the observed value of  $q$

$N$  = total number of observations

$obs\_rinxy$  = observation nudging radius of influence setting

$obs\_twindo$  = observation nudging time window setting

$RIN$  = effective radius of influence

$W_q$  = spatiotemporal weighting function

$W_{xy}$  = horizontal weighting function

1 DEFENSE TECH INFO CTR  
(PDF) ATTN DTIC OCA

2 US ARMY RSRCH LABORATORY  
(PDF) ATTN IMAL HRA MAIL & RECORDS MGMT  
ATTN RDRL CIO LL TECHL LIB

2 US ARMY RSRCH LAB  
(PDF) ATTN RDRL CIE M  
B REEN  
R DUMAIS

1 GOVT PRNTG OFC  
(PDF) A MALHOTRA